

AD-A180 318

DTIC FILE COPY

12



PROGRESS REPORT

PREPARATION, CHARACTERIZATION AND PROPERTIES  
OF RAPIDLY SOLIDIFIED ALLOYS

L. Bendersky, D. Shechtman and E. Horowitz

Submitted by: The Johns Hopkins University  
G.W.C. Whiting School of Engineering  
Materials Science and Engineering Department  
Baltimore, Maryland 21218  
Attn: E. Horowitz (301) 338-7916

DARPA Order No. 5527 (5-30-85)

ONR Order No. N00014-85-K-0779

Effective Date: 08-01-85

Expiration Date: 06-30-87

Sponsored by: Defense Advanced Research Project Agency  
(DARPA)  
and The Office of Naval Research (ONR)

DTIC  
ELECTE  
MAY 14 1987  
S A

This document has been approved  
for public release and sale; its  
distribution is unlimited.

October 1986

87 3 12 108

**PROGRESS REPORT**

**PREPARATION, CHARACTERIZATION AND PROPERTIES  
OF RAPIDLY SOLIDIFIED ALLOYS**

**L. Bendersky, D. Shechtman and E. Horowitz**

**Submitted by: The Johns Hopkins University  
G.W.C. Whiting School of Engineering  
Materials Science and Engineering Department  
Baltimore, Maryland 21218  
Attn: E. Horowitz (301) 338-7916**

**DARPA Order No. 5527 (5-30-85)  
ONR Order No. N00014-85-K-0779  
Effective Date: 08-01-85  
Expiration Date: 06-30-87  
Sponsored by: Defense Advanced Research Project Agency  
(DARPA)  
and The Office of Naval Research (ONR)**

**October 1986**

## TABLE OF CONTENTS

### Executive Summary

1. Microstructural Characterization of Rapidly Solidified Nb-Si Alloys  
  
L. Bendersky, F.S. Biancaniello, W.J. Boettinger and J.H. Perepezko  
  
J. Mater. Sci. and Engr. (Submitted)
2. Metallurgy of Phase Relationships of Icosahedral Al-Mn  
  
R.J. Schaefer, L.A. Bendersky, D. Shechtman, W.J. Boettinger and F.S. Biancaniello  
  
Met. Trans. A (Accepted)
3. Microsegregation in Rapidly Solidified Ag-15 wt% Cu Alloys  
  
W.J. Boettinger, L.A. Bendersky, S.R. Coriell, R.J. Schaefer and F.S. Biancaniello  
  
J. of Crystal Growth (Accepted)
4. Crystallization of the Icosahedral Phase in Rapidly Quenched Al-Rich Al-Mn Alloys  
  
A.J. McAllister, L.A. Bendersky, R.J. Schaefer and F.S. Biancaniello  
  
Scripta Met. (Submitted)
5. X-Ray and Electron Metallographic Study of Quasicrystalline Al-Mn-Si Alloys  
  
J.L. Robertson, M.E. Misenheimer, S.C. Moss and L. Bendersky  
  
Acta Met. (Submitted)
6. Stable and Metastable Phase Equilibria in the Al-Mn System  
  
J.L. Murray, A.S. McAllister, R.J. Schaefer, L.A. Bendersky, F. Biancaniello and D.L. Moffat  
  
Met. Trans. A (Accepted)

## Executive Summary

The results obtained on six research projects undertaken within the framework of the DARPA/ONR sponsored research program on rapidly solidified alloys are reported in this progress report. Each of the six topics has been prepared in the form of manuscripts which have been submitted and/or accepted for publication in a scientific journal. The manuscripts deal with microstructure (<sup>NIOBIDIUM / SILICON</sup> ~~Nb-Si~~ alloys), phase relationships of icosahedral alloys (<sup>ALUMINUM / MANGANESE</sup> ~~Al-Mn~~ alloys), microsegregation (<sup>SILVER / COPPER</sup> ~~Ag-Cu~~ alloys), crystallization of the icosahedral phase (<sup>ALUMINUM / MANGANESE</sup> ~~Al-Mn~~ alloys), x-ray and electron studies of quasicrystals (Al-Mn-Si alloys) and phase equilibria studies (Al-Mn alloys). This research has contributed important data and concepts dealing with rapidly solidified alloy systems.



Accession For	
NTIS GRA&I	<input checked="" type="checkbox"/>
DTIC TAB	<input type="checkbox"/>
Unannounced	<input type="checkbox"/>
<i>Added on file</i>	
By	
Distribution/	
Availability Codes	
Dist	Avail and/or Special
<i>A1</i>	

## Microstructural Characterization of Rapidly Solidified Nb-Si Alloys

L. Bendersky\*, F. S. Biancaniello, W. J. Boettinger  
Metallurgy Division  
National Bureau of Standards  
Gaithersburg, MD 20899

and

J. H. Perepezko  
Department of Metallurgical and Mineral Engineering  
University of Wisconsin-Madison  
Madison, WI 53706

### Summary

Rapidly solidified alloys of Nb-Si containing between 12 and 25 at% Si have been examined by analytical electron microscopy to identify the phases present and the solidification path. The phase Nb<sub>3</sub>Si is absent either as the equilibrium tetragonal phase or the A15 phase. Glass formation is observed in high Si alloys but is difficult and observed only near the chill side of melt spun ribbons. The most commonly observed microstructure consists of fine grain mixtures (15-100 nm) of  $\alpha$ -Nb and Nb<sub>5</sub>Si<sub>3</sub>. The observed microstructures are shown to be consistent with the metastable phase diagram and T<sub>0</sub> curves for the Nb-Si system.

### 1. Introduction

Liquid Nb and Nb-based alloys can undercool up to 525 K (0.19 T<sub>M</sub>) prior to nucleation in relatively large samples (0.3 gm) at relatively slow cooling rates [1,2]. This tendency combined with rapid quenching should make Nb alloys an ideal candidate for significant microstructural modification by rapid solidification.

Nb-Si alloys have been of considerable interest because of the possibility of forming the compound Nb<sub>3</sub>Si with the A15 structure with its predicted high

---

\* Also with Center for Materials Research, The Johns Hopkins University, Baltimore, MD 21218.

superconducting transition temperature. Such a phase, would be metastable since equilibrium  $\text{Nb}_3\text{Si}$  has the tetragonal  $\text{Ti}_3\text{P}$ -type structure ( $a = 1.021 \text{ nm}$ ,  $c = 0.519 \text{ nm}$ ;  $P4_2/n$ ) [3]. It is known that the A15 structure can be made by devitrification of amorphous Nb-Si alloys especially when stabilized by high-pressure [4-6]. However, reports of the A15 structure in melt-quenched Nb-Si alloys are subject to some controversy [5,7-9]. Phase identification in this alloy system is complicated by the fact that another equilibrium intermetallic compound in this system,  $\text{Nb}_5\text{Si}_3$ , is also tetragonal with parameters very close to the tetragonal  $\text{Nb}_3\text{Si}$  ( $a = 1.003 \text{ nm}$ ,  $c = 0.507 \text{ nm}$ ,  $I4/mcm$ ) [10]. The purpose of this study is to detail the microstructure of melt-spun ribbons of several Nb-Si alloys by analytical electron microscopy (AEM) characterization with the emphasis on identifying the phases present and understanding the solidification path.

## 2. Experimental

The melt spinning of refractory alloys requires special techniques for alloy melting. One technique [11] uses a non-consumable electrode arc melter with ejection of metal onto the spinning wheel through a small hole in the cold copper hearth by a pressure differential. We have employed a simpler method which uses a standard quartz crucible (shooter) coated with a  $\text{ZrO}_2$  mold wash and an RF levitation coil for specimen heating. With this device small samples are levitated just above the shooter orifice with minimum contact with the quartz. Simultaneous power shut down and helium pressure application ejects a melt stream onto the spinning wheel in the usual manner. An 8.9 cm diameter Cu wheel with a linear velocity of  $\sim 24 \text{ m/s}$  was used to produce ribbons 1-2 mm in width and 20-30  $\mu\text{m}$  in thickness. By this technique, three compositions were melt-spun and investigated: Nb-12.1 at% Si (Nb-4 wt%

Si), Nb-20 at% Si (Nb-7 wt% Si) and Nb-25 at% Si (Nb-9 wt% Si). The eutectic composition between  $\alpha$ -Nb solid solution and Nb<sub>3</sub>Si is 18.7 at% Si [12].

Due to the brittleness of the melt spun material, ion milling was used for TEM specimen preparation. The microstructure of the melt-spun ribbons generally shows inhomogeneity with respect to the distance from the wheel side [13]. Accordingly, two kinds of TEM specimens were prepared: one by milling from both sides of the ribbon and representing the microstructure approximately in the center of the ribbon, and the second by milling from the top side of the ribbon and representing the microstructure near the wheel side of the ribbon. The foils were examined in an analytical electron microscope. In addition to the general observations and the microdiffraction analysis in TEM mode, chemical microanalysis (EDX) in the STEM mode was performed.

### 3. Results

#### 3.1 Microstructure of Nb-25 at% Si alloy (hypereutectic composition)

For this composition, a significant difference in the microstructure has been found between the wheel side and center of the melt-spun ribbons. The wheel side shows an amorphous layer which changes to a fine grain microcrystalline structure with increasing distance from the chill surface. Figure 1 shows a typical micrograph of the structure near a perforation in the TEM foil with selected area diffraction patterns (SADP), positioned under the areas from which they were taken. The sequence of SADP's from the thinnest area (foil edge on the left side of the micrograph) to the thicker areas shows a change from an amorphous diffraction (diffuse rings) to a polycrystalline diffraction. Chemical EDX analysis confirms that the glass has the same composition as the bulk alloy. In a wedge shaped foil microstructural changes normal to the ribbon surface (or to the TEM foil in our case) appear as lateral changes

because the image on the micrograph and diffraction patterns results from the projection of different layers on the imaging plane. The schematic drawing in Figure 1 shows the presumed microstructural variation along the normal to the ribbon surface. The size of the crystalline grains varies from 15 to 100 nm, as a function of distance from the chill surface. Microdiffraction analysis shows that the finest grain region is a mixture of  $\alpha$ -Nb and Nb<sub>5</sub>Si<sub>3</sub> grains. However, it is possible that some of the intermetallic grains are Nb<sub>3</sub>Si (Ti<sub>3</sub>P-type), since microdiffraction under strong dynamical diffraction conditions could show similar patterns for these two tetragonal phases which have almost the same unit cell size. Chemical EDX analysis was impossible for such small grains. For a larger grain size ( $\sim 0.1 \mu\text{m}$ ), the identification was unambiguous.

Figure 2a shows the microstructure observed near the ribbon center (after two-side ion milling). The microstructure consists of fine randomly oriented equiaxed grains (see SADP, Figure 2b). Two types of grains can be recognized: one, with uniform contrast and mostly convex grain boundaries (Type 1), and the other with mottled contrast and some concavity of the grain boundaries (Type 2). The convexity of the Type 1 grains suggests that they solidify before the Type 2 grains. The size of both kinds of grains is of the order of  $0.1 \mu\text{m}$ . Chemical EDX analysis of Type 1 grains using a 10 nm probe produced a spectrum identical to one obtained from a large grain of Nb<sub>5</sub>Si<sub>3</sub> phase produced in a well annealed sample. Analysis of Type 2 grains produced a spectrum containing little Si (Figure 3). Microdiffraction taken from Type 2 grains fits the  $\alpha$ -Nb BCC phase (Figure 4a). Microdiffraction from Type 1 grains fits the Nb<sub>5</sub>Si<sub>3</sub> phase not only by the geometry of the pattern, but also by the spot intensities. For example, Figure 4b shows a pattern, identified

as the  $[1\bar{1}3]$  zone axis of  $\text{Nb}_5\text{Si}_3$ , where the 330 reflection is stronger than 110 and 220, in agreement with the x-ray data from the literature [10]. For  $\text{Nb}_3\text{Si}$  phase the 110 reflection is forbidden, and even under conditions of dynamical diffraction the 220 reflection is expected to be stronger than either the 110 or 330. The mottled contrast of  $\alpha\text{-Nb}$  grains appears to be a result of damage from ion milling [13]. The same contrast was observed in the  $\alpha\text{-Nb}$  phase in ion milled samples which were prepared from cast and annealed alloys. Therefore, we conclude that the microstructure consists of two phases,  $\alpha\text{-Nb}$  and  $\text{Nb}_5\text{Si}_3$ .

Large grains of  $\text{Nb}_5\text{Si}_3$  phase ( $\sim 2 \mu\text{m}$ ) were occasionally found surrounded by a mixture of fine grains. Optical metallography of ribbon cross-sections shows that these grains are of dendritic morphology and mostly occur in the upper part of the ribbons. Dendritic growth of  $\text{Nb}_5\text{Si}_3$  would be expected for this alloy composition under conventional solidification conditions.

### 3.2 Microstructure of Nb-20 at% Si alloy (hypereutectic-close to eutectic composition)

The microstructure on the wheel side of the ribbons for this composition is similar to the Nb-25 at% Si alloy at the same location - amorphous layer followed by microcrystalline mixture of  $\alpha\text{-Nb}$  and  $\text{Nb}_5\text{Si}_3$ . However, the central part of the ribbons exhibits a completely different microstructure. Figure 5a shows the typical microstructure consisting of faulted grains with an embedded second phase. The matrix phase was identified as  $\text{Nb}_5\text{Si}_3$ . (The diffraction pattern in Figure 5b shows the  $[1\bar{1}3]$  zone axis orientation, where the appearance of the strong 330 reflection rules out the possibility of the  $\text{Ti}_3\text{P}$ -type phase.) The matrix is divided into slightly misoriented subgrains, elongated normal to the fault planes, and the misorientation can be clearly seen from the inclination of faults and from SADP's. The second phase was found to be  $\alpha\text{-Nb}$ .

(Figure 5c shows a microdiffraction pattern of the  $[012]_{\alpha\text{-Nb}}$  zone axis orientation.) Observations at different orientations indicate that the  $\alpha\text{-Nb}$  particles have a rod-like morphology with an interrod spacing of  $\sim 40\text{-}50\text{ nm}$ . Hence, we conclude that the microstructure is a rod eutectic of  $\text{Nb}_5\text{Si}_3$  and  $\alpha\text{-Nb}$ .

### 3.3 Microstructure of Nb-12 at% Si (hypoeutectic composition)

At this composition, no difference in microstructure was observed between the wheel side and the center of the ribbons. The microstructure shows a transverse section of dendrites of  $\alpha\text{-Nb}$  phase with an interdendritic second phase of  $\text{Nb}_5\text{Si}_3$  (see Figure 6). Usually the  $\text{Nb}_5\text{Si}_3$  phase appears to be continuous, separating the  $\alpha\text{-Nb}$  dendrites. But in some regions an interlocking structure of the two phases was observed between the dendrites.

## 4. Discussion

Three features of the microstructure of the Nb-Si alloys merit discussion: the absence of the equilibrium tetragonal  $\text{Nb}_3\text{Si}$  phase, the extremely fine grain structures of  $\alpha\text{-Nb}$  and  $\text{Nb}_5\text{Si}_3$ , and metallic glass formation near the wheel side. The  $\text{Al}_5\text{Nb}_3\text{Si}$  phase was not observed in the present study.

Absence of tetragonal  $\text{Nb}_3\text{Si}$  phase - A common occurrence in RSP is the absence of a phase which according to the equilibrium diagram should be present. When a phase has difficulties in nucleation and/or growth, the phase selection is governed by a metastable phase diagram [14]. Such a diagram is constructed from the equilibrium diagram [12] in Figure 7 where the  $\text{Nb}_5\text{Si}_3$  (designated  $\gamma$ ) liquidus extends below the  $L + \text{Nb}_5\text{Si}_3 + \text{Nb}_3\text{Si}$  peritectic isotherm and intersects the  $\alpha\text{-Nb}$  liquidus to form a metastable eutectic  $L + \alpha\text{-Nb} + \text{Nb}_5\text{Si}_3$ . For alloys near a peritectic reaction, solidification of the high temperature phase, in this case  $\text{Nb}_5\text{Si}_3$ , can continue below the peritectic temperature while the remaining liquid develops only slight undercooling

with respect to the low temperature phase, in this case  $\text{Nb}_3\text{Si}$ . This is especially true when the two liquidus curves are nearly parallel. Hence phases ordinarily formed by peritectic reactions may often be absent in RSP microstructures.

Further rational for the absence of the tetragonal  $\text{Nb}_3\text{Si}$  phase is obtained by examining the shapes of crystals grown under slow cooling conditions. The  $\text{Nb}_3\text{Si}$  phase grows as strongly faceted idiomorphs, while the  $\text{Nb}_5\text{Si}_3$  phase grows as smoothly curved dendrites with only occasional facets [3]. Facetting usually indicates difficult atomic attachment kinetics at the liquid-solid interface. Under rapid quenching conditions, growth competition between  $\text{Nb}_3\text{Si}$  and  $\text{Nb}_5\text{Si}_3$  will be won by  $\text{Nb}_5\text{Si}_3$ . This phase is seen to dominate in the observed microstructures.

The observation of a rod eutectic structure of  $\alpha\text{-Nb}$  and  $\text{Nb}_5\text{Si}_2$  in the center of Nb-20 at% Si ribbons is also consistent with the absence of the tetragonal  $\text{Nb}_3\text{Si}$  phase. Figure 7 indicates a metastable eutectic for these phases at about 20 at% Si. In many alloys eutectic microstructures are observed at off-eutectic compositions at moderate growth rates due to a shift in the coupled zone [15] toward the phase of the eutectic which shows a more pronounced tendency for facetting. In the present case  $\text{Nb}_5\text{Si}_3$ , although less faceted than  $\text{Nb}_3\text{Si}$ , is more faceted than  $\alpha\text{-Nb}$ . Hence the eutectic structure is observed on the Si-rich side of the eutectic composition. The eutectic spacing of 30 nm is extremely fine and approaches the minimum spacing observed in other eutectic microstructures [16,17]. This minimum corresponds to a growth rate maximum for eutectic microstructures in the range of 1-10 cm/s [18]. Closer to the wheel surface the imposed solidification velocity apparently exceeds this maximum and the eutectic structure is not observed.

Fine grain structure of  $\alpha$ -Nb and  $\text{Nb}_5\text{Si}_3$  - A useful method for examining the thermodynamic options available to an alloy undergoing rapid solidification is to examine the  $T_0$  curves for the various liquid to crystal transformations in a system. Schematic  $T_0$  curves are included for the  $\alpha$ -Nb and  $\text{Nb}_5\text{Si}_3$  ( $\gamma$ ) phases in Figure 7. A  $T_0$  curve places a bound on temperatures and compositions where partitionless solidification is possible. Regardless of how rapidly an alloy is quenched, a range of compositions may exist between adjacent  $T_0$  curves where partitionless solidification is impossible and crystal growth must involve the more difficult process of diffusional solute redistribution into a mixture of solid phases [19]. Because of this difficulty, glass formation is most likely in this range. Due to the limited equilibrium range of composition of  $\text{Nb}_5\text{Si}_3$  compared to  $\alpha$ -Nb, the range of compositions is likely centered at hypereutectic compositions as indicated. The two phase mixture of fine equiaxed grains of  $\alpha$ -Nb and  $\text{Nb}_5\text{Si}_3$ , as well as the region of glass formation, observed for the 20 and 25 at% Si alloys are consistent with this range of compositions. In this range the structures are two options which thermodynamics permits. Partitionless solidification of Nb-12 at% Si alloy may or may not be possible depending on the precise  $T_0$  location. It was not observed however in the present experiments.

The fine two phase grain structure clearly involves copious nucleation. Although a detailed understanding of this process is not yet possible, one factor which can increase the opportunity for high nucleation rates is found in the relatively slow growth rates for crystals which require solute redistribution. Simple estimates for grain size produced during isothermal transformations involve a ratio of nucleation rate to growth rate. For a fixed nucleation rate, slow growth rates decrease grain size. Alternately, during continuous

cooling the rate of recalescence after the initial nucleation event depends on the crystal growth rate. If it is slow, the melt may be undercooled further permitting a rapid rise in the nucleation rate [20].

A good portion of the interest in RSP has been focused on the novel microstructures associated with the solidification of non-equilibrium phase structures. There have been numerous reports on the formation of supersaturated solid solutions, metastable intermediate crystalline phases and metallic glass. Indeed, most of the previous work dealing with rapid liquid quenching of Nb-Si alloys has involved efforts to synthesize the metastable Nb<sub>3</sub>Si (A15) phase either during solidification directly or indirectly by devitrification of an amorphous product. However, the fine two phase grain structures developed during the melt spinning of Nb-Si alloys indicate that another pattern of a metastable microstructure is accessible in the form of very high grain densities of the equilibrium phases which were observed to vary from  $10^{18} \text{ m}^{-3}$  to  $10^{21} \text{ m}^{-3}$ . A high density of grains for a two phase mixture is metastable due to a high incoherent interphase boundary area. For example, with a grain size of  $0.12 \text{ } \mu\text{m}$  and an interphase boundary energy in the range of  $500\text{-}1000 \text{ mJ/m}^2$  that is typical for incoherent interfaces, the excess free energy due to the polycrystalline grain structure is in the range of about  $120\text{-}250 \text{ J/mole}$ . However, for the ultrafine grains with size of  $0.015 \text{ } \mu\text{m}$  the free energy increment increases to the range of about  $800\text{-}1600 \text{ J/mole}$ . Thus, with ultrafine grains the level of metastability is comparable to that associated with non-equilibrium crystal structures.

The devitrification of an amorphous phase is a fairly well-recognized approach to the production of very fine grain sizes. During such treatments it appears that either the growth of "quenched in" nuclei or the volume

nucleation of crystals during heating can yield grain sizes of the order of 0.01-0.1  $\mu\text{m}$ . Often, it has been observed that the crystallization steps associated with the devitrification process can also involve one or more metastable phase products. With each stage the product phase grain size can increase so that the initial fine sizes are not retained as the reaction reaches the equilibrium phase products. In addition, the attainment of an equiaxed grain structure resulting from an isotropic growth is restricted to a polymorphic type of crystallization reaction. In this sense, the equiaxed two phase ultrafine grain structure that is established during melt spinning in Nb-Si alloys represents a distinct microstructural pattern of non-cooperative growth that is not readily achieved by a devitrification treatment. However, due to the gradient in solidification conditions through the ribbon cross section during melt spinning, the ultra fine duplex phase region is restricted in extent. Other processing methods, such as rapid solidification of powders which can provide a more uniformly undercooled sample, may allow for the production of a more extensive ultra fine two phase structure region.

Metallic glass formation - In the Nb-Si system the conditions for amorphous phase formation during melt spinning are marginal. Based upon the reported temperatures [4,5,8,9] of about 600°C for devitrification of Nb-Si glasses in the range of 18-25 at/o Si,  $T_g/T_L < 0.31$  while good glass forming alloys typically exhibit  $T_g/T_L$  values of 0.5-0.6. Only in a restricted region within about 0.5  $\mu\text{m}$  of the wheel was any amorphous zone observed. Even in this zone the amorphous phase contained extremely fine crystallites. Glass formation at the very high undercooling in the presence of the prolific nucleation suggests that kinetic difficulties in maintaining a high rate of diffusion controlled growth can be important in glass formation.

The observation of ultra fine grains adjacent to the glassy layer in Nb-9wt% Si indicates that transient nucleation effects play an important role in vitrification. As noted, the diffusional growth limitations that restrict the solidification rate for eutectic products will also yield ultra fine grain duplex structures. Further, the steep grain size transition from 0.01  $\mu\text{m}$  to 0.1  $\mu\text{m}$  across the ribbon also suggests that the finest grains are forming under relatively sluggish diffusional kinetics. The same diffusional growth difficulties will also inhibit the full development of the steady state cluster size distribution that controls the evolution of crystal nuclei. When non-steady state cluster formation is included into the calculation of the cooling conditions to bypass crystallization, Kelton and Greer [21] have shown that the critical cooling rate for glass formation can be reduced by an order of magnitude or more. For a marginal glass forming alloy system such as Nb-Si these considerations are important in understanding glass formation and also the development of an ultrafine duplex grain structure, but an assessment of the magnitude of the non-steady state effects requires quantitative kinetic measurements which are not available at this time.

## References

1. L. L. Lacy, M. B. Robinson, and T. J. Rathy, J. Cryst. Growth 51, 47 (1981).
2. L. L. Lacy, T. J. Rathy, and M. B. Robinson, J. Appl. Phys. 53, 682 (1982).
3. D. K. Deardorft, R. E. Siemens, P. A. Romans, and R. A. McCune, J. Less-Common Metals 18, 11 (1969).
4. W. K. Wang, H. Iwasaki, C. Suryanarayana, T. Masumoto, N. Toyota, T. Kukase, and F. Kagiku, J. Mat. Sci. 17, 1523 (1982).
5. K. Togano, H. Kumakura, and K. Tachikawa, Phys. Lett. 76A, 83 (1980).
6. R. M. Waterstrat, F. Haenssler, J. Muller, S. D. Dahlgren, and J. O. Willis, J. Appl. Phys. 49(3), 1143 (1978).
7. R. M. Waterstrat, F. Maenssler, and J. Muller, J. Appl. Phys. 50(7), 4763 (1979).
8. T. Masumoto, A. Inoue, S. Sakai, H. Kumura, and A. Hoshi, Trans. JIM 21, 115 (1980).
9. L. R. Gresock and M. T. Clapp, Materials Letters 2(6A&B), 492 (1984).
10. Nat. Bur. Stand. (U.S.) Monogr. 25, Sec. 15, 44 (1978).
11. S. H. Whang and B. C. Giessen, in Rapid Solidification Processing: Principles and Technologies III; ed. by R. Mehrabian, NBS, 1983, 439.
12. Metals Handbook, Vol. 8, ASM, Metals Park, OH (1973), 383.
13. L. Bendersky and W. J. Boettinger, Proceedings of 43rd Annual Meeting of EMSA, G. W. Bailey, ed., San Francisco Press, San Francisco, CA (1985), 54.
14. J. H. Perepezko and W. J. Boettinger, Mats. Res. Soc. Symp. Proc. 19, 223 (1983).
15. W. Kurz and D. J. Fisher, Int. Met. Rev. 5 & 6, 177 (1979).
16. W. J. Boettinger, D. Shechtman, R. J. Schaefer, and F. S. Biancantiello, Met. Trans 15A, 55 (1984).
17. W. J. Boettinger, D. Shechtman, T. Z. Kattamis, and R. J. Schaefer, in "Rapidly Quenched Metals," S. Steeb and H. Warlimont, eds., North Holland, Amsterdam, 871 (1985).
18. W. J. Boettinger, in "Rapidly Solidified Crystalline and Amorphous Alloys," B. Kear and B. Giessen, eds., North Holland, NY, 15 (1982).

19. W. J. Boettinger, F. S. Biancaniello, G. M. Kalonji, and J. W. Cahn, in Rapid Solidification Processing: Principles and Technology II, R. Mehrabian, B. H. Kear, and M. Cohen, eds., Claitors, Baton Rouge, 50 (1980).
20. W. J. Boettinger and J. H. Perepezko, in "Rapidly Solidified Crystalline Alloys," S. Das, ed., TMS-AIME (1986) in press.
21. K. F. Keton and A. L. Greer, in "Rapidly Quenched Metals," S. Steeb and H. Warlimont, eds., North Holland, Amsterdam, 223 (1985).

## Figure Captions

- Figure 1. Microstructure of Nb-25 at % Si near TEM foil edge (left side of the micrograph) for specimen polished from one side. Selected area diffraction patterns (SADP's) are positioned under the areas from which they were taken. On the bottom a schematic drawing shows the presumed microstructure across the ribbon.
- Figure 2. Microstructure of Nb-25 at % Si for specimen polished from both sides SADP (b) shows random orientation of equiaxed grains of two phases (type 1 and 2, marked on the micrograph (a)).
- Figure 3. EDS X-ray spectrum from type 1(a) and type 2(b) grains of Nb-25 at % Si alloy.
- Figure 4. Microdiffractions taken from (a) type 2 grain ( $B = [111]$  of  $\alpha$ -Nb); (b) type 1 grain ( $B = [\bar{1}\bar{1}3]$  of  $Nb_5Si_3$  phase). Note the strong 330 reflection in (b).
- Figure 5. Microstructure of Nb-20 at % Si for specimen polished from both sides. The faulted matrix is  $Nb_5Si_3$  phase as shown by the SADP (b) at the zone axis orientation  $B = [\bar{1}\bar{1}3]$ . The second phase is  $\alpha$ -Nb as shown by microdiffraction (c) of the  $[012]$  zone axis orientation.
- Figure 6. Microstructure of Nb-12 at % Si showing transverse section of  $\alpha$ -Nb dendrites with an interdendrite second phase of  $Nb_5Si_3$ . Right side of the micrograph shows an interlocking structure of the two phases.
- Figure 7. Phase diagram for Nb-Si showing metastable extension of  $Nb_5Si_3$  (i.e.,  $\gamma$ ) liquidus to form a metastable eutectic  $L \rightarrow \alpha$ -Nb +  $Nb_5Si_3$ . This extension is relevant when the  $Nb_3Si$  phase is absent. Also shown are approximate  $T_0$  curves for the transformation of liquid to  $\alpha$ -Nb and to  $\gamma$ .

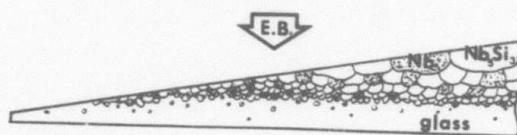
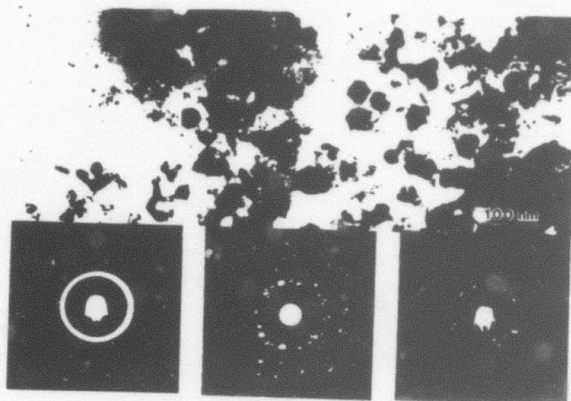


Fig 1

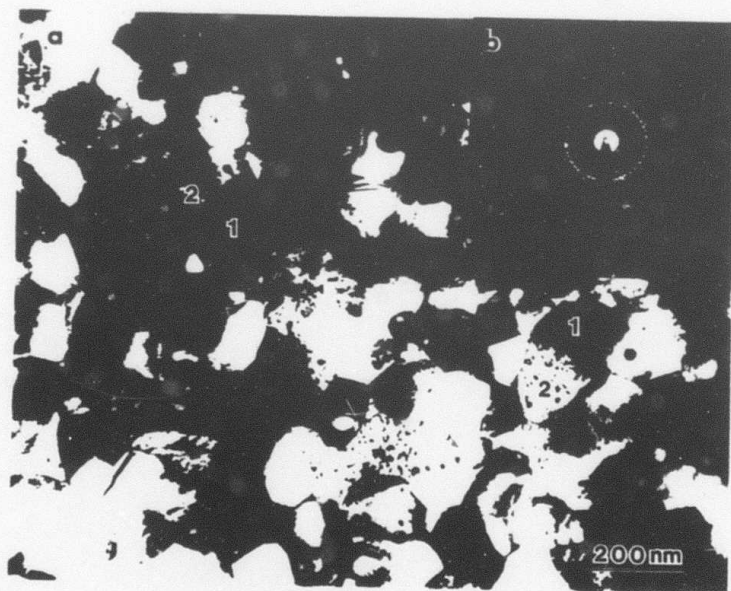


Fig 2

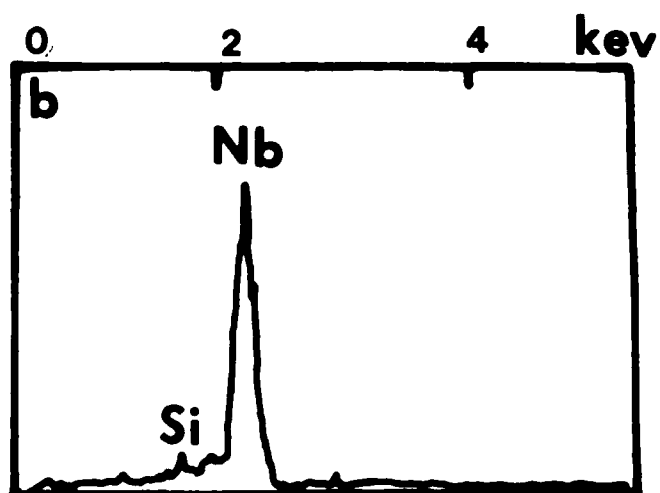
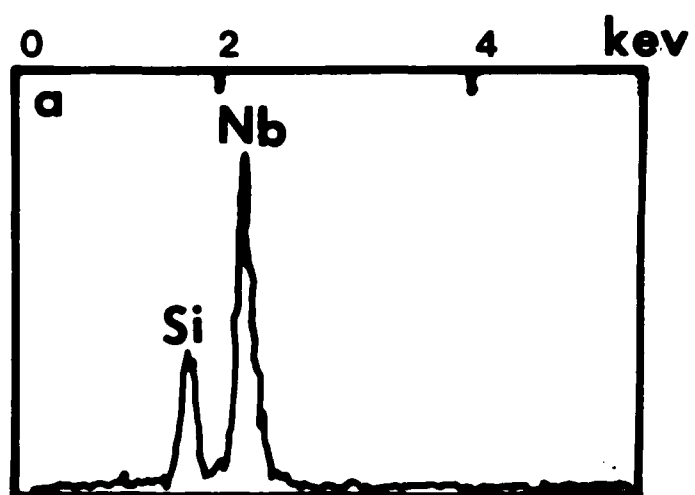


Fig 3

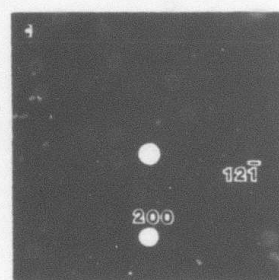
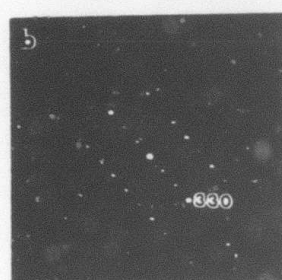
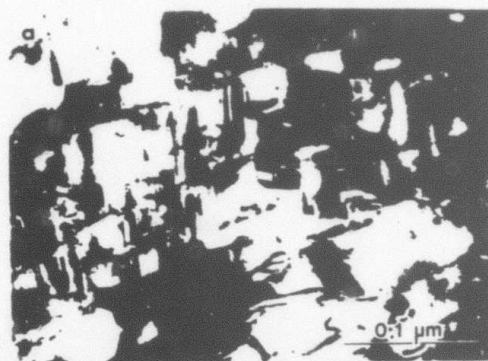


Fig 5

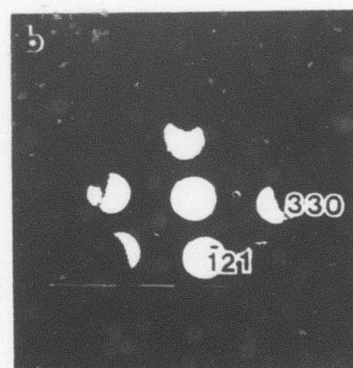
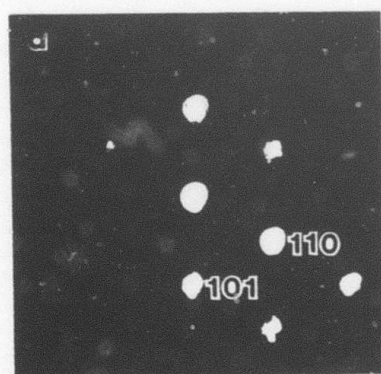


Fig 4

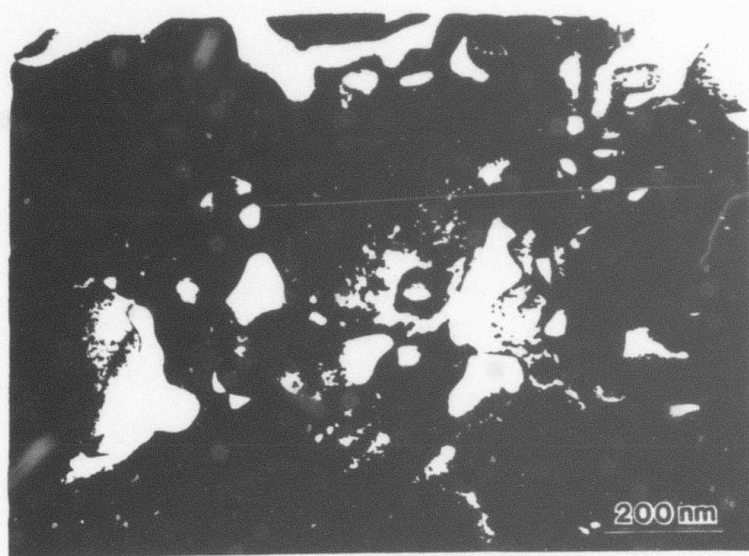


Fig 6

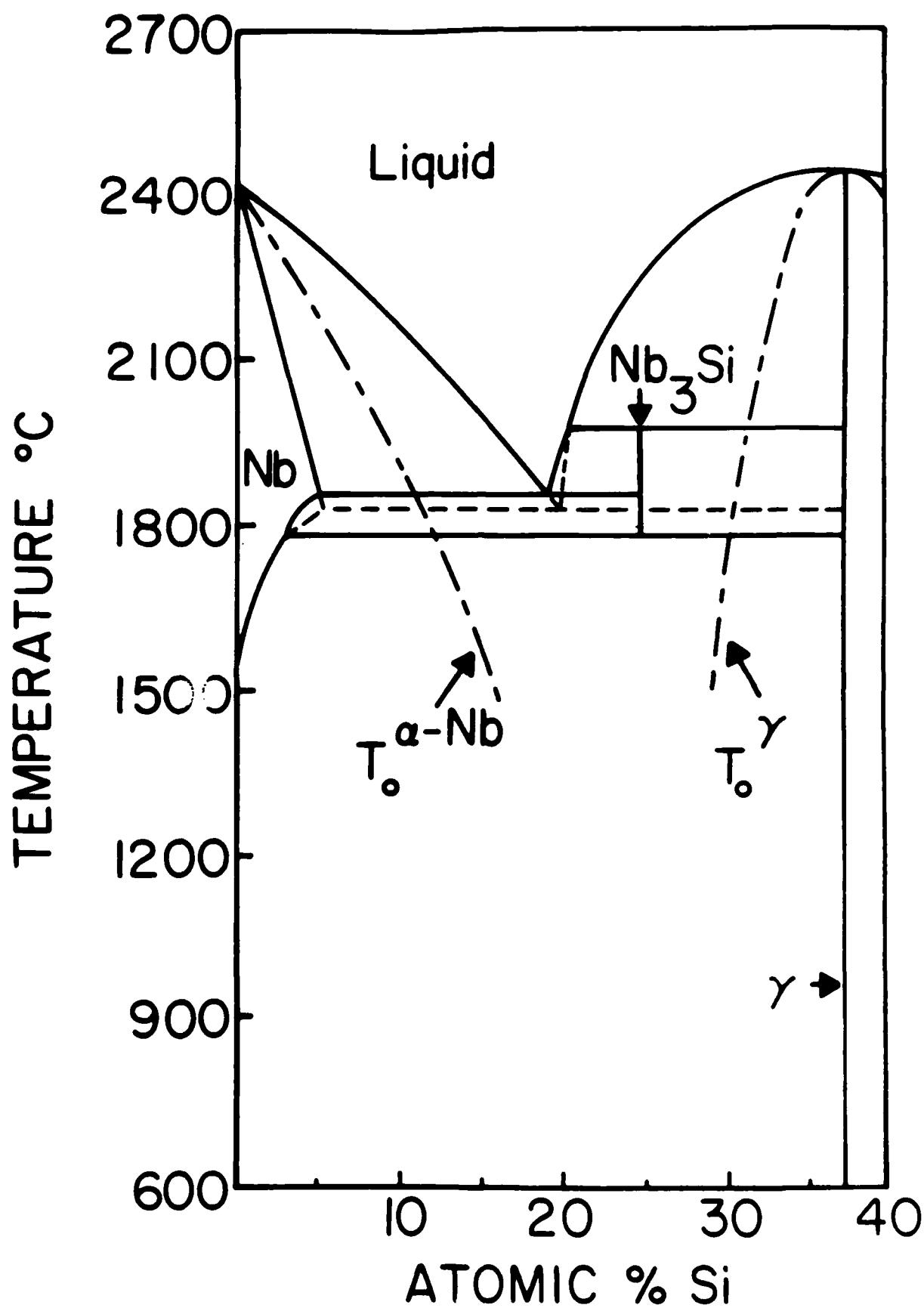


Fig. 7

## Metallurgy of Phase Relationships of Icosahedral Al-Mn

R. J. Schaefer, L. A. Bendersky, D. Shechtman, W. J. Boettinger and  
F. S. Biancaniello

### ABSTRACT

The solidification conditions leading to the formation of the icosahedral phase in Al-Mn alloys have been investigated, using samples prepared by melt spinning and electron beam surface melting. It is found that the icosahedral phase can grow with a range of compositions, but that it grows in competition with another metastable phase which is decagonal. Both of these phases can displace the equilibrium intermetallic phases by nucleating ahead of them in the melt when the solidification velocity is greater than a few centimeters per second. The relative abundance of the icosahedral and decagonal phases varies with composition and solidification rate. Icosahedral crystals in electron beam melt trails are often about 25  $\mu\text{m}$  in diameter, and they grow dendritically along a preferred crystallographic direction.

---

R. J. Schaefer, W. J. Boettinger and F. S. Biancaniello are in the Metallurgy Division, Institute for Materials Science and Engineering, National Bureau of Standards, Gaithersburg, MD 20899.

L. A. Bendersky is in the Center for Materials Research, The Johns Hopkins University, Baltimore, MD 21218, and is a guest worker at NBS.

D. Shechtman is in the Department of Materials Engineering, Technion, Haifa, Israel, and is a guest worker at NBS.

## Metallurgy of Phase Relationships of Icosahedral Al-Mn

R. J. Schaefer, L. A. Bendersky, D. Shechtman, W. J. Boettinger,  
F. S. Biancaniello

### I. Introduction

The icosahedral phase (1) which has been reported in aluminum-manganese alloys is readily formed by rapid solidification. This phase exhibits an electron diffraction pattern which has sharp spots, but it has a five-fold symmetry which is not consistent with crystal lattice translations. During rapid solidification, the icosahedral phase grows dendritically and competes with several other stable and metastable phases for dominance in the microstructure. The material thus produced is typically compositionally segregated and even multiphase. Hence, it is generally not adequate for bulk property measurements of the icosahedral phase. Because the icosahedral phase in the Al-Mn system is metastable, it is not possible to obtain single phase specimens by long anneals at an appropriate temperature and composition. In this paper we report the microstructure and growth behavior of the icosahedral and associated phases as a function of alloy composition and solidification conditions.

Many different intermetallic compounds have been reported in Al-rich Al-Mn alloys (2,3,4) and some compounds previously considered to be stable have subsequently been reported to be metastable (5). It is clear that the attainment of equilibrium is extremely sluggish and that the primary solidification phase expected on the basis of the phase diagram may be easily replaced by another of the equilibrium phases or by a metastable phase (6). All phase diagram authors agree, however, that in the Al-Mn system a series of intermetallic compounds forms by peritectic reactions. Figure 1 represents a

orientation textures which were believed to be present for the  $\alpha$ -Al but not for the other phases. Nonetheless, the trends with composition as shown in Figure 1 could be clearly distinguished. At Mn concentrations of 30 wt% or more it was found that the very fine flakes had a phase distribution which differed from that of the normal ribbon segments, and it is assumed that the former solidified more rapidly. The phases referred to in the figure are described in more detail below.

#### 1. Aluminum ( $\alpha$ )

The equilibrium limit of solid solubility of Mn in Al is approximately 1.6 wt% but this solid solubility can be greatly extended by rapid solidification (9). We previously reported observations of the microstructure of melt-spun ribbons containing up to 15 wt% Mn in solid solution (10). At higher Mn contents, the icosahedral phase appears but  $\alpha$ -Al is still found to be present. At 25 wt% Mn, which is close to the stoichiometric composition for  $Al_6Mn$ ,  $\alpha$ -Al is still strongly present in the x-ray diffraction patterns but in TEM pictures much of it is hidden between the arms of the icosahedral dendrites.  $\alpha$ -Al is still detected by x-ray diffraction in a ribbon containing 30 wt% Mn but it is not seen in a ribbon with 33.7 wt% Mn.

The manganese content of the  $\alpha$ -Al present in melt-spun samples can be deduced from lattice parameter measurements. Figure 3 shows the measured d spacing of the (111) plane of Al in ribbons of different compositions. The values shown in this figure have been calibrated by the use of Si powder mixed with the sample. For ribbons containing up to 18 wt% Mn, the d spacing decreases steadily with composition, as is well established for this supersaturated solid solution. In ribbons of higher composition, where the icosahedral phase is present, the d spacing of the Al (111) planes rises back to a

value indicative of a manganese content of less than 4 wt%. Thus in these samples the icosahedral phase must be growing with a manganese content greater than the average composition of the alloy, leaving the intercrystalline liquid depleted in manganese.

The 15 and 18 wt% Mn ribbons both show Al (111) peaks which are split, indicating two different concentrations of solid solution, together with weak diffraction peaks from the icosahedral phase. These ribbons appear to contain some regions which are supersaturated solid solution and other regions which contain icosahedral phase plus manganese-depleted aluminum. These different regions reflect the point-to-point variations of solidification conditions within the ribbons, which become evident only when these conditions are near the limit for one of the modes of solidification.

## 2. Icosahedral Phase

The icosahedral phase is present in some regions of ribbons with as little as 15 wt% Mn and it increases in abundance as the Mn content increases. In the very thinnest flakes, the icosahedral phase reaches its maximum abundance at 33.7 wt% Mn, where it is accompanied by a small amount of the decagonal phase (described below) but no detectable Al. At still higher Mn concentrations the decagonal phase rapidly gains in abundance. In thicker ribbons the icosahedral phase is replaced by decagonal phase at lower Mn content, and none is seen at compositions above 33 wt% Mn (see Figure 1).

The d spacing of the most strongly reflecting planes of the icosahedral phase also changes as the composition of the bulk alloy changes, as is shown in Figure 4. This shift indicates that the icosahedral phase itself can exist over a range of compositions, but the actual composition of the icosahedral material in each alloy is not known.

The microstructure of the icosahedral phase has been described in detail elsewhere (11). Figure 4 shows a typical icosahedral crystallite, which is easily recognized by its mottled appearance and coral-like branches with little evidence of preferred crystallographic growth directions. The crystallites have grown radially outward from independent nucleation sites with little if any tendency toward a columnar directional growth due to temperature gradients. A somewhat different dendrite morphology is observed in electron beam melted alloys of lower composition, as will be described below.

### 3. $\text{Al}_6\text{Mn}$

This well-characterized equilibrium phase (12), with a stoichiometric composition of 25.3 wt% Mn and an orthorhombic structure, is seen in melt-spun ribbons only if they were unusually thick as a result of abnormal processing conditions such as a low wheel speed. In these cases it totally displaced the icosahedral and decagonal phases: no ribbons were seen in which  $\text{Al}_6\text{Mn}$  occurred together with the metastable phases, so the transition from orthorhombic to quasicrystal apparently occurs within a narrow range of processing parameters.

$\text{Al}_6\text{Mn}$  forms a eutectic with  $\alpha\text{-Al}$ , which on the phase diagram lies at 1.8 wt% Mn and  $658^\circ\text{C}$ , only  $2^\circ\text{C}$  below the melting point of pure Al. It has been shown (13) that with increasing growth velocities, coupled eutectic growth occurs at higher manganese concentrations, but the range of composition and growth rate conditions under which coupled growth occurs appears to be very narrow, because eutectic microstructures were not observed in the present experiments.

### 4. $\text{Al}_4\text{Mn}$

The  $\text{Al}_4\text{Mn}$  phase has been reported to be hexagonal with a large unit cell

( $c = 12.4 \text{ \AA}$ ,  $a = 28.4 \text{ \AA}$ ), but no further details of its structure are available. Conflicting opinions on its range of stability have been reported (3,5). This phase was not seen in melt-spun ribbons except after high-temperature equilibration anneals. A ribbon containing 30 wt% Mn was mostly  $\text{Al}_4\text{Mn}$  after a 24 hour anneal at  $675^\circ\text{C}$ : this sample formed the basis for the diffraction pattern shown in Figure 2.

#### 4. Decagonal Phase

An additional metastable phase appears in melt-spun ribbons containing 30 or more wt% Mn. This phase is highly faulted, has a complex electron diffraction pattern, and is apparently identical to a phase previously (10) detected in annealed Al-5 wt% Mn ribbons and designated "T" phase. In melt-spun material containing 30 or more wt% Mn the decagonal phase is especially prominent in thicker ribbons, which probably solidified more slowly than thinner ones of the same composition. The thicker ribbons of 35 and 37 wt% Mn alloys were single-phase decagonal.

The decagonal phase is recognizable by its highly faulted structure as well as its blocky form (Figure 5). Its close crystallographic relationship to the icosahedral phase, as revealed by electron diffraction and high-resolution microscopy, has recently been described (14,15): it has been shown to be a quasicrystalline phase with a 10-fold symmetry axis and a one-dimensional translational periodicity along this axis. In several specimens it was found that the decagonal phase had grown epitaxially on the icosahedral phase.

#### B. Electron Beam Surface Melts

Figure 6 summarizes the primary phase found in the various electron beam melt scans at different velocities and alloy compositions.

### 1. Intermetallic Region

At higher manganese contents and low scan velocities, the melt scans solidify by primary growth of large intermetallic plates or needles. In optical micrographs these frequently seem to have a coating of a second intermetallic phase, in a microstructure characteristic of peritectic alloys. Figure 7 shows an example of such a microstructure in an Al-25 wt% Mn alloy scanned at 0.25 cm/s. At slightly higher scan velocities ( $> 2.5$  cm/sec) the primary crystals often form bundles of platelets with progressively finer scale as the velocity increases (Figure 8). These platelets also seem to have a coating of a second intermetallic phase, but TEM analysis of several of them revealed both the platelets and the coating to be  $Al_6Mn$ . Although the intermetallics can sometimes be recognized by morphological features, most of them have not been positively identified in the optical micrographs and they are labelled merely as intermetallics in Figure 6.

### 2. Aluminum Region

At relatively low Mn concentrations and high scan velocities, cellular primary Al, highly supersaturated in Mn, is formed. Figure 9 compares electron beam melts of an Al-14 wt% Mn alloy at scan rates of 1, 2.5 and 5 cm/s, showing the change with increasing scan rate from a dense array of  $Al_6Mn$  dendrites to scattered  $Al_6Mn$  dendrites to (unresolved) cellular aluminum.

### 3. Icosahedral Phase

The icosahedral phase dominated the melt zone of electron beam scans at 200 cm/sec, for alloys containing 22 or more wt% Mn. It most frequently had the form of equiaxed crystals, indicating that just as in the melt spun ribbons it formed from separate nucleation centers and then grew radially outward. Compared to the icosahedral grains in the melt-spun ribbons, those in the

electron beam scans were larger (often over 10  $\mu\text{m}$  in diameter) and had more well-defined dendritic growth directions.

In the electron beam surface melts on the alloy containing 18 wt% Mn, the icosahedral grains were often far enough apart to grow without interference from their neighbors, with the result that their external form clearly shows their unusual icosahedral symmetry. The grains are randomly oriented in the melt trails, so that in a given plane of polish many will be found in which the five-fold symmetry is conspicuous (Figure 10). In grains with such orientation, however, dendrite arms are not seen as continuous rods but as broken rows of particles. Continuous dendrite arms are seen when the plane of polish lies perpendicular to a two-fold symmetry axis and passes through the point at which growth originated (Figure 11). In this case the angles between the dendrites can be compared to a stereographic projection of the icosahedral system with the conclusion that they grow from the central nucleus along the three-fold symmetry axes (the  $(10\ 10\ 10)$  directions (16)), forming sheets of dendrite arms in the planes containing adjacent three-fold axes. On this basis, a model was constructed showing the overall structure of the crystallites (Figure 12). All of the crystals seen in the melt trails of Al-18 wt% Mn, such as in Figure 10, can be understood as different cross sections of this model. TEM examination of these crystals does not indicate any faceting (Figure 13) but in some cases it reveals them to be encrusted with an overgrowth of the T phase.

#### 4. Decagonal Phase

In the alloys containing 22 and 25 wt% Mn, the decagonal phase dominated the melt zone at scan velocities of 10 cm/s. Although the decagonal phase crystals often appeared to be randomly dispersed, careful inspection frequently

showed them to be parts of rather large dendritic systems. At velocities between 10 and 200 cm/s, there was a steady change in the proportions of icosahedral and decagonal phase, as measured by x-ray diffraction (Figure 6) and confirmed by TEM. In the 18 wt% Mn alloy, by contrast, the icosahedral phase persisted to velocities as slow as 2.5 cm/s.

#### V. Discussion

From the analysis of the melt-spun ribbons, we can draw some conclusions about the form of the metastable equilibrium between the icosahedral phase and the melt. Figure 14 shows the hypothetical position of the solidus and liquidus curves for the icosahedral phase. The presence of aluminum, depleted in manganese, in samples containing 30 wt% Mn or less indicates that any metastable congruent melting composition of the icosahedral phase must occur at  $> 30$  wt% Mn.

The substantial change of lattice parameter of the icosahedral phase with overall alloy composition indicates that the icosahedral phase is not a stoichiometric compound and that it must exist over a significant range of compositions. Therefore, the usual microsegregation processes which occur during solidification would lead to the presence of a range of compositions within any given sample. Hence it is not possible to interpret x-ray line width measurements solely in terms of orientational correlation distances. In addition, if we assume local equilibrium at the interface between the liquid and the growing icosahedral crystal, then the low manganese content of the aluminum which forms between the icosahedral phase grains shows that the liquidus curve of the icosahedral phase extends to compositions as low as only a few percent Mn at the temperature where the Al solidifies. Because of the very low slopes of both the liquidus and solidus curves for the Al phase,

the solidification temperature of the Al in this case probably lies only a few degrees below the freezing point of pure Al.

The results described here provide little information on the metastable liquidus temperature of the icosahedral phase. We can, however, make an estimate of the temperature at which the icosahedral crystals nucleated in the Al-18 wt% Mn alloy. The 2.5 cm/sec electron beam melt trail of this alloy contains dendrites of  $Al_6Mn$  which grow up from the substrate, but near the top of the melt trail their further progress is blocked by icosahedral crystals which have nucleated ahead of them in the melt (Figure 15). Eady, Hogan, and Davies (13) have developed a relationship between the maximum growth velocity  $V_m$  in micrometers per second, the alloy composition  $x$  in wt% Mn, and the growth temperature  $T^*$  in degrees C of the dendrite tip for  $Al_6Mn$  dendrites;

$$V_m = (1/3)[659 + 27.9(x - 1.95)^{0.786} - T^*]^2 \quad (1)$$

In this expression,  $659 + 27.9(x - 1.95)^{0.786}$  is the liquidus temperature for  $Al_6Mn$ . At velocities slightly greater than that at which the dendrites can grow, there exists a narrow range of velocities in which coupled eutectic growth is seen, and Eady et al. correlate the eutectic growth velocity  $V_e$  to the temperature difference  $\Delta T$  between the interface temperature and the eutectic temperature (659°C) by

$$V_e = 100(\Delta T)^2 \text{ (micrometers/sec)} \quad (2)$$

At the boundary between the dendrite growth region and the coupled eutectic growth region, we can set  $V_e = V_m$ , and using  $T^* = 659 - \Delta T$  we can reformulate Eq. (1) to predict the limiting velocity for dendritic growth as a function of alloy composition,

$$V = 0.0232 (x - 1.95)^{1.572} \text{ cm/sec} \quad (3)$$

Although the expressions of Eady et al. were based on alloys containing

< 5 wt% Mn, we find that the transition from intermetallic phase growth to  $\alpha$ -Al, which is seen for alloys containing up to 14 wt% Mn as shown in Figure 7, is correctly predicted by Eq. (3). In view of this agreement, we conclude that their analysis gives a good description of the growth process of  $\text{Al}_6\text{Mn}$  and Eq. (2) can be used to give a reasonable value for the temperature at the dendrite tips at the upper limit of dendrite growth. In the 18 wt% Mn alloy the limiting velocity is about 2.5 cm/sec, so  $\Delta T = 16^\circ\text{C}$  below the eutectic temperature. This point is indicated by an asterisk on the phase diagram (Figure 14) and serves as an estimate for the nucleation temperature of the icosahedral phase. Temperature gradients ahead of the advancing dendritic interface would tend to raise this estimate, while the growth of the icosahedral phase to a finite size would tend to lower this estimate. Although icosahedral is the dominant phase in electron beam melt trails scanned at high velocities, its growth velocity is less than the scan velocity. This can be deduced from examination of the melt trails in the Al-18 wt% Mn alloy. If the icosahedral phase could grow at several centimeters per second, then in the 2.5 cm/sec melt scans it would have shown at least some tendency to form elongated dendrite colonies similar to those of the adjacent  $\text{Al}_6\text{Mn}$  dendrites; no such elongated icosahedral dendrite colonies are seen. Conversely, to reach the observed radius of  $5 \times 10^{-4}$  cm in the time available for growth in the 50 cm/sec melt scan, the growth velocity could not have been much less than about 1 cm/sec. The icosahedral crystals show little change in morphology as the scan rate was changed from 2.5 to 50 cm/sec, indicating that their growth rate did not increase significantly. The growth rate in all cases must have been approximately 1 cm/sec, which is comparable to the velocity deduced by Shechtman et al (1) in melt-spun ribbons of Al-25 wt% Mn. These

velocities are slow enough that an equilibrium distribution of solute at the solid-liquid interface can be expected [17]. These crystals must have grown in a liquid with substantial undercooling, because they show no apparent response to the large temperature gradients which were present. For example, the gradient near the edge of the melt pool may be estimated to be approximately  $5 \times 10^3$  C/cm, so that there would be a 5°C temperature difference across a crystal 10  $\mu$ m in diameter. Because the crystals appear to be unaffected by this temperature difference, their growth must be driven by a supercooling which is considerably greater than 5°C. Because the crystals have such slow growth rates in the presence of a large supercooling, we must conclude that the growth is limited by solute diffusion or kinetics rather than local heat flow. Growth velocities of this order of magnitude probably are typical for this phase at the temperatures at which nucleation occurs, and thus would not be greatly altered by changes in the cooling rate. Higher cooling rates would, however, produce a finer grain size by increasing the number of nuclei. If the growth rate is limited primarily by solute diffusion rather than interfacial kinetics, greater growth rates should be possible at higher manganese concentrations, where the composition change accompanying solidification is probably smaller.

Efforts to produce a larger grain size by decreasing the cooling rate and thus the number of nuclei are frustrated by the resulting growth of the  $\gamma$  phase. This phase has in many cases been seen as an oriented overgrowth on the icosahedral phase and its increasing dominance in low speed electron beam melt scans makes particularly clear the difficulty of trying to grow large icosahedral crystals.

The results reported here indicate that in binary Al-Mn alloys, single

phase icosahedral material may be produced only at compositions close to that of  $\text{Al}_4\text{Mn}$  and that at these compositions extremely high cooling rates are needed to avoid formation of the decagonal phase. One way to produce larger crystals of the icosahedral phase would be to add other chemical constituents which would stabilize this phase relative to the phases with which it competes, especially the decagonal phase. We have recently found (19) that melt spun ribbons of Al containing 33 wt% Mn and 5 wt% Si contained less than 1% aluminum phase and no decagonal phase. Further investigation of this ternary system may show the way to produce larger icosahedral crystals.

## VI. Conclusions

1. The icosahedral phase in Al-Mn alloys can grow with a range of compositions. It grows competitively with the decagonal phase, which progressively replaces it with increasing manganese concentrations or lower solidification velocities.
2. The icosahedral phase forms by nucleation and growth within a supercooled liquid, but its growth velocity is usually only about 1 cm/s.
3. The preferred dendrite growth direction of the icosahedral phase is along the 3-fold symmetry axis.

## Acknowledgement

The authors thank DARPA for financial support of this work. The authors also thank J. W. Cahn for useful discussions and D. Carrick and C. Brady for metallographic specimen preparation.

## References

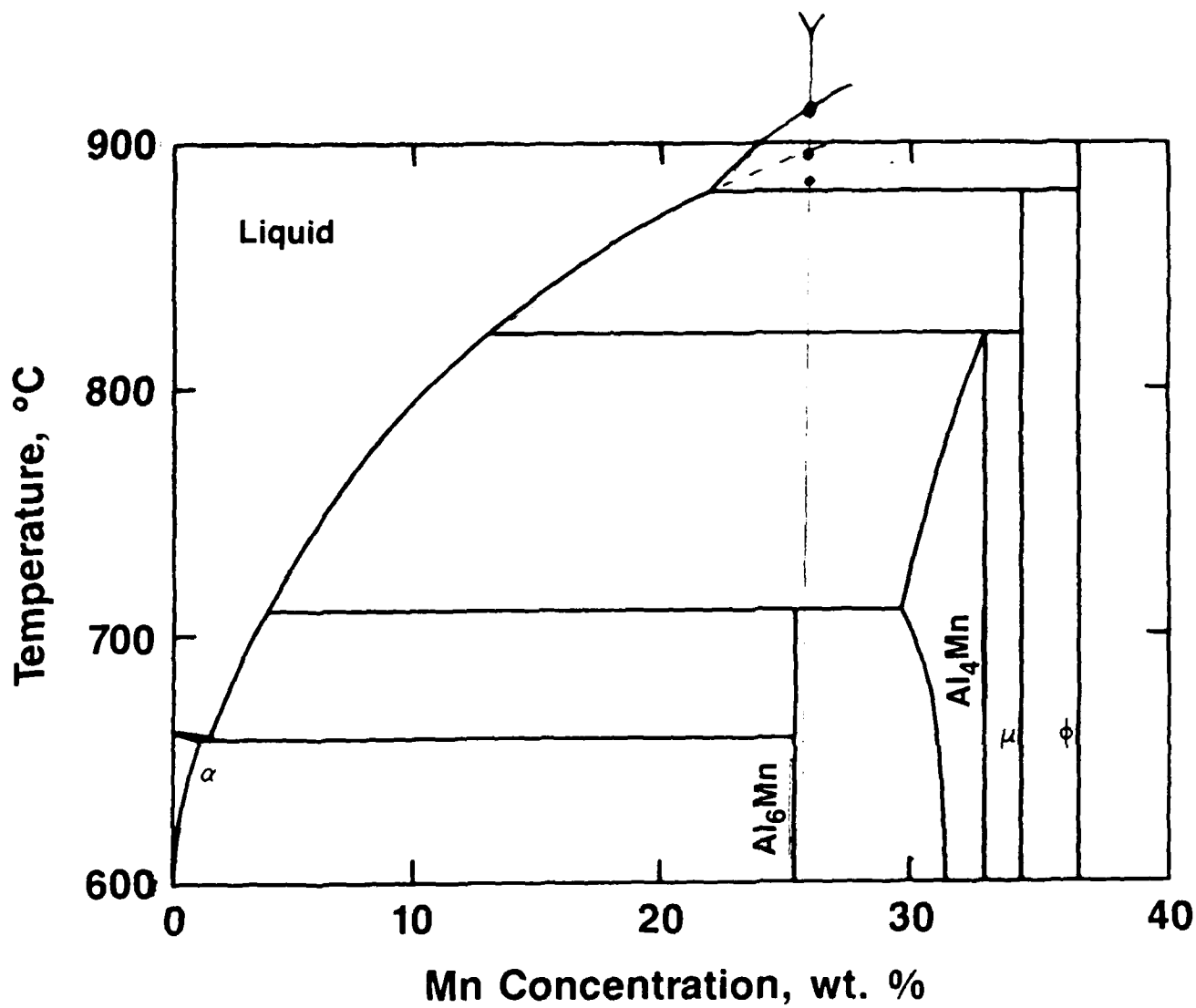
1. D. Shechtman, I. Blech, D. Gratias, and J. W. Cahn: *Phys. Rev. Lett.*, 1984, vol. 53, p. 1951.
2. H. W. L. Phillips: *J. Inst. Metals*, 1943, vol. 69, p. 275.
3. M. A. Taylor: *Acta. Met.*, 1960, vol. 8, p. 256.
4. J. A. Bland: *Acta Cryst.*, 1958, vol. 11, p. 236.
5. T. Godecke and W. Koster: *Z. Metall.*, 1971, vol. 62, p. 727.
6. J. H. Perepezko and W. J. Boettinger: *Mat. Res. Soc. Symp. Proc.*, 1983, vol. 19, p. 223.
7. W. Hofmann: *Aluminium Berlin*, 1938, vol. 20, p. 865.
8. A. J. McAllister: 1985, unpublished research, NBS.
9. H. Jones: *Aluminium*, 1978, vol. 54, p. 274.
10. D. Shechtman, R. J. Schaefer, and F. S. Biancaniello: *Met. Trans.*, 1984, vol. 15A, p. 1987.
11. D. Shechtman and I. Blech: *Met. Trans.*, 1985, vol. 16A, p. 1005.
12. A. D. I. Nicol: *Acta. Cryst.*, vol. 6, p. 285.
13. J. A. Eady, L. M. Hogan, and P. G. Davies: *J. Aust. Inst. Met.*, 1975, vol. 20, p. 23.
14. L. Bendersky, R. J. Schaefer, F. S. Biancaniello, W. J. Boettinger, M. J. Kaufmann and D. Shechtman: *Scripta Met.*, 1985, vol. 19, p. 909.
15. L. Bendersky: *Phys. Rev. Lett.* (submitted).
16. J. W. Cahn, D. Shechtman, and D. Gratias: 1985, unpublished research, NBS.
17. M. J. Aziz: *J. Appl. Phys.*, 1982, vol. 53, p. 1158.
18. L. A. Bursill and Peng Ju Lin: (May-June 1985), in press *Nature*.
19. R. J. Schaefer, W. J. Boettinger, F. S. Biancaniello, D. Shechtman and L. Bendersky: APS March Meeting, Baltimore, MD, March 1985.

### Figure Captions

- Figure 1. A portion of the Al-Mn phase diagram. The abundance of the phases found in melt spun ribbons, as a function of composition, is shown below the diagram.
- Figure 2. Diffraction patterns of phases observed in this study, for Cu K $\alpha$  radiation.
- Figure 3. Variation of d spacing for Al (111) and icosahedral (300000) in melt spun ribbons of different compositions.
- Figure 4. Typical TEM appearance of icosahedral phase, showing coral-like branches and mottled contrast. Al-25 wt% Mn melt-spun ribbon.
- Figure 5. Typical TEM appearance of the decagonal phase, showing faulted structure and blocky faceting. (a) shows general view and (b) shows detail of a single particle.
- Figure 6. Mapping of primary phases in electron beam melts of different velocity and composition. In the icosahedral + decagonal (T) region, the numbers indicate the relative fraction of the intermetallics which are icosahedral, from x-ray intensities.
- Figure 7. Microstructure of 0.25 cm/s melt scan on an Al-25 wt% Mn alloy showing large plates of primary intermetallic with subsequent overgrowth of Al<sub>6</sub>Mn and terminal solidification of Al.
- Figure 8. Bundles of intermetallic platelets in 2.5 cm/s melt scan on Al 25 wt% Mn alloy.
- Figure 9. Electron beam melt scans on Al-14 wt% Mn at (a) 1.0, (b) 2.5, and (c) 5 cm/s, showing the transition from primary intermetallic Al<sub>6</sub>Mn to supersaturated Al. The deeper melts were the homogenization pre-melts, and the direction of scan on the shallower, controlled-velocity, melts was toward the observer.
- Figure 10. Crystals with conspicuous 5-fold symmetry in the Al-18 wt% Mn alloy. Similar crystals were found at scan velocities between 2.5 and 50 cm/s: the ones pictured here were in the overlapping melt spots used to refine the surface microstructure.
- Figure 11. A crystal of the same type as shown in Figure 12, but aligned with a two-fold symmetry axis normal to the metallographic section, compared to the icosahedral stereographic projection.
- Figure 12. A model of the icosahedral crystallites as found in Al-18 wt% Mn electron beam melts.
- Figure 13. TEM of crystallites in Al-18 wt% Mn alloy. Electron diffraction confirms them to be icosahedral.

Figure 14. Hypothetical solidus and liquidus curves for the icosahedral phase. The asterisk indicates the point at which nucleation occurs in an Al-18 wt% Mn alloy during electron beam surface melting.

Figure 15. Icosahedral phase grains (left), nucleated in the melt, blocking the advance of  $Al_6Mn$  dendrites growing up from the bottom of an electron beam melt pool. The electron beam was scanned at 2.5 cm/sec across the surface of an Al-18 wt% Mn alloy.



Phase Abundance in Melt-Spun Ribbons

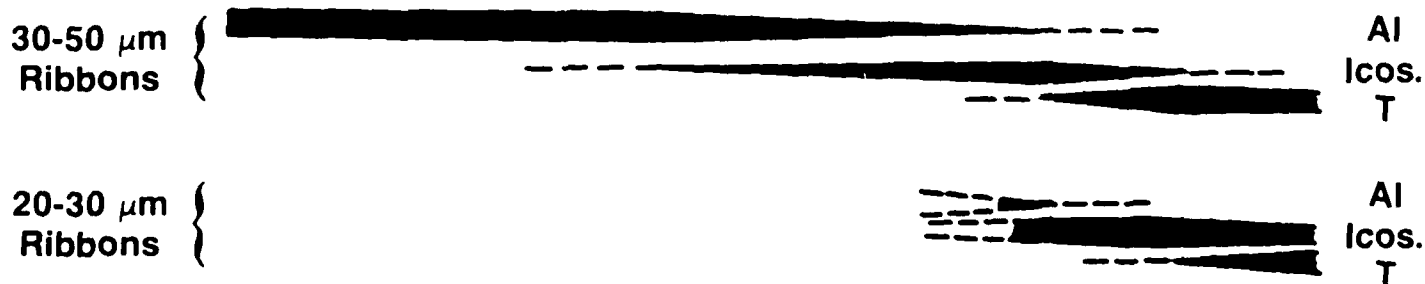


Fig. 1

Diffracted Intensity, arbitrary units

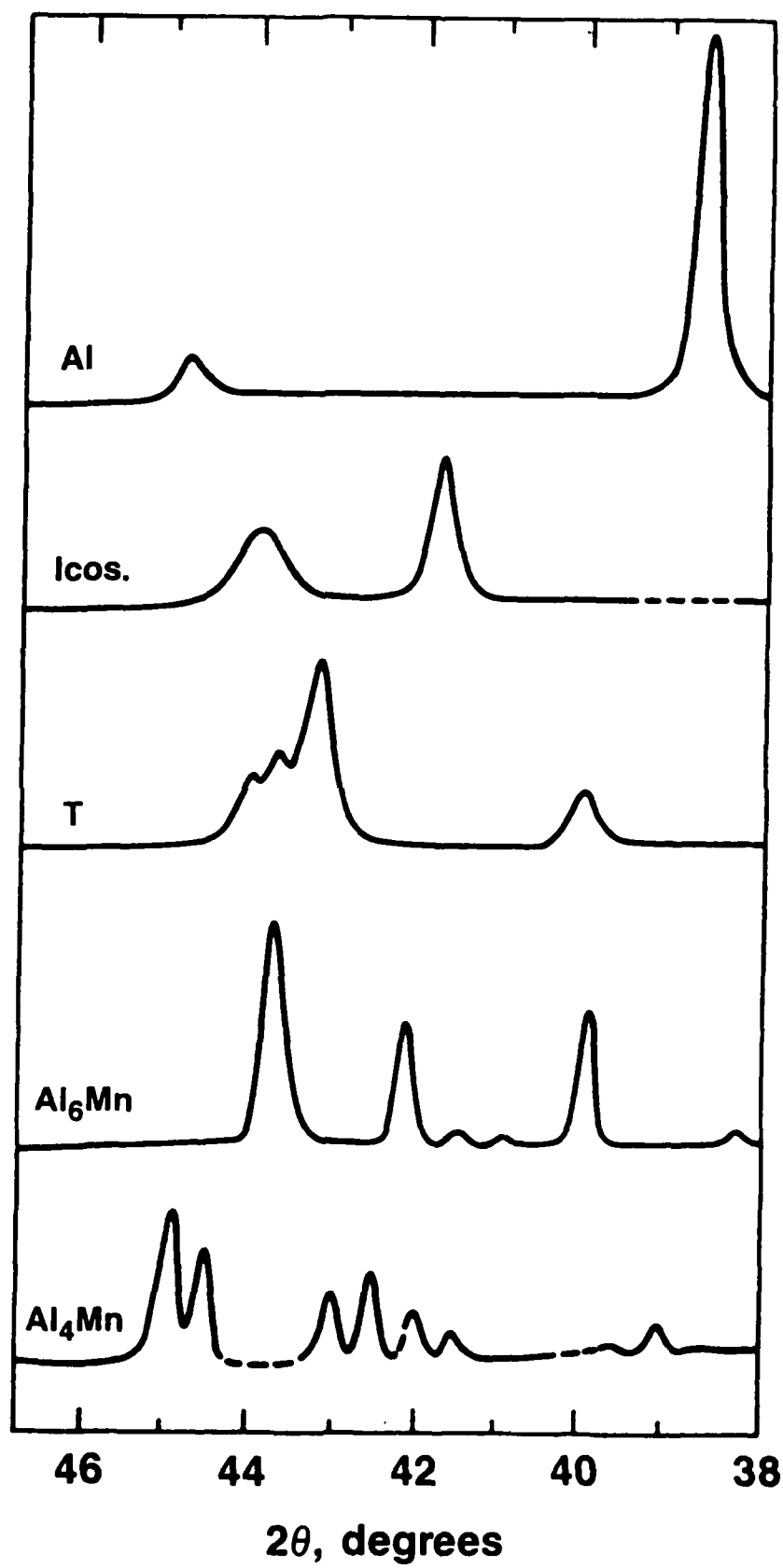


Fig. 2

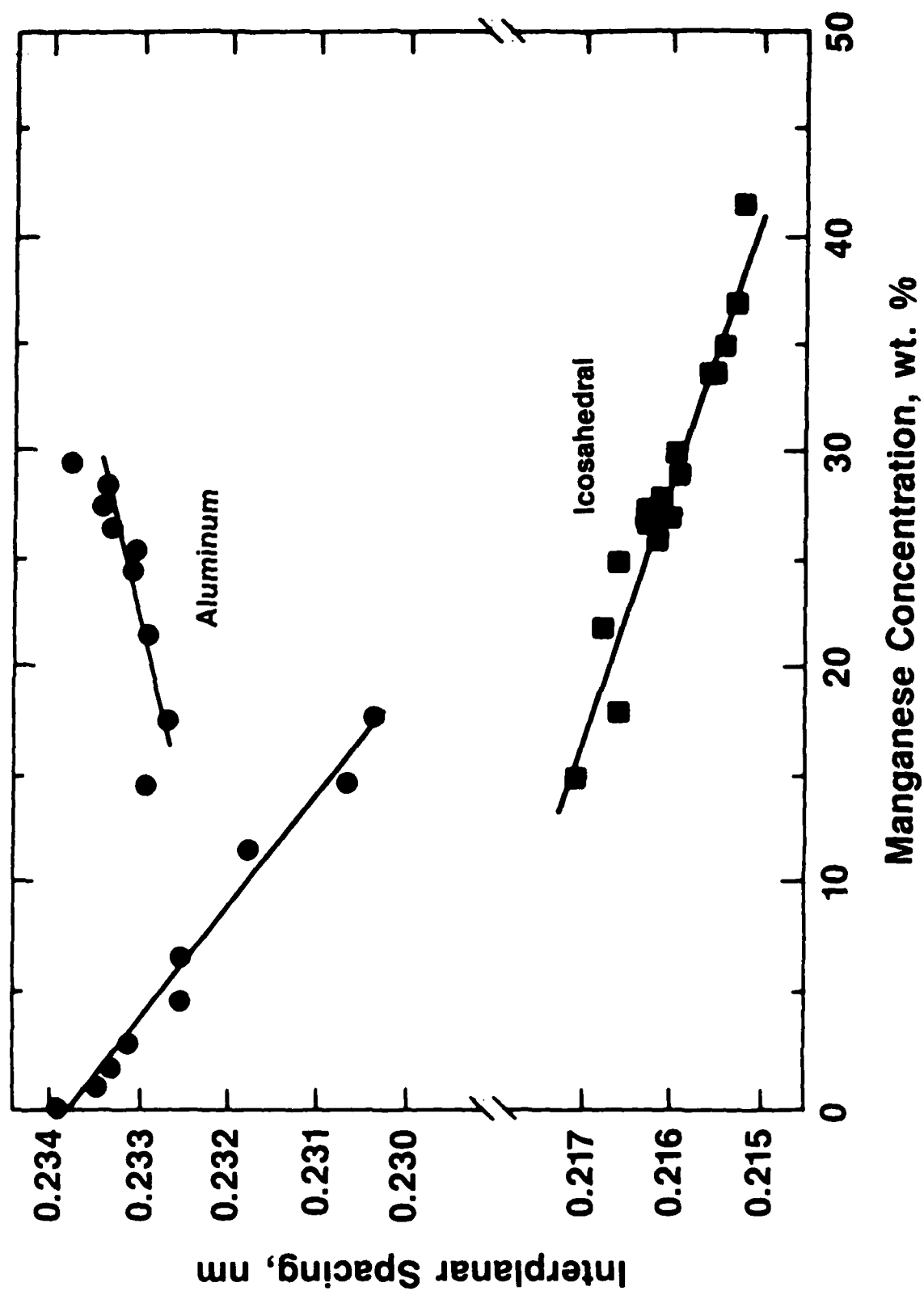


Fig. 3

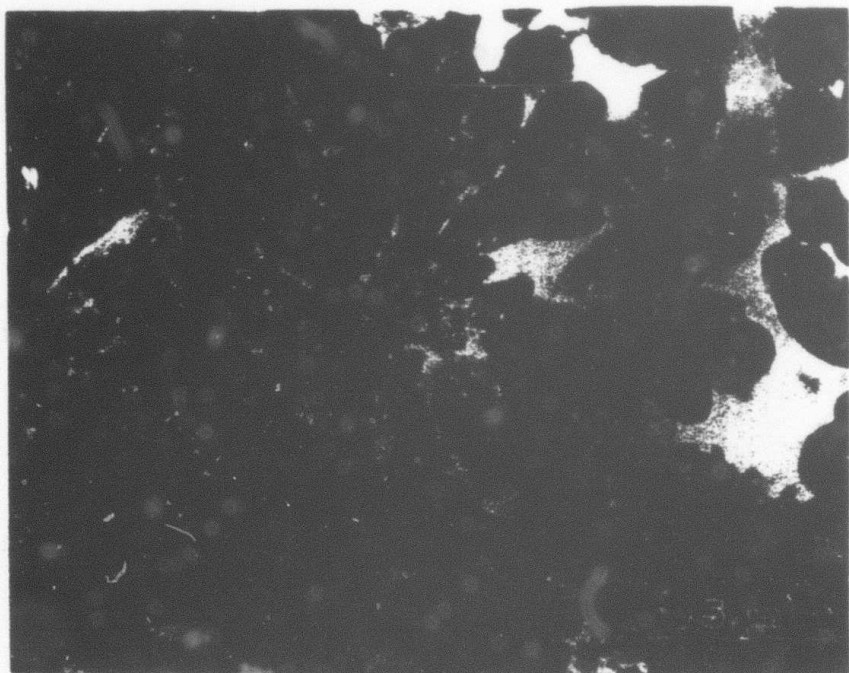
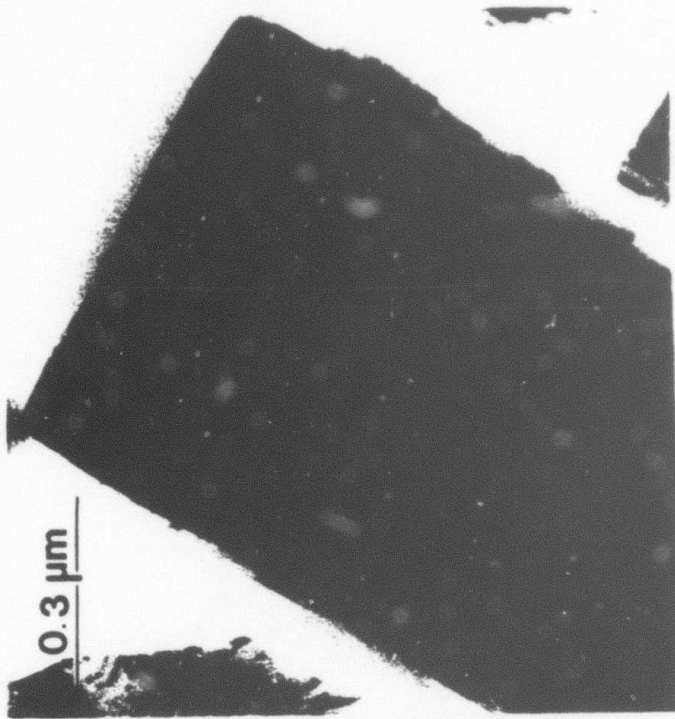


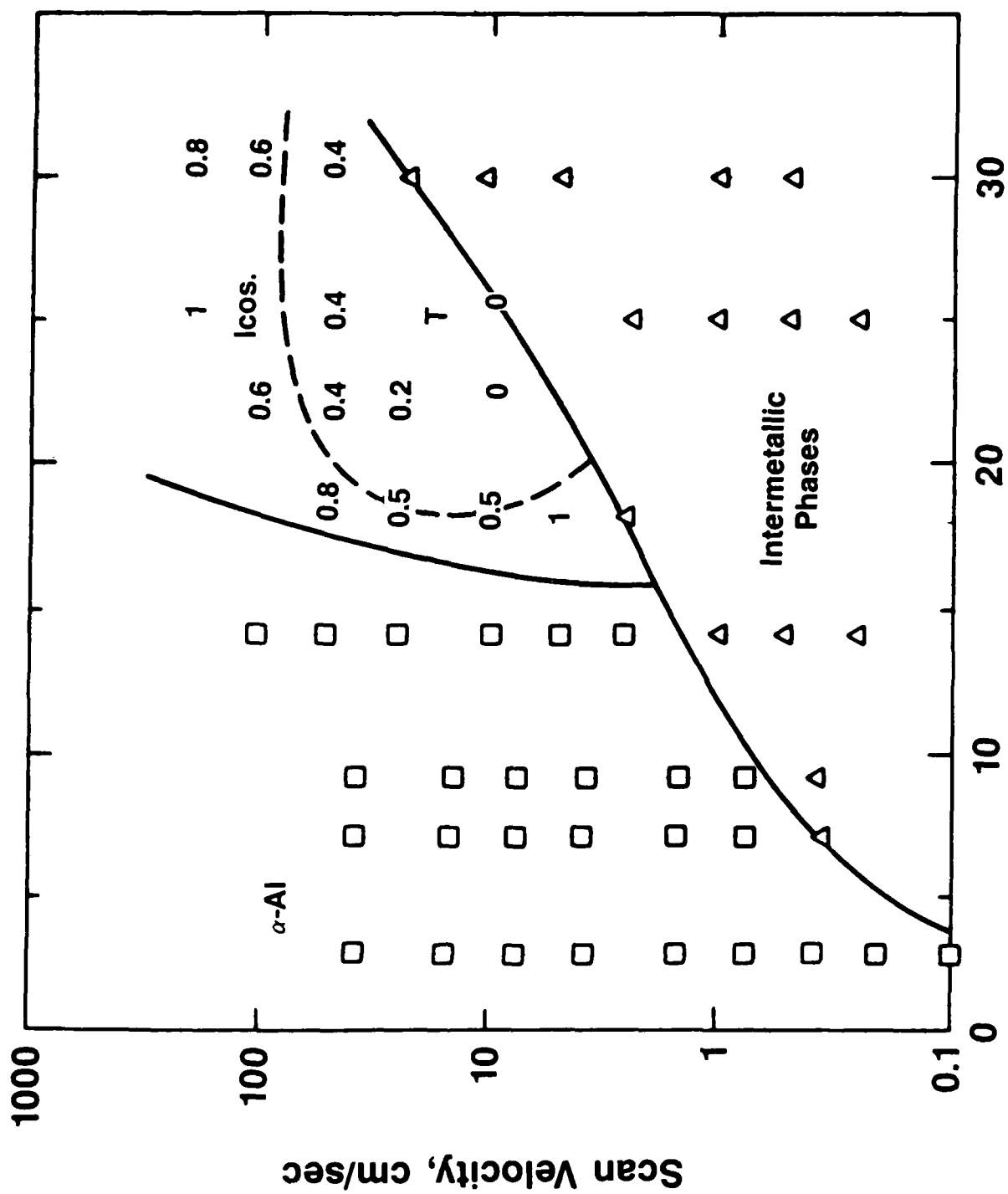
Fig. 4



(b)

(a)

Fig. 5



Manganese Concentration, wt. %



Fig. 7

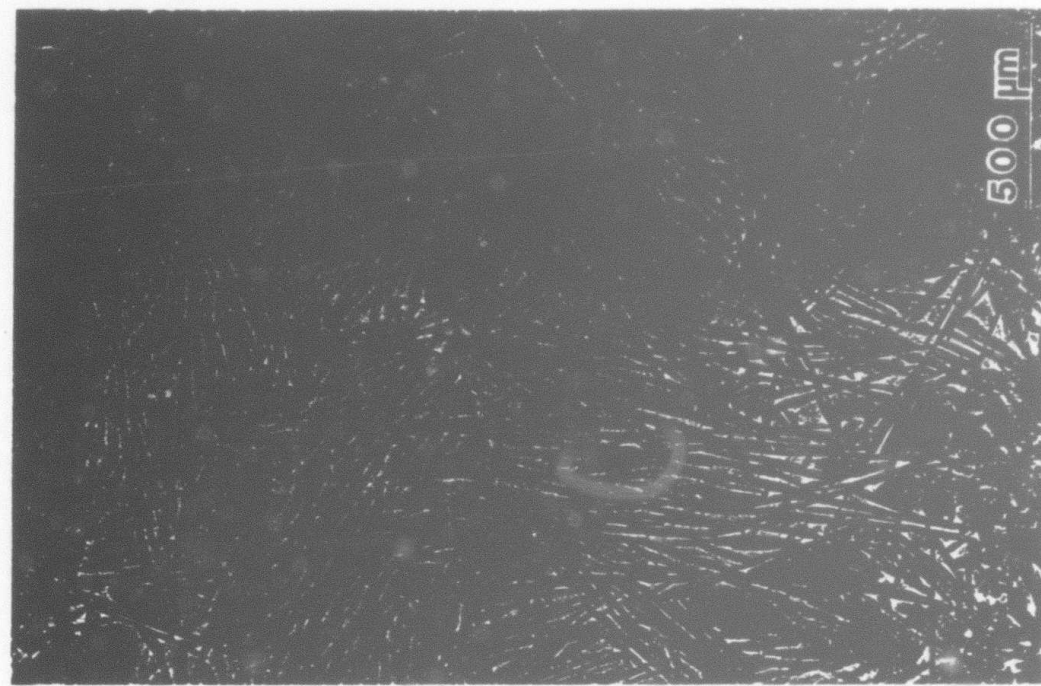


Fig. 8



(a)



(c)



(b)

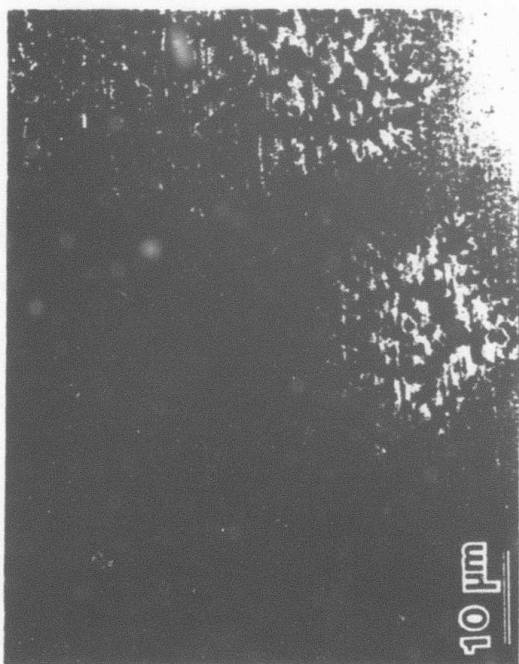


Fig. 10

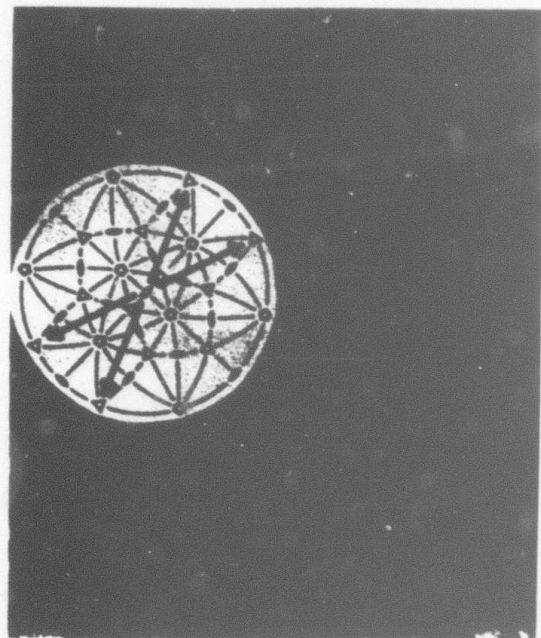


Fig. 11

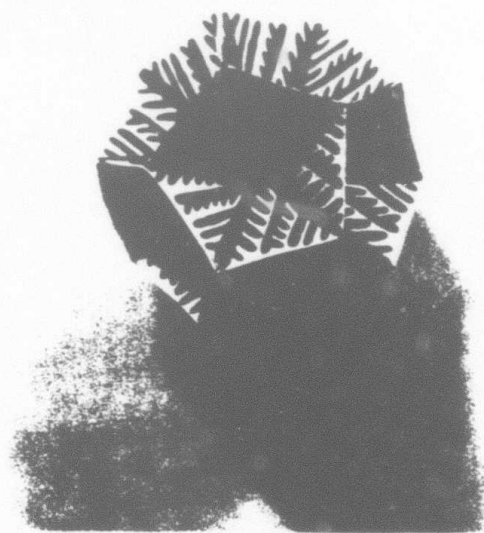


Fig. 12

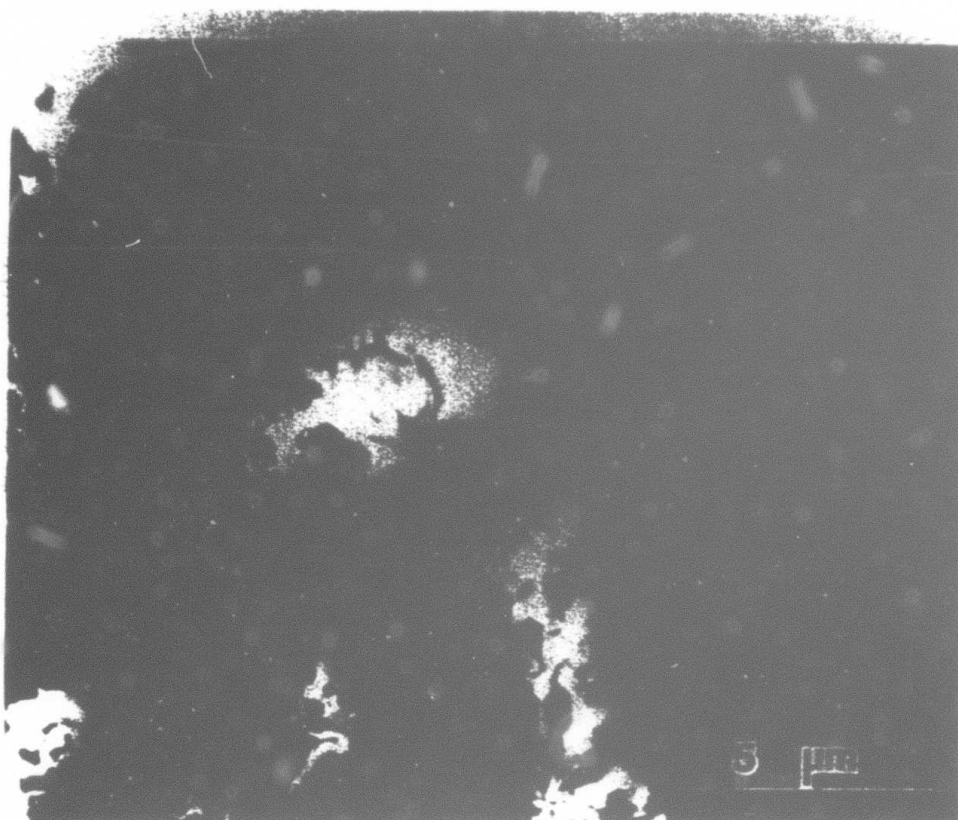


Fig. 13

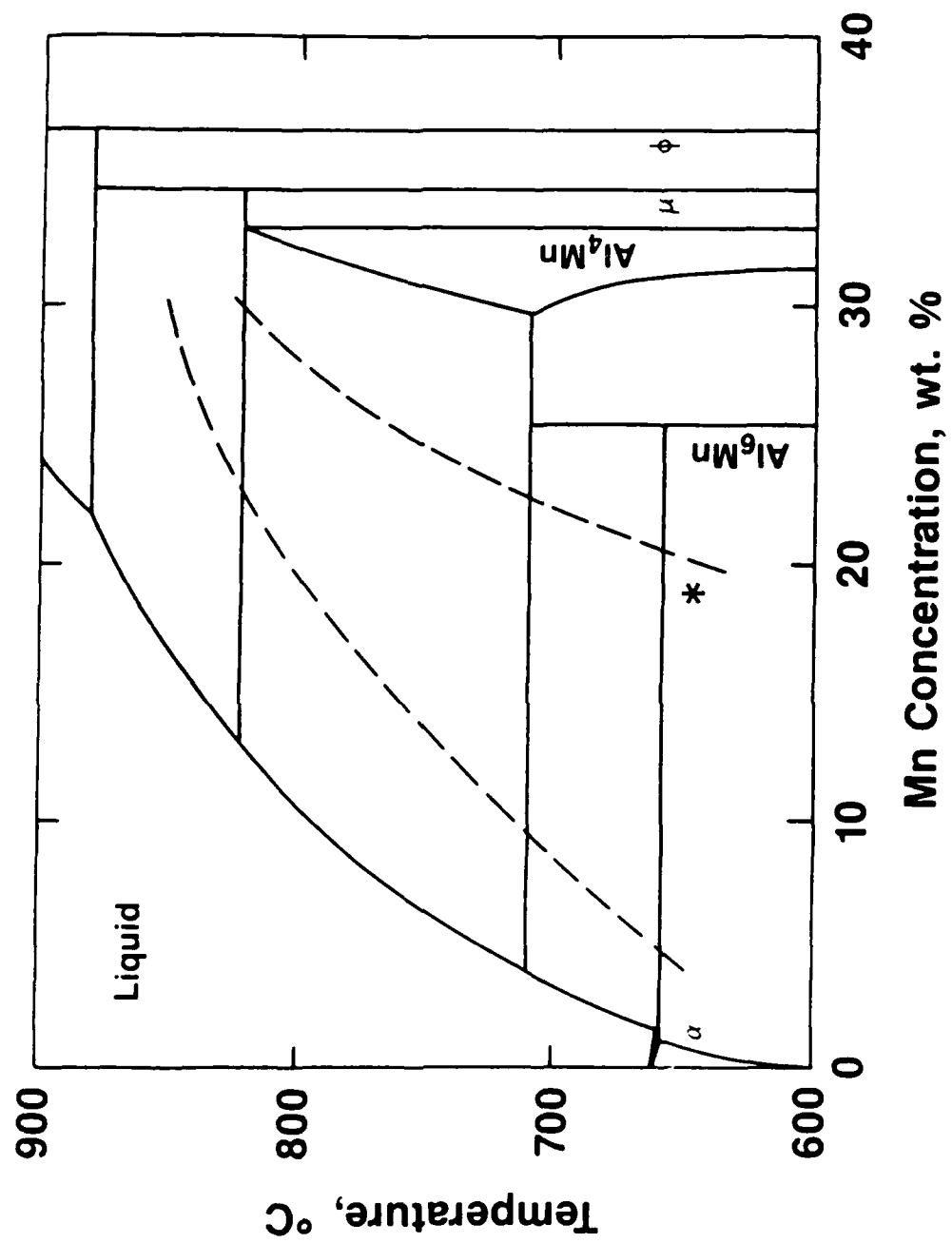


Fig 14

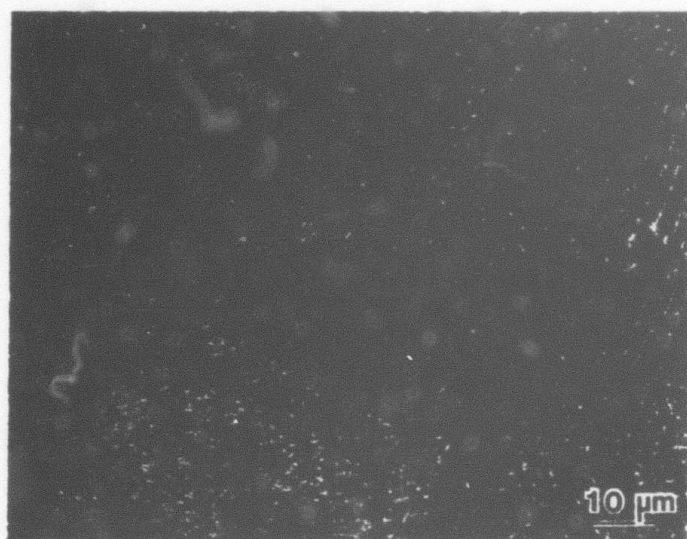


Fig. 15

## Microsegregation in Rapidly Solidified Ag-15 wt% Cu Alloys

W. J. Boettinger, L. A. Bendersky\*, S. R. Coriell, R. J. Schaefer,  
and F. S. Biancaniello

Metallurgy Division  
National Bureau of Standards  
Gaithersburg, MD 20899

### Abstract

Spacings and composition profiles of cellular structures formed in Ag-15 wt% Cu alloys at growth rates between 0.1 and 18 cm/s are measured. At the highest rates the cell spacings exceed the characteristic diffusion length  $D/V$  (ratio of liquid diffusion coefficient to growth rate) by a factor of ten. The rate of increase of the average cell composition with growth velocity is larger than predicted by existing diffusion models of the cell tip. Increases in cell compositions beyond the Ag solidus retrograde are accounted for quantitatively by the use of non-equilibrium interface conditions (solute trapping).

### Introduction

One of the most important microstructural benefits of solidification at high rates compared to conventional rates is a reduction in microsegregation. Despite the fact that completely microsegregation-free crystalline microstructures are obtained for some alloys under certain conditions (1), many commercially important rapidly solidified crystalline alloys exhibit very fine cellular microsegregation patterns. The amount of solute incorporated into cell interiors has a direct influence on the volume fraction of intercellular phases (inclusions) and subsequent precipitation in the cell interiors during thermomechanical treatment.

\* Materials Science and Engineering Department  
Johns Hopkins University  
Baltimore, Maryland 21218  
J. of Crystal Growth (Accepted)

Several authors (2-6) have measured cellular solute profiles or second phase content in rapidly solidified alloys produced with either unknown or estimated growth rates. These estimates rely either on assumed values of the heat transfer coefficient between the alloy and the quenchant or on extrapolation of expressions which relate microstructural scale (e.g., dendrite arm spacing) to cooling conditions under conventional solidification conditions. In the present work cellular solute profiles are measured in samples in which the growth rate is determined in a more direct fashion using the electron-beam melting and resolidification technique.

#### Experimental Procedure

Samples were prepared using one dimensional scans of a 1 mm diameter focussed electron beam across the surface of a 4 mm thick Ag-15 wt% Cu plate at speeds of 0.1, 0.6, 2.5, 12 and 18 cm/s. At these speeds the dimensionless parameter,  $V_s a / 2\alpha$ , is less than unity where  $V_s$  is the scan speed,  $a$  is the beam radius and  $\alpha$  is the thermal diffusivity of the plate ( $\sim 1 \text{ cm}^2/\text{s}$  for Ag). Mehrabian et al. (7) have calculated that under these conditions the melt puddle is nearly hemispherical and thus the growth direction and solidification speed of the resolidified alloy near the top center of the melted region are nearly parallel and equal to the electron beam scan velocity. Metallographic examination of samples in this range previously established that the growth velocity is generally no more than 15% slower than the scan speed (8).

Half disks cut transverse to the scan direction were prepared for analytical electron microscopy by ion milling on a liquid nitrogen cold stage. Compositions were quantified using the Cliff-Lorimer ratio technique (9) for the  $L_{\alpha}$  and  $K_{\alpha}$  x-rays for Ag and Cu, respectively, with a constant determined experimentally from measurements on a homogeneous Ag-28 wt% Cu alloy, rapidly solidified in

a partitionless manner at a velocity of 70 cm/sec (8). The thin-film criterion (9) is satisfied for both characteristic x-rays for specimen thicknesses less than 153 nm as was the case for our specimens. The spatial resolution was determined using the beam broadening equation (9). For a foil thickness of 150 nm, the beam broadening was calculated to be 42 nm, and the total broadening for the probe size of 5 nm used in our experiments was 42.2 nm.

The range of solidification velocities and the alloy composition of Ag-15 wt% Cu were chosen for detailed analysis of microsegregation based on previous experience with this alloy using the electron beam solidification technique (8). Above a velocity of ~18 cm/s this alloy does not form cellular structures. A banded structure, which can be considered as a part of the transition from the cellular to the microsegregation-free structure, occurs between ~18 cm/s and ~200 cm/s. Above 200 cm/s significant solute trapping or velocity dependence of the partition coefficient is thought to occur.

A critical issue in the present experiments is to determine the degree of interfacial non-equilibrium (solute trapping) which occurs during cellular solidification. For this purpose the choice of Ag-15 wt% Cu alloys is particularly useful. The Ag-rich portion of the Ag-Cu phase diagram as assessed by Murray (10) is shown in Figure 1. The Ag-rich solidus exhibits a metastable retrograde calculated at 10 wt% Cu and 700°C. This retrograde composition is thought to be accurate to  $\pm 1$  wt% Cu (11). The existence of this retrograde precludes the formation of Ag-rich solid solution above 10 wt% Cu regardless of the interface temperature or liquid composition unless solute trapping occurs. Microsegregation profiles will be examined regarding this point.

## Results

Intercellular Constituent - Figure 2 shows transverse sections of cellular structures formed at 2.5 cm/s and 12 cm/s. The intercellular regions in these micrographs are typical of cells grown below and above ~2.5 cm/s, respectively. At low speeds the intercellular regions contain eutectic. At higher speeds single phase sheets of Cu-rich phase presumably continuous in the growth direction are found. The latter morphology occurs at velocities above 2.5 cm/s when the width of the intercellular region becomes less than ~20 nm. Qualitatively one also notes a decrease in the area fraction of intercellular constituent at higher rates. This fact is consistent with the increase in the average composition of Cu within the cell interiors described below.

Cell Spacing - Examination of TEM micrographs at the five growth rates yields the average cell spacing data shown in Figure 3. Also in Figure 3 is the characteristic diffusion length  $D/V$  plotted versus velocity where  $D$  is the liquid diffusion coefficient, here taken as  $2 \times 10^{-5} \text{ cm}^2/\text{s}$  (12). At 0.1 cm/s the cell spacing is only slightly greater than  $D/V$  whereas at high growth rates the cell spacing is larger than  $D/V$  by a factor of 10.

Microsegregation Profiles - Plots of composition versus distance across the center of transverse sections of cells formed at the five growth rates are shown in Figure 4. The cross-hatched regions represent intercellular material, either eutectic or Cu-rich phase. Data points within 40 nm of the intercellular Cu-rich regions have been neglected based on the estimate of the spatial resolution for chemical analysis described above.

Only the 0.1 cm/s sample has a profile which has the characteristic U-shape usually expected for cellular segregation at lower growth rates.

Profiles for the higher speeds seem irregular with no indication of a minimum composition at the cell center. Despite this irregularity the average composition across the cells increases with increasing growth rate from approximately 6.4 wt% Cu at 0.1 cm/s to ~12.6 wt% Cu at 18 cm/s. Figure 5 summarizes this trend. The mean composition as well as the maximum and minimum compositions for each profile are plotted against growth velocity. The compositions exceed the equilibrium solubility limit of 8.7 at% Cu for samples solidified above 1 cm/s. The samples solidified at 12 and 18 cm/s also exceed the Ag-solidus retrograde composition.

Inverse coring - A few composition profiles were obtained which contained a maximum in composition at the cell center. Such a profile is shown in Figure 6. Corresponding microstructures in polished and etched samples were occasionally found in SEM micrographs with a strongly etched core at the cell center as shown in Figure 7.

#### Analysis of Results

The prediction of microsegregation profiles in cellular structures is a formidable task. Two important aspects of the modeling problem are the choice of proper boundary conditions for the compositions and temperature at the liquid solid interface and the solution of the solute and thermal diffusion problems in the vicinity of the cellular interface. At slow solidification rates, the concept of local equilibrium is used to describe the temperatures and compositions at the liquid-solid interface. The diffusion problems are treated approximately by calculating the conditions at the cell tip (13-16) and applying a Scheil-type solute balance to determine full cross-cell solute profiles (13, 17). More recently, numerical techniques have been employed to determine the full solution to the moving boundary problem (18-20). These

techniques have been reviewed by Coriell, McFadden and Sekerka (21). Even these full solutions suffer from the problem of wavelength selection, i.e. what determines the cell spacing for a given set of growth conditions. In the present discussion we focus on the effect that non-equilibrium interface conditions have on cellular microsegregation profiles and the impact of the observation that cell spacings can greatly exceed the characteristic diffusion length for solidification.

Non-equilibrium Interface Conditions - Because cell compositions in the present experiments exceed the Ag-rich solidus retrograde composition, non-equilibrium interface conditions must be considered. One approach to modeling these interface conditions requires three equations which have been described by Aziz (22) and by Boettinger, Coriell and Sekerka (1). Using an atomistic diffusion model at the liquid solid interface, Aziz has shown that the ratio  $k$  of the solid and liquid compositions at the interface,  $C_S^*$  and  $C_L^*$ , can be expressed in terms of the equilibrium partition ratio  $k_E$  and the interface speed  $V$  by

$$k = \frac{k_E + \beta_0 V}{1 + \beta_0 V} \quad (1)$$

where  $\beta_0$  is a kinetic parameter. The second equation is obtained by the usual assumption that the interface speed is a function of the thermodynamic driving force  $\Delta G$  for solidification. Turnbull and Bagley (23) give for this equation

$$V = V_0(1 - \exp(\Delta G/RT_I)) \quad (2)$$

where  $V_0$  is a second kinetic parameter,  $R$  is the gas constant and  $T_I$  is the interface temperature. The third equation relates  $\Delta G$  to  $T_I$ ,  $C_L^*$  and  $C_S^*$  through the expression

$$\Delta G = \Delta u_1(1 - C_S^*) + \Delta u_2 C_S^* \quad (3)$$

where  $\Delta u_1$  and  $\Delta u_2$  are the differences in chemical potential between solid and liquid for the compositions and temperature at the interface. For pure metals or when  $k$  is assumed to be equal to  $k_E$ ,  $\Delta G$  is simply proportional to interface undercooling (1). However in the present case  $\Delta G$  is more complex. The chemical potential differences can be evaluated from a thermodynamic model of the alloy system of interest.

Given this thermodynamic model and values for the kinetic parameters  $v_0$  and  $V_0$ , one can calculate, for example,  $C_S^*$  and  $T_I$  as functions of  $C_L^*$  and  $V$ . Examples of plots of this type are given in reference (1). Aziz (24) has recently plotted  $C_S^*$  vs.  $T_I$  and  $C_L^*$  vs.  $T_I$  for fixed values of  $V$ . Such a diagram is used just like the equilibrium phase diagram to specify interface conditions at any velocity of interest. In fact at  $V = 0$  these two curves are precisely the equilibrium solidus and liquidus for the phase of interest. At very high velocities, these two curves become one at temperatures and composition below the  $T_0$  curve. This situation corresponds to partitionless solidification (1).

The effect of growth velocity on the maximum solubility of Cu in the Ag-rich phase is of primary interest for this paper. How does the retrograde feature of the  $C_S^*$  vs.  $T_I$  plot depend on  $V$ ? Figure 8 shows the Ag solidus along with  $C_S^*$  vs.  $T_I$  plot for  $V = 2.5, 12$  and  $18$  cm/s corresponding to the growth rates for the higher speed experiments reported herein. If shown in Figure 8, the  $C_L^*$  vs.  $T_I$  plots would be indistinguishable from the liquidus for these velocities. The parameter  $V_0$  has been taken as the speed of sound in liquid metals,  $2 \times 10^5$  cm/s, in accordance with the model of collision limited growth (25). Such a model seems appropriate for a disordered close-packed

crystal structure. The parameter  $a_0$  in the Aziz model is  $a_0/D_i$  where  $a_0$  is the interatomic dimension here taken as 0.3 nm and  $D_i$  is the interface solute diffusivity. Little is known about  $D_i$  except that it is most likely less than the liquid diffusivity. Hence,  $a_0$  is greater than  $1.5 \times 10^{-3}$  s/cm ( $1/a_0 < 667$  cm/s). Experimental evidence (8) has shown that microsegregation-free structures are obtained in Ag-15 wt% Cu by solute trapping at 200 cm/s. Therefore we use  $1/a_0$  as 200 cm/s for the curves shown in Figure 8.

The  $C_S^*$  vs.  $T_I$  plot shows a retrograde composition of 12.4 wt% Cu for  $V = 12$  cm/s and 13.4 wt% Cu for  $V = 18$  cm/s. Hence according to this non-equilibrium interface model, a planar interface for an alloy of bulk composition 15 wt% Cu growing at 12 or 18 cm/s would form a solid with a maximum composition of 12.4 or 13.4 wt% Cu, respectively. For a cellular interface, the composition of cells would be less than this value due to lateral diffusion of solute in the liquid ahead of each cell. The extent of this lateral diffusion is discussed below. However, the values of 12.4 and 13.4 wt% Cu serve as maximum bounds which are consistent with the data shown in Figure 5.

Lateral solute diffusion at the cell tip - Without including the non-equilibrium interface conditions described above, various theories predict that increasing the solidification rate leads to an increase in the cell compositions, including an increase at the cell centers. We now examine two theories: Burden and Hunt (BH) and Ivantsov/Marginal Stability (I/MS).

According to BH (14) the composition at the center of a cell  $C_S^{tip}$  can be expressed in terms of the growth rate  $V$  and liquid temperature gradient  $G_L$  by

$$C_S^{tip} = k_E C_0 (1 - a + b) \quad (4)$$

where

$$a = G_L D / m_L V C_0 \quad (5)$$

and

$$b^2 = -2T_m^r(1 - k_E)V/m_L DC_0 \quad (6)$$

with  $m_L$  the liquidus slope,  $C_0$  the alloy composition and  $T_m^r$  the capillarity constant (ratio of liquid solid surface tension to entropy of fusion per unit volume). For values of the materials parameters appropriate to liquid of composition Ag-15 wt% Cu, viz.,  $m_L = -8\text{K/wt\%}$ ,  $k_E = 0.37$ ,  $D = 2.1 \times 10^{-5} \text{ cm}^2/\text{s}$  and  $T_m^r = 1.5 \times 10^{-5} \text{ Kcm}$ , the term involving the temperature gradient can be neglected for the velocities of interest in the present experiments. The resulting dependence of  $C_S^{\text{tip}}$  on  $V$  is shown in Figure 5. Clearly the data for the composition at the cell centers rise faster with increasing growth rate than predicted by BH. Inclusion of the retrograde nature of the equilibrium solidus, which requires  $k_E$  to decrease with increasing solute buildup at the interface, further increases the discrepancy between BH and the data. On the other hand, use of a non-equilibrium value of  $k = 0.42$  obtained using eqn. (1) for  $V = 18 \text{ cm/s}$  and  $1/\rho_0 = 200 \text{ cm/s}$  in eqns. (4-6) predicts a value of  $C_S^{\text{tip}} = 8.5 \text{ wt\% Cu}$ . This value is still much less than the 12 wt% Cu experimentally observed as a minimum in cells formed at 18 cm/s.

The BH model employs the extremum assumption to specify a unique value of tip radius  $R$  (and hence tip undercooling or tip concentration) for a given growth rate. Recently, considerable success has been achieved in matching theory and experiment for dendritic growth in initially undercooled melts (26) and during directional solidification (27) using the Ivantsov paraboloid model of the tip combined with a marginal stability assumption to specify the tip radius ( $1/MS$ ). Using expressions for alloys obtained by Lipton, Glicksman and Kurz (28),  $R$  can be obtained as a function of  $V$  by solving the transcendental equation

$$R = 4\pi^2 T_m^2 [1 - (1 - k_E) \text{Iv}(P_C)] / [-2m_L P_C C_0 (1 - k_E)] \quad (7)$$

where  $P_C = VR/2D$ ,  $\text{Iv}(P_C) = P_C \exp P_C E_1(P_C)$  and  $E_1(P_C)$  is the first exponential integral of  $P_C$ . Then  $C_S^{\text{tip}}$  is given by

$$C_S^{\text{tip}} = k_E C_0 / [1 - (1 - k_E) \text{Iv}(P_C)]. \quad (8)$$

The form of eqn. (7) neglects the influence of the temperature gradient which is justified in cases where the alloy is concentrated (29) and includes a factor 2 in the denominator previously omitted (30). The predictions of I/MS for the same materials parameters as used for BH is also shown in Figure 5. Although the predicted cell composition is seen to rise faster with increasing growth rate than the BH prediction, it still lies significantly below the data. Inclusion of the non-constant  $k_E$  necessary to describe the solidus retrograde again only increases the discrepancy between the data and prediction. Using the non-equilibrium value of  $k = 0.42$  appropriate for  $V = 18$  cm/s as described above, I/MS predicts a value of 9.8 wt% for 18 cm/s. Hence I/MS including non-equilibrium interfacial effects is inadequate to describe the measured dependence of cell composition on growth velocity.

Failure of BH and I/MS should come as no surprise. Direct observation (31) and calculations (18-20) show that cell shapes are flatter than paraboloids. Hence increased levels of solute build up at the cell center. An interesting observation can be made by comparing the data with the prediction of eqn. (8), using values of  $P_C$  obtained by letting  $R$  be one half of the measured cell spacing  $\lambda_{\text{cell}}$  ( $P_C = V\lambda_{\text{cell}}/4D$ ). These values of  $P_C$  range from 0.3 for  $V = 0.1$  cm/s to 5.4 for  $V = 18$  cm/s and are much larger than  $P_C$  values calculated using Eqn. (7). The results compare quite favorably with the measured data as shown in Figure 6 and further underscore the problems that remain in the area of cellular growth.

Cell Spacings - Theoretical prediction of cell spacings is not yet possible. However, Coriell, McFadden and Sekerka have noted (21) that measured cell spacings often compare within a factor of two with  $\lambda_c$ , the wavelength at the onset of morphological instability obtained, for example, from eqn. 24 of ref. 21. For this comparison, the wavelength must be calculated for the composition at the onset of instability for the growth velocity and temperature gradient of the experiments. This composition may be quite different than the alloy composition. Generally  $\lambda_c$  is much less than  $D/V$  for low growth rates but increases to values greater than  $D/V$  as the growth rate increases.

Using the phase diagram and surface tension parameters for Ag-Cu given above and an estimated liquid temperature of  $10^4$  K/cm appropriate for surface melting (32), the  $\lambda_c$  values are 7.6, 3.5, 1.7, 0.75 and 0.59  $\mu\text{m}$  for the velocities of 0.1, 0.6, 2.5, 12 and 18 cm/s respectively at compositions of 0.15, 0.065, 0.088, 0.28 and 0.40 wt% Cu. By comparison with Figure 3, the  $\lambda_c$  values are 2-3 times the observed spacings.

Profile Shape - The irregular shape of the solute profiles for the higher speed samples precludes any detailed analysis of entire microsegregation profiles. While all of the profiles vary by  $\sim 2$  wt% Cu across the cells, when this variation is normalized to the average composition, we conclude that the profiles become more uniform or flatter with increasing growth rate. This increasing uniformity is most likely related to difficulty of lateral solute diffusion when the cell spacing significantly exceeds  $D/V$ . In fact the characteristic U-shaped profile is observed only for the sample solidified at 0.1 cm/s where the cell spacing essentially equals  $D/V$ . At slower solidification rates we would also expect U-shaped profiles.

Inverse Microsegregation Profiles - The origin of the solute-rich regions

observed in some cellular structures (Figures 7 and 8) is difficult to determine with certainty. In surface melting and resolidification using a moving heat source, the velocity of any point on the liquid solid interface, when followed in a direction perpendicular to the interface, accelerates from zero velocity at the bottom of the melted puddle to near the scan speed at the top of the puddle. This acceleration produces a gradient of cell spacings from the edge to the centerline of the resolidified region, i.e., the cell spacing must decrease from edge to center line. One mechanism by which cells can decrease their spacing is the formation of a solute-rich dimple or ridge near the cell center and subsequent splitting. The observed solute-rich regions in some cell centers may correspond to the initiation of this cell spacing reduction mechanism. Indeed, Coriell and McFadden (18) have found solute-rich centers in some calculations of cell shape.

A second possibility follows a model originally proposed by Kattamis (33) in microstructures produced in initially undercooled melts. The normal velocity of a cell tip is higher than the normal velocity of points away from the cell center. In the regime of solidification velocities where  $k$  depends on  $v$  strongly, more solute may be trapped at cell centers than at cell edges. Such a situation could presumably result in cell profiles as shown in Figures 6 and 7. However, at a growth rate of 0.1 cm/s significant non-equilibrium effects are not expected.

#### Conclusions

- (1) In Ag-15 wt% Cu alloys average composition of the cells of the Ag-rich phase increase from 6.4 wt% Cu at 0.1 cm/s to 12.6 wt% Cu at 18 cm/s.
- (2) Microsegregation profiles across cells are not U-shaped at growth rates above 0.6 cm/s.

(3) Cell spacings decrease from 2.5  $\mu\text{m}$  at 0.1 cm/s to  $\sim 0.25 \mu\text{m}$  at 18 cm/s. The smallest spacings exceed the characteristic liquid diffusion length  $D/V$  by a factor of 10.

(4) Increases in cell compositions beyond the Ag solidus retrograde at 10 wt% Cu for the highest speeds are accounted for quantitatively by the use of non-equilibrium interface conditions (solute trapping).

(5) The Burden-Hunt and Ivantsov/Marginal Stability models of tip composition underestimate the rate of increase of cell composition with growth rate.

#### Acknowledgement

The authors acknowledge the support of DARPA for this research. Helpful discussions with G. B. McFadden and R. F. Sekerka are recognized with gratitude.

## References

1. W. J. Boettinger, S. R. Coriell and R. F. Sekerka, *Mat. Sci. & Eng.* 65 (1984) 27.
2. L. J. Mazur and M. C. Flemings, *Proc. 4th Int. Conf. on Rapidly Quenched Metals*, Vol. 2, T. Maxumoto, Suzuki, eds., Japan Inst. of Metals, Sendai (1982) 1557.
3. T. Z. Kattamis and R. Mehrabian, *J. Mat. Sci.* 9 (1974) 1446.
4. T. F. Kelly, G. B. Olson and J. B. Vander Sande, in *Rapidly Solidified Amorphous and Crystalline Alloys*, B. H. Kear, B. C. Giessen and M. Cohen eds., North Holland, 1982, 343.
5. H. A. Palacio, M. Solari and H. Biloni, *J. Cryst. Growth* 73 (1985) 369.
6. J. A. Sarreal and G. J. Abbaschian, *Met. Trans. A*, submitted for publication.
7. S. Kou, S. C. Hsu and R. Mehrabian, *Met. Trans.* 6B (1981) 33.
8. W. J. Boettinger, D. Shechtman, R. J. Schaefer and F. S. Biancaniello, *Met. Trans* 15A. (1984) 55.
9. J. I. Goldstein, in: *Introduction to Analytical Electron Microscopy*, eds. J. J. Hren, J. I. Goldstein and D. C. Joy (Plenum Press, NY 1979) p. 83.
10. J. L. Murray, *Met. Trans.* 15A (1984) 261.
11. J. L. Murray, National Bureau of Standards, unpublished research (1984).
12. T. Yamamura and T. Ejima, *J. Japanese Inst. Met.* 37 (1973) 901
13. T. F. Bower, H. D. Brody and M. C. Flemings, *Trans. TMS-AIME* 226 (1966) 624.
14. M. H. Burden and J. D. Hunt, *J. Cryst. Growth* 22 (1974) 109.
15. W. Kurz and D. J. Fisher, *Acta Met.* 29 (1981) 11.
16. R. Trivedi, *J. Cryst. Growth* 49 (1980) 219.
17. M. Solari and H. Biloni, *J. Cryst. Growth* 49 (1980) 451.
18. G. B. McFadden and S. R. Coriell, *Physica D* 12 (1984) 253.
19. L. H. Ungar and R. A. Brown, *Physical Rev. B* 31 (1985) 5931.
20. D. G. McCartney and J. D. Hunt, *Met. Trans.* 15A (1984) 983.

21. S. R. Coriell, G. B. McFadden and R. F. Sekerka, *Ann. Rev. Mater. Sci.* 15 (1985) 119.
22. M. J. Aziz, *J. Appl. Phys.* 53 (1982) 1158.
23. D. Turnbull and B. G. Bagley, in *Treatise Solid State Chem.*, ed. N. B. Hannay (Plenum Press, NY 1975) Vol. 5, p. 513.
24. M. J. Aziz, Harvard University, unpublished research (1986).
25. F. Spaepen and D. Turnbull, in *Proc. 2nd Int. Conf. on Rapidly Quenched Metals*, eds. N. J. Grant and B. C. Giessen (MIT Press, Cambridge, MA 1976) Vol. 1, p. 205.
26. S. C. Huang and M. E. Glicksman, *Acta Met.* 29 (1981) 701, 707.
27. R. Trivedi and K. Somboonsuk, *Mat. Sci. & Eng.* 65 (1984) 65.
28. J. Lipton, M. E. Glicksman and W. Kurz, *Mat. Sci. & Eng.* 65 (1984) 57.
29. W. J. Boettinger and S. R. Coriell, in *Rapid Solidification Technologies*, ed. P. Sahm (NATO Ad. Res. Workshop, Amburg FGR) 1985, in press.
30. M. E. Glicksman, Rensselaer Polytechnic Institute, unpublished research (1985).
31. R. Trivedi, *Met. Trans.* 15A (1984) 977.
32. R. J. Schaefer and R. Mehrabian, *Mat. Res. Soc. Symp. Proc.* 13 (1983) 733.
33. T. Z. Kattamis, *Z. Metallkunde* 61 (1970) 856.

### Figure Captions

- Figure 1. Ag-rich portion of the Ag-Cu phase diagram (10). Dashed lines are the metastable extensions of the liquidus and solidus for the Ag-rich phase. Note the retrograde in the metastable solidus at ~10 wt% Cu.
- Figure 2. Transverse sections of cellular structure in Ag-15 wt% Cu.  
(a) Solidified at 2.5 cm/s. TEM (darkfield). Note intercellular eutectic.  
(b) Solidified at 12 cm/s. TEM.  
(c) Solidified at 12 cm/s. TEM. High magnification of intercellular regions which are single phase Cu-rich solid solution.
- Figure 3. Average cell spacing versus solidification velocity for Ag-15 wt% Cu alloys. Shown for comparison is a plot of  $D/V$  versus  $V$ .
- Figure 4. Microsegregation profiles (composition versus distance) measured by STEM across transverse sections of cells in Ag-15 wt% Cu alloys solidified at the indicated velocities. The cross-hatched regions represent intercellular material, either eutectic or Cu-rich phase. The average composition of the Ag-rich phase increases with velocity.
- Figure 5. Average composition of the cells of the Ag-rich phase as a function of solidification velocity. The bars at each velocity represent the range of composition observed for each profile shown in Figure 4. Shown for comparison are the alloy composition  $C_0$ , the equilibrium Ag phase solubility limit (at the eutectic temperature), the Ag solidus retrograde composition, and predictions of the BH (Burden-Hunt) and I/MS (Ivantsov/Marginal stability) approaches to modelling cell compositions.
- Figure 6. Microsegregation profile of a cell solidified at 0.1 cm/s showing a solute-rich region at the cell center.
- Figure 7. SEM micrograph of transverse section of cells solidified at 0.1 cm/s etched to reveal solute-rich cores.
- Figure 8.  $C_S^*$  versus  $T_I$  plots for solidification velocities of 2.5, 12 and 18 cm/s obtained as solutions to Equations 1-3 for thermodynamic parameters appropriate for Ag-Cu alloys and kinetic parameters  $a_0 = 5 \times 10^{-3}$  s/cm and  $V_0 = 2 \times 10^5$  cm/s. The equilibrium solidus (stable and metastable parts) is also shown.

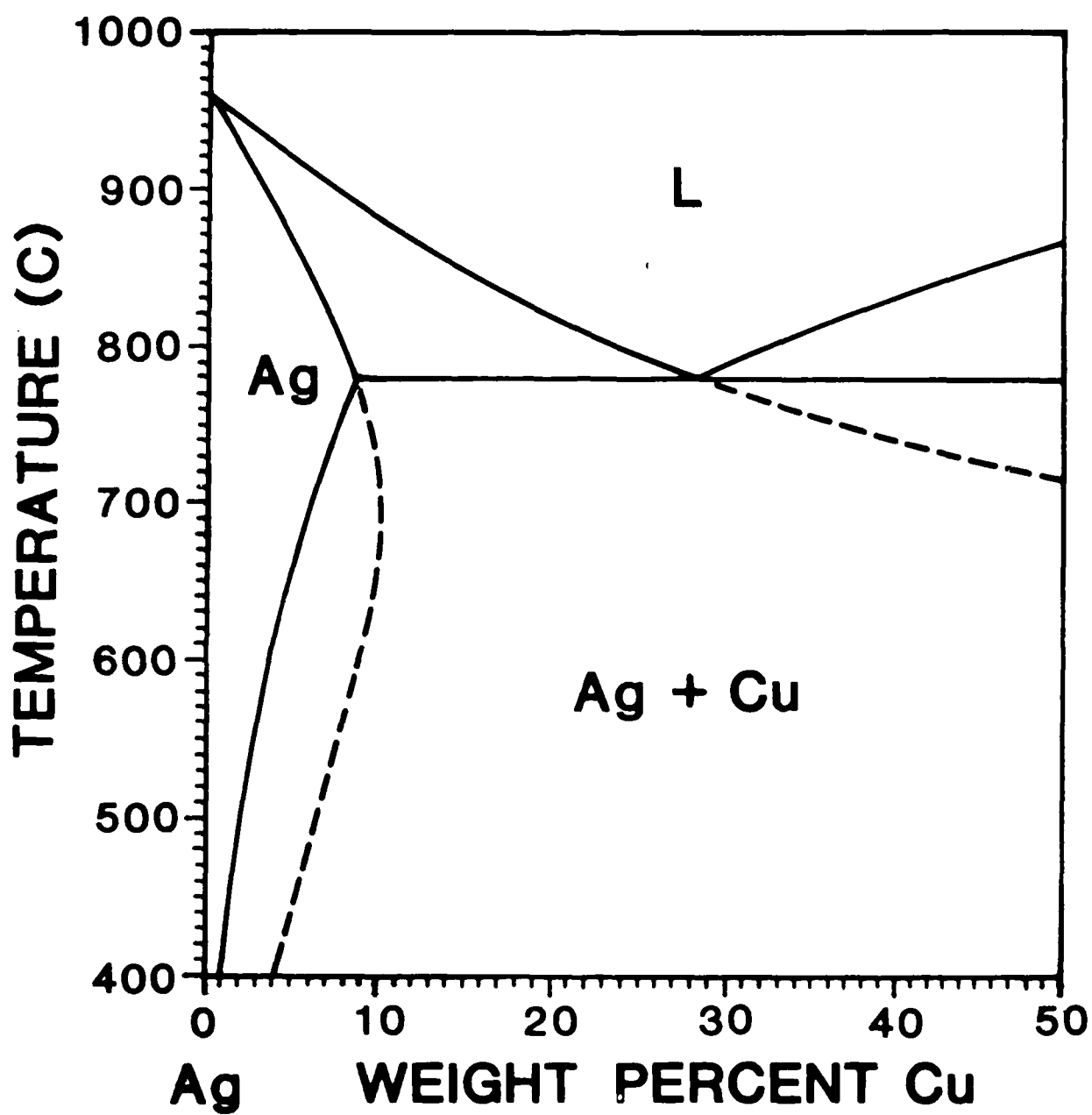
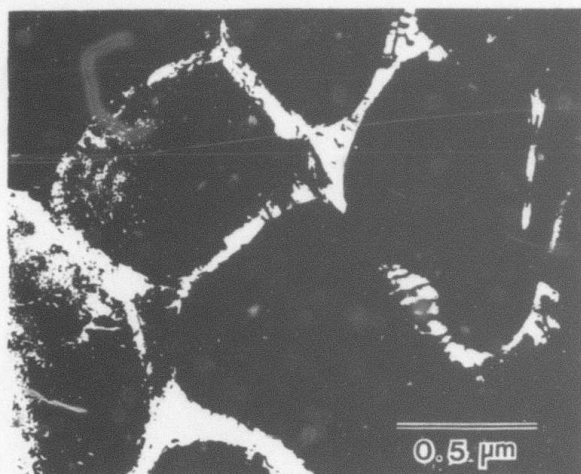
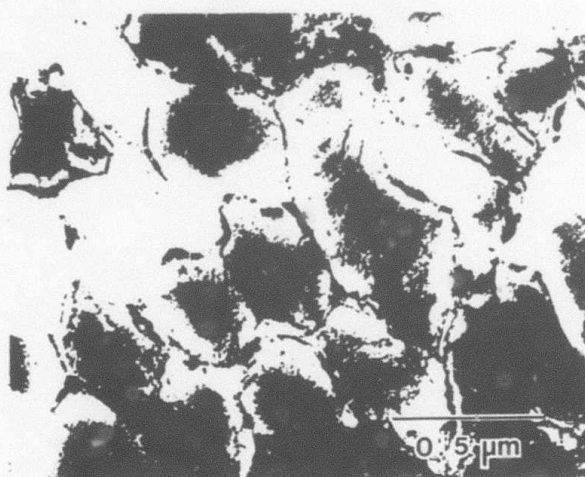


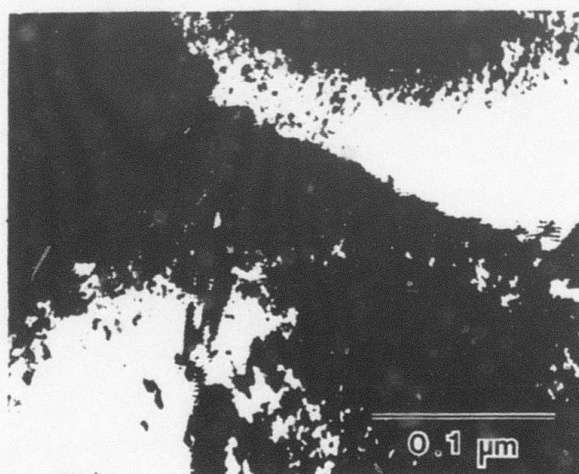
Fig. 1



a

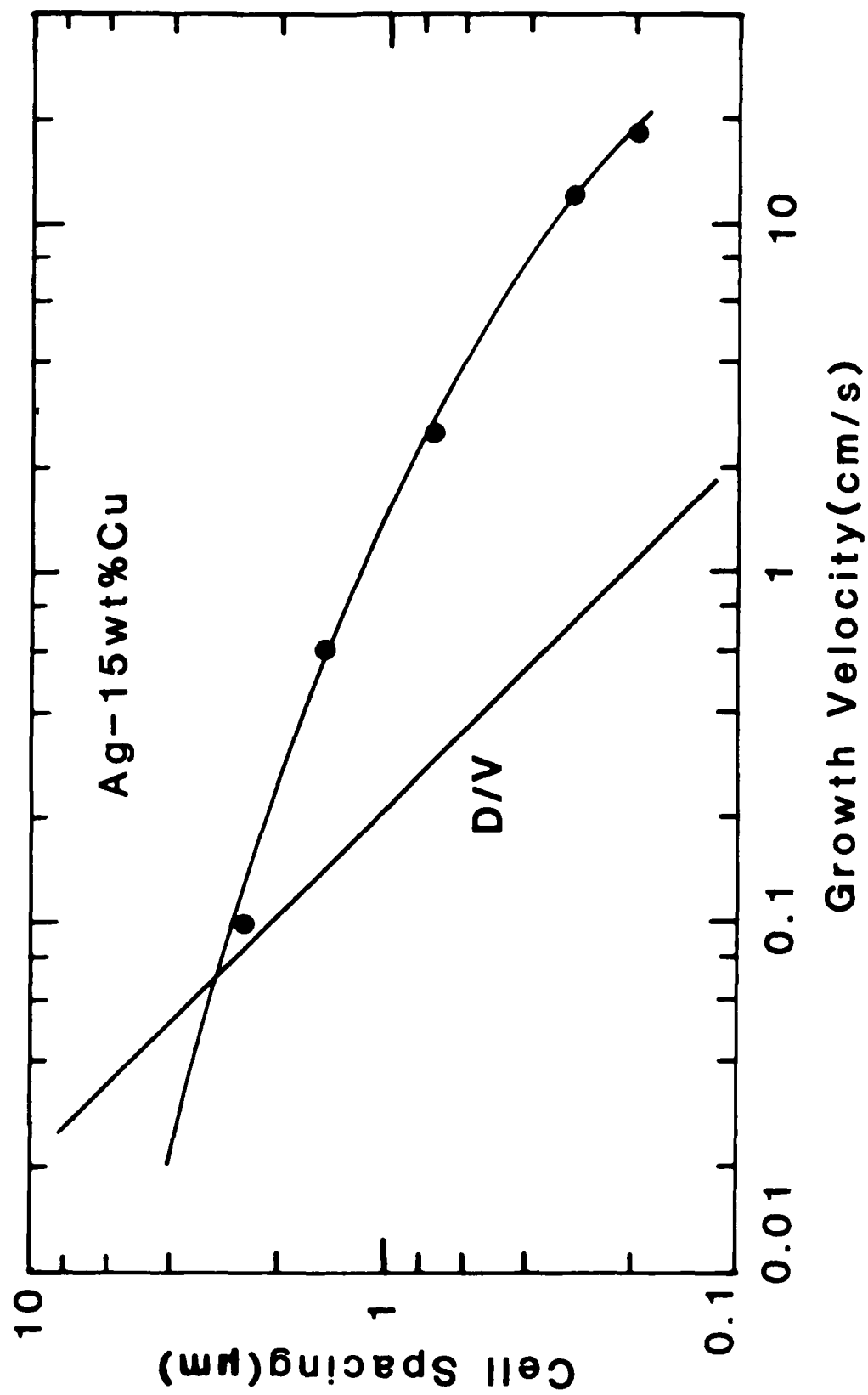


b



c

Fig 2



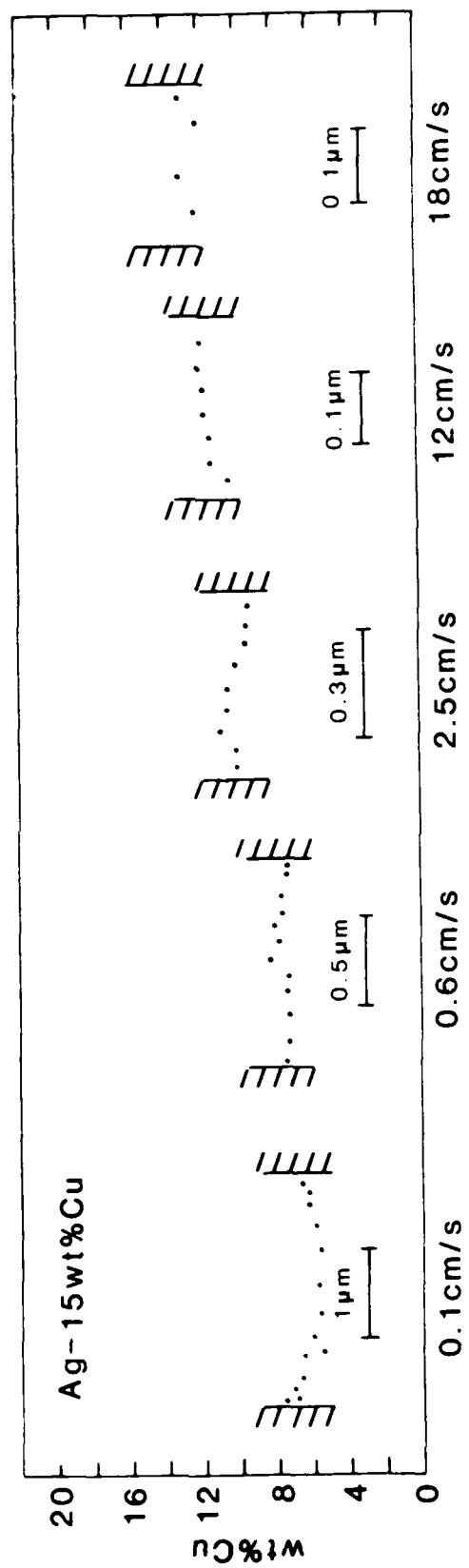


FIG 4

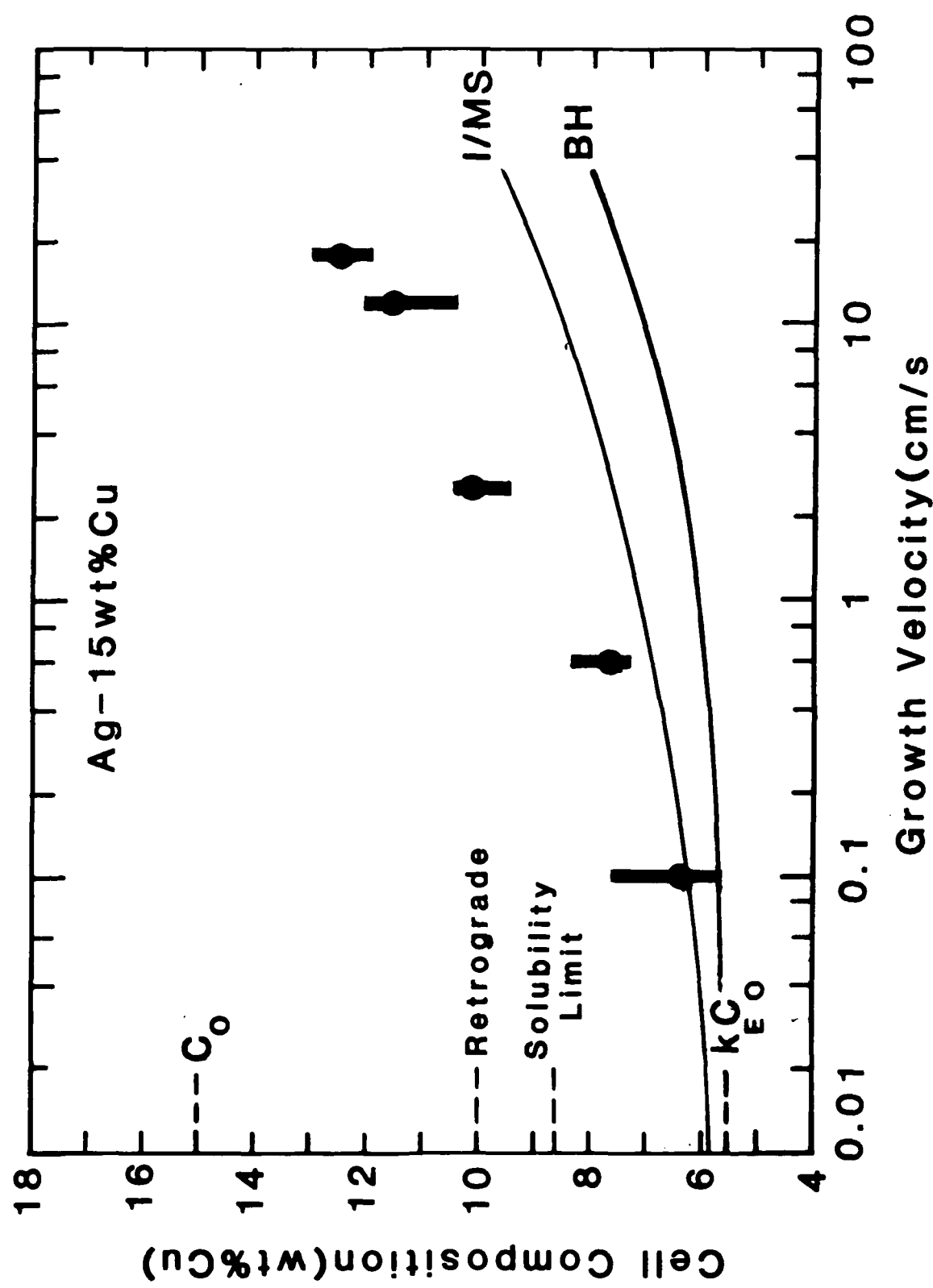


Fig. 5

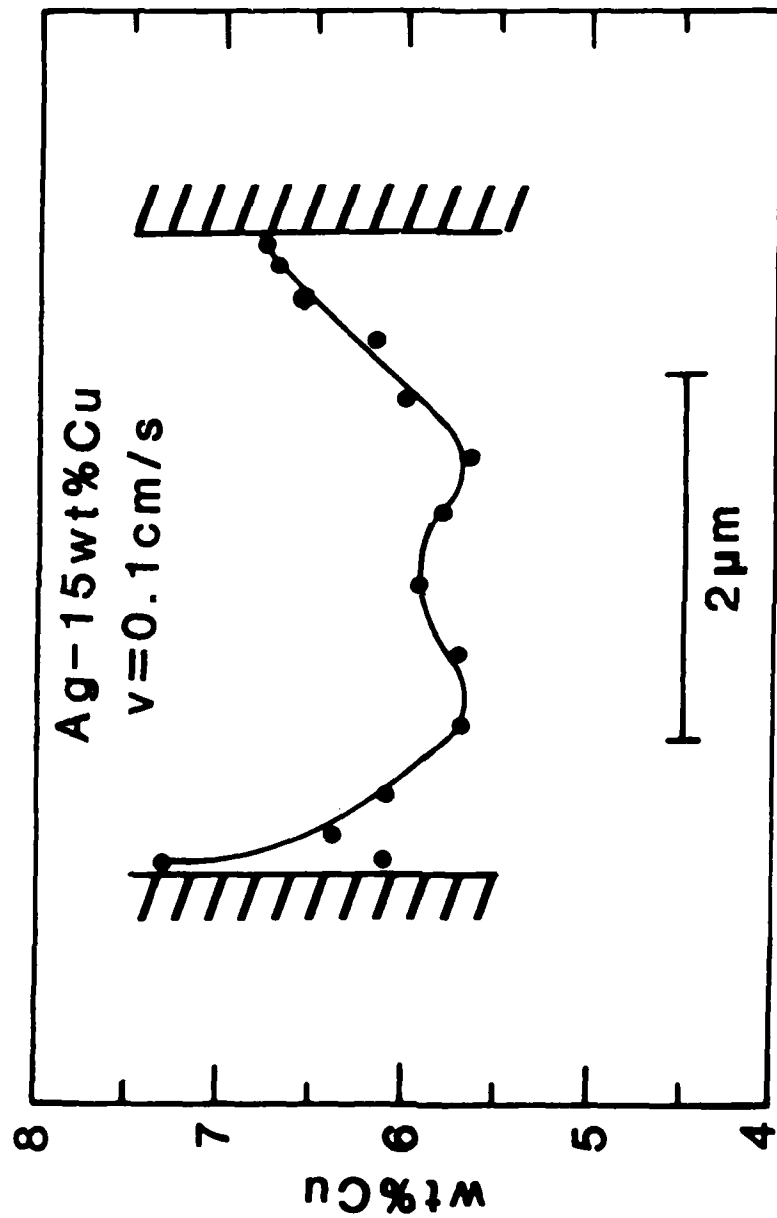


Fig 6

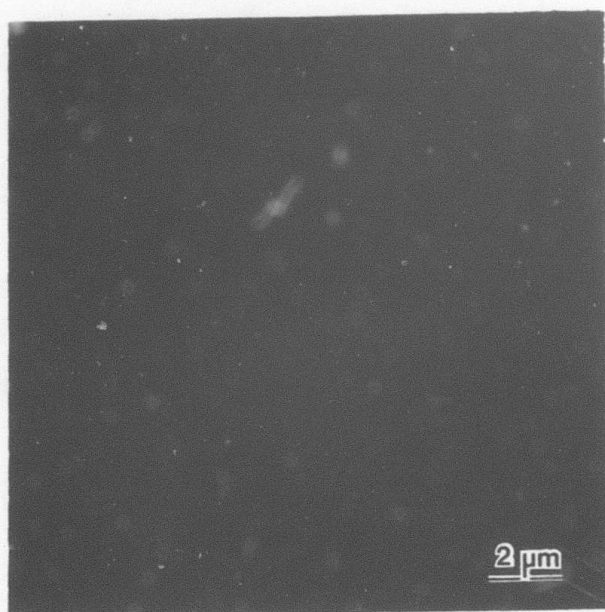


Fig. 7

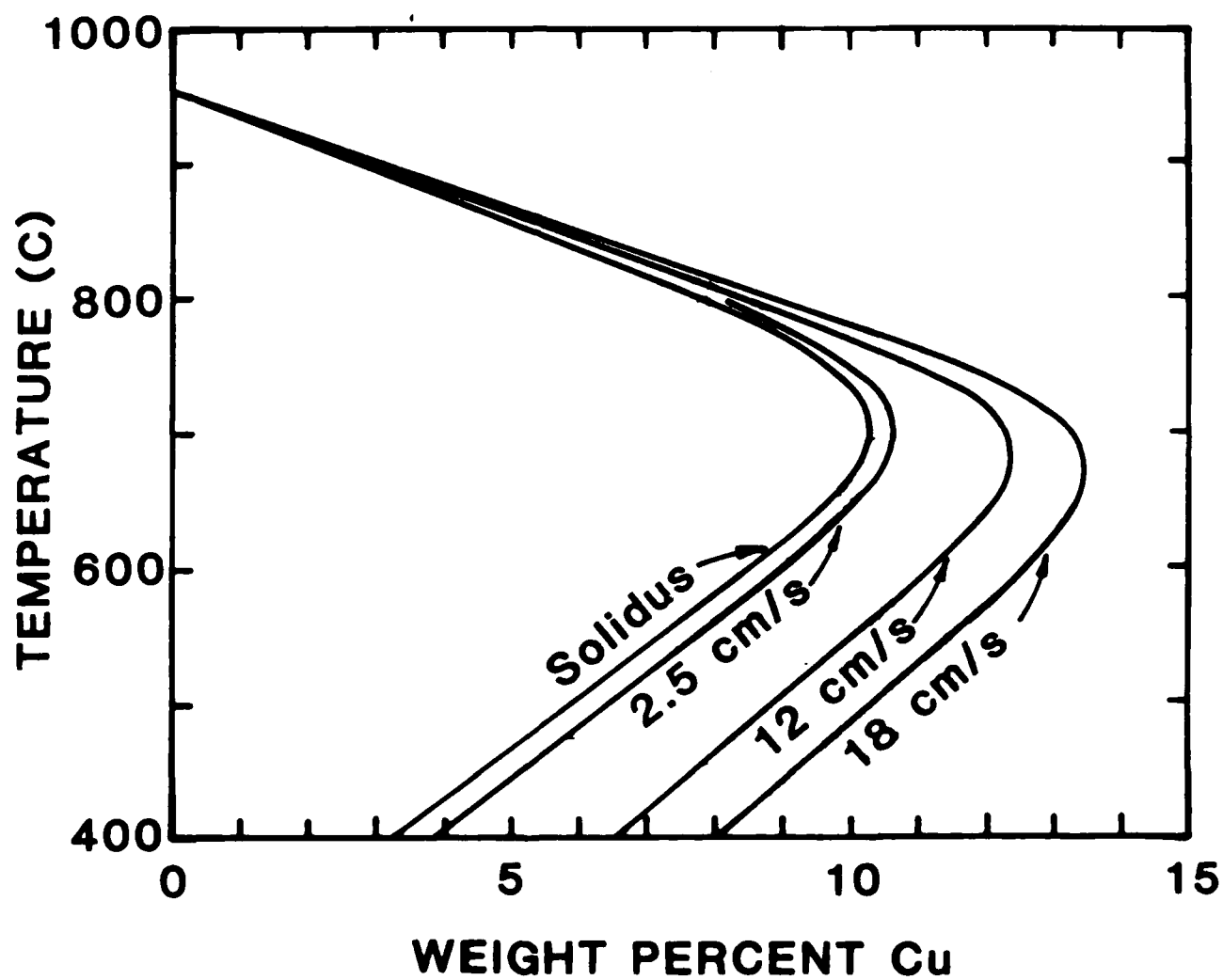


FIG. 8

# CRYSTALLIZATION OF THE ICOSAHEDRAL PHASE IN RAPIDLY QUENCHED AL-RICH AL-MN ALLOYS

A.J. McAlister,\* L.A. Bendersky,\* R.J. Schaefer,\* and F.S. Biancaniello\*

\*Institute for Materials Science and Engineering  
National Bureau of Standards, Gaithersburg, MD 20899

\*Center for Materials Research  
The Johns Hopkins University, Baltimore, MD 21218 and guest worker, NBS

## Introduction

Crystallization of the quasicrystalline icosahedral phase (1) formed in rapidly quenched Al-Mn alloys containing 22, 25, 26 and 27 wt % Mn has been studied by constant heating rate differential thermal analysis (DTA). Phases present in as-quenched (fcc + icosahedral) and crystallized (fcc + Al<sub>6</sub>Mn) alloys were determined by x-ray diffraction (XRD) and transmission electron microscopy (TEM). Heats and activation energies of transformation were estimated from the DTA results. The microstructure of a partially converted sample was examined by TEM.

## Experimental Procedure

Rapidly solidified Al-Mn alloys were prepared by melt spinning, using chunks of arc melted buttons prepared from 99.99% Al and 99.97% Mn. Stated compositions are starting compositions of the arc melted buttons, and are probably within a few tenths of a weight % of the composition of the final melt spun ribbons. Full details of preparation and characterization of the melt spun ribbons, and of the XRD and TEM methods, have been presented elsewhere (2).

For DTA studies the quenched ribbons were cut into short strips which were stacked in alumina crucibles. All DTA studies were carried out in a Mettler (TA) 2000C Thermoanalyzer<sup>#</sup>. In this instrument, temperatures are measured at the exterior of the flat crucible bases, with the reference crucible base temperature controlled. Pertinent experimental quantities must be extracted from the raw data by model analysis.

<sup>#</sup>Reference to commercial equipment is for identification only and in no way constitutes endorsement or evaluation of its merits.

### Analysis and Interpretation of DTA Data

The DTA data have been analyzed by means of the following dynamic model, a simple generalization of the Goldberg and Prosen (3) treatment:

$$h_R (T_f - T_R) = C_R \dot{T}_R$$

$$T_R = T_o + \alpha t$$

$$h_s (T_f - T_s) + h_{s'} (T_{s'} - T_s) = C_s \dot{T}_s$$

$$h_{s'} (T_s - T_{s'}) + \dot{q}_s = C_s \dot{T}_s$$

where  $T$  is temperature,  $t$  is time,  $\alpha$  is heating rate,  $C$  is heat capacity. Subscripts refer to:  $f$ , furnace wall;  $R$ , reference crucible;  $s$ , sample crucible;  $s'$ , sample;  $o$ , initial condition. The  $h$ 's are heat transfer coefficients:  $h_R$ , furnace to reference crucible;  $h_s$ , furnace to sample crucible;  $h_{s'}$ , sample crucible to sample. The quantity  $\dot{q}_s$  is the rate of heat flow into the sample due to phase transformation. All quantities are known, calculable without significant error, or obtainable from measurements of transformations of known enthalpy change.

Expressions for the heat of transformation,  $q = \int \dot{q}_s dt$  and for the sample temperature,  $T_{s'}$ , are easily derived from the model equations.  $T_{s'}$ , so calculated, at maximum deviation from base line (1.5 ° C or less), was used in constructing Kissinger plots (4) from which activation energies were obtained. This DTA data treatment method is not without flaw, but a variety of experience indicates that it is reliable to within stated error limits.

The slope of the Kissinger plot,  $\ln(\alpha/T_p^2)$  vs  $(1/T_p)$ , where  $T_p$  is the sample temperature  $T_{s'}$  in K at maximum deviation from baseline and  $\alpha$  the heating rate, is expected to yield the quantity  $E_a/n$  for transformations which can be described under isothermal conditions by the Johnson-Mehl-Avrami (JMA) equation (5):

$$1 - \zeta = \exp \{-Kt^n\}.$$

Here  $\zeta$  is the fraction transformed;  $K = K_o \exp\{-E_a/RT\}$  the temperature dependent rate constant for the dominant step of the transformation. The coefficient  $n$  has a value dependent on the mechanism of the dominant step. Typical values of  $n$  have been listed by Christian (6). The validity of the Kissinger relation has been established by Henderson (7) and Meisel and Cote (8), who have generalized the isothermal JMS expression to constant heating rate conditions, and have presented recipes for obtaining  $E_a/n$ ,  $E_a$ , and  $n$  from DTA data. For various reasons,  $E_a$  and  $n$  so obtained cannot be regarded as describing the transformation uniquely. Isothermal kinetic expressions more general than JMA have been derived (6) but not, to our knowledge, extended to constant heating rate conditions.

## Results and Discussion

Only the fcc and icosahedral phases could be detected in the as-quenched samples; only fcc and  $\text{Al}_5\text{Mn}$  immediately after transformation. Relative abundances of the different phases could not be accurately determined, but trends with composition were inferred. For the as-quenched alloys, the ratio of the intensities of the strongest XRD lines, fcc to icosahedral, drops from 4.5 at 22 wt % Mn to 1.8 at 27 wt % Mn. There is considerable scatter in the ratio for independent preparations at given composition, and there are indications of preferred orientation texture in the fcc. However, the trend was clearly discernible (2). Metallographic examination, while not quantitative, clearly shows the presence of significant amounts of fcc at all four concentrations. After transformation, DTA melting studies were carried out. From the observed heat of the fcc melt and the model enthalpies of Murray (9), the fcc abundances at the onset of melting were estimated to be .11, .02, .002, and zero, from 22 to 27 wt % Mn. The 26 and 27 wt % Mn samples underwent a further transformation between crystallization and melting, in which a small fraction of ' $\text{Al}_5\text{Mn}$ ' (hexagonal,  $a=12.4\text{\AA}$ ,  $c=28.4\text{\AA}$ ) was produced. From these trends, it is clear that not only is the icosahedral phase transformed during the transformation, but the fcc phase is consumed as well. The microstructure of a partially transformed 25 wt % Mn sample, shown in Fig. 1, supports this view.

At each composition, a number of heats were carried out at rates in the range of 1.5 to 20.0 °C/min. Smooth Kissinger plots were obtained. For each heat, the heat of transformation was calculated. In contrast to the smoothness of the Kissinger plot, the heat of transformation generally showed scatter, the distribution being markedly skewed toward higher magnitude. For example, we found the heat of transformation to range from -.30 to -.40 kcal/mol of atoms at 22 wt % Mn, and from -.45 to -.49 at 25 wt % Mn. Possibly, this scatter arises from variation in phase abundance along the length of the quenched ribbon. No indication of rate dependence was seen. The heats of transformation listed in Table 1 are not means of all values at each composition, but have been placed where the values cluster. The stated uncertainties are based on calibration studies of equilibrium and metastable transformations and analysis of the uncertainties in the quantities entering the dynamic DTA model. They exceed the experimental scatter. Also listed in Table 1 are  $E_a/n$  and intercept from the Kissinger plots. The uncertainties given for the latter quantities are the standard statistical uncertainties of the linear regression procedure.

TABLE 1  
Thermal and Kinetic Results

Concentration		Heat of Transformation kcal/mol of atoms	$E_a/n$ kcal	Kissinger Intercept $\ln(10^{-3}/K\text{-sec})$
wt% Mn	at% Mn			
22	12.2	-0.40 ± .08	167 $\pm$ 5 <sub>m</sub> 37.4 ± 1.4	12.4 ± 1.0
25	14.1	-0.48 ± .10	20 $\pm$ 1 <sub>m</sub> 36.9 ± 0.7	11.4 ± 0.5
26	14.7	- .46 ± .92	37.6 ± 1.2	12.5 ± 0.9
27	15.4	- .29 ± .06	38.4 ± 1.8	12.0 ± 1.2

The heat of transformation varies with Mn content, showing an extreme value of  $-0.48 \pm 0.10$  kcal/mol of atoms near the composition  $\text{Al}_6\text{Mn}$ . This value is in good agreement with that reported by Kelton and Wu (10) of  $-0.5$  kcal/mol of atoms for a rapidly quenched sample containing 24.9 wt % Mn.

For the composition 25 wt% Mn, an attempt was made to ascertain  $E_a$  directly by plotting  $\ln \ln \left( \frac{1}{1-\xi} \right)$  vs  $1/T_s$ , under the assumption  $\dot{\xi} = (T_s - T_b) / \int (T_s - T_b) dt$ , where  $T_b$  is the background sample temperature level (7,8). A rough value of  $E_a = 92$  kcal was obtained. Hence a value  $n = 2.5$  is indicated. Literal interpretation of this result within the framework of the JMA approximation suggests long range diffusion controlled growth, all shapes growing from small dimensions, with constant nucleation rate (6). The general danger of such literal interpretation has already been noted, and additional caution is urged in the present case, owing to: (a) weak thermal signals resulting from the low heat of transformation and necessarily small sample mass; (b) the noise level of the instrument; (c) the difficulty in assigning start and stop values of  $\xi$ ; and (d) difficulty in approximating  $T_b$  because of the quite discernible change in sample specific heat during transformation.

However, TEM investigation of the microstructure of a partially transformed 25 wt % Mn sample lends credence to diffusion controlled growth of the  $\text{Al}_6\text{Mn}$  phase. In any small piece of partially transformed ribbon, one finds areas in which the icosahedral grains are completely transformed, others where partial transformation has occurred, and yet others where no transformation has occurred. Nucleation of  $\text{Al}_6\text{Mn}$  seems usually to start at the fcc/icosahedral interface, with growth into both the icosahedral and interdendritic fcc phases. This latter point is illustrated in Fig. 1, which shows a micrograph of a partially transformed area. The inhomogeneity of  $\text{Al}_6\text{Mn}$  nucleation in the ribbon probably arises from the solidification sequence during rapid quenching, the first stage of which is nucleation of the icosahedral phase, followed by growth of the randomly oriented crystallites to a diameter of a few micrometers. In the second stage, the fcc phase is nucleated on various icosahedral crystallites, and grows with a definite orientational relation to the crystallite upon which it nucleated. Thus, at completion of solidification, there will exist fcc/icosahedral interfaces both with and without orientational relation between the two phases, the latter type being more favorable to nucleation of  $\text{Al}_6\text{Mn}$ . This, coupled with the small size and high spatial density of icosahedral crystallites could well lead to apparently constant  $\text{Al}_6\text{Mn}$  nucleation rate during a substantial fraction of the time required for complete transformation under constant heating rate conditions. Overall, the morphology of the  $\text{Al}_6\text{Mn}$  crystallites is compatible with diffusion controlled growth.

#### Summary

Crystallization of the quasicrystalline icosahedral phase formed in Al-rich Al-Mn alloys has been studied by constant heating rate DTA, XRD, and TEM. Heats and activation energies of transformation were obtained, and evidence presented which suggests that the transformation is diffusion controlled.

#### References

1. D. Schechtman, I. Blech, D. Gratias, and J.W. Cahn, Phys. Rev. Lett., 1984, Vol. 53, p 1951.
2. R.J. Schaefer, L.A. Bendersky, D. Schechtman, W.J. Boettinger, and F.S. Biancaniello, Met. Trans. A, to be published.
3. R.N. Goldberg and E.J. Prosen, Thermochimica Acta, 1973, Vol. 6, p 1.
4. H.E. Kissinger, Analytical Chemistry, 1957, Vol. 29, p 1702.
5. W.A. Johnson and R.F. Mehl, Trans. Am. Inst. Min. (Metall.) Engrs., 1939, p 416; M. Avrami, J. Chem. Phys., 1973, Vol. 7, 1103, 1940, Vol. 8, p 212, and 1941, Vol. 9, p 177.

6. J.W. Christian, The Theory of Transformation in Metals and Alloys (Pergamon Press, Oxford, 1975).
7. D.W. Henderson, J. Thermal Analysis, 1979, Vol. 15, p 325.
8. L.V. Meisel and P.J. Cote, Acta Met., 1983, Vol. 31, p 1053.
9. J.L. Murray, A.J. McAlister, R.T. Schaefer, F.S. Biancaniello, and D.L. Moffat, to be published.
10. K.F. Kelton and T.W. Wu, Applied Physics Letters, in press.

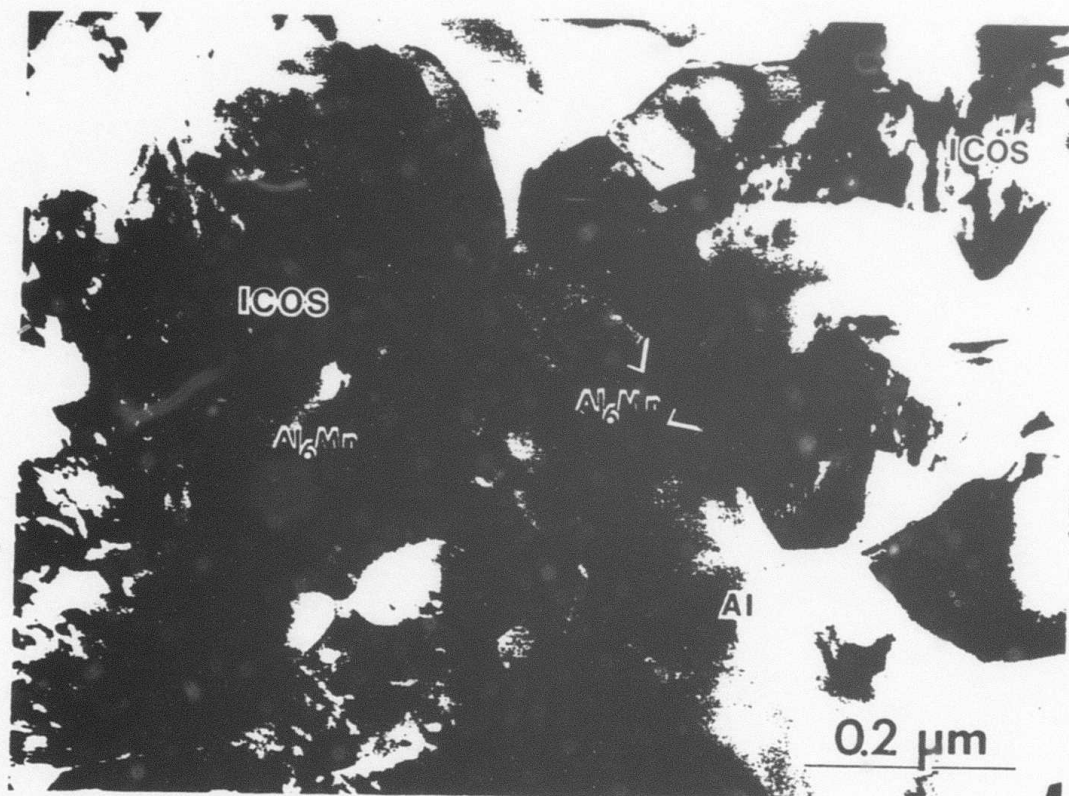


Fig. 1

TEM micrograph of a partially transformed specimen, fcc + icosahedral + fcc + icosahedral +  $\text{Al}_6\text{Mn}$ . Icosahedral phase can be recognized from the typical mottled contrast. Orthorhombic  $\text{Al}_6\text{Mn}$  appears on fcc/icosahedral interfaces.

X-Ray and Electron Metallographic Study  
of Quasicrystalline Al-Mn-Si Alloys

J.L. Robertson, M.E. Misenheimer and S.C. Moss

Department of Physics  
University of Houston-University Park  
Houston, TX 77004

and

L. Bendersky

Center for Materials Research  
The Johns Hopkins University  
Baltimore, MD 21218 and  
National Bureau of Standards  
Gaithersburg, MD 20899

ABSTRACT

We present the results of x-ray diffraction, scanning electron microscopy (SEM) and transmission electron microscopy (TEM) on spin-quenched flakes of alloys of composition  $\text{Al}_{94-x}\text{Mn}_x\text{Si}_{0.06}$  ( $x=0.20, 0.22, 0.24$ ). From x-ray pinhole photographs of intact flakes we conclude that the alloys are nearly pure single phase and may be indexed using the prescription of Cahn, Shechtman and Gratias as a guide. The grain size is estimated to be between 13 and 18  $\mu\text{m}$ . From high resolution diffractometer tracings a correlation range of 350-480Å is recorded with an asymmetric profile at the position of the 2-fold peak ( $Q \approx 3.04\text{\AA}^{-1}$ ) whose extent in  $Q$  is comparable to the inverse correlation range. These short correlation ranges are associated with defects as in a defective Penrose tiling. SEM photos on a fractured flake show a chill zone of 3-4  $\mu\text{m}$  followed by columnar dendritic morphology. The extent of a single dendrite cluster is about the same as the x-ray grain size. At the bottom of the chilled surface distinct geometrical shapes are observed including an occasional pentagonal dodecahedron of about 0.4-0.6  $\mu\text{m}$  in size. TEM micrographs show a cellular structure on the order of 40-100nm, both near the chill zone and in a dendrite arm, and distinct mottling or speckling on a scale of 2-5nm.

## 1. Introduction

The finding by Shechtman et al<sup>1</sup> of a metallic alloy which shows both icosahedral symmetry and sharp diffraction peaks has proven to be a remarkable discovery. Closely following the experimental announcement was a letter by Levine and Steinhardt<sup>2</sup> in which a theoretical framework for such quasicrystalline structures was outlined. As noted by Levine and Steinhardt<sup>2</sup>, Penrose<sup>3</sup> had shown some years earlier how to tile completely a two-dimensional (2-D) surface with elements that preserved pentagonal orientational order while necessarily sacrificing periodicity. The Penrose scheme was elaborated upon by Gardner,<sup>4</sup> Mackay<sup>5</sup> and Penrose himself<sup>6</sup> and it was Mackay<sup>5</sup> who first suggested the application of these modeling schemes to real three-dimensional (3-D) solids. Penrose has also noted<sup>7</sup> that in building his aperiodic tilings from two basic rhombi, even while carefully obeying local matching rules to insure that a large tiled surface will be filled, one invariably runs into trouble as the tiled surface grows outward from the chosen nucleus. By "trouble" we mean that sites eventually crop up at which the local rules cannot be satisfied. These defects can, however, be incorporated in the 2-D surface and the tiling can proceed without loss of orientational order, i.e. the orientation of an element outside the defect is the same as inside.<sup>8</sup>

We mention this aspect of quasicrystalline order at the outset because we believe (with others) that all crystals grow via local rules. In the case of the melt-spun quasicrystalline alloys, however, local rules do not build a succession of repeating cells, whatever the local molecular or icosahedral configuration in the melt may be.<sup>9</sup> Defects seem thereby to be considerably more a concomitant of the growth of quasicrystals than of crystals (where they aid growth), and it will be partly the purpose of this paper to bring both our own observations and those of others to bear on this question.

Theoretically, one can construct an infinite quasicrystal through the use of projection crystallography in which a higher dimensional space (e.g.  $Z^6$ ) is employed. The dimensionality is given by the number of independent orthogonal axes, or independent wave vectors<sup>10</sup>, required by the structure in question. For example, as Zia and Dallas<sup>11</sup> and Elser<sup>12</sup> show, a one-dimensional (1-D) aperiodic sequence can be constructed from a 2-D square (X-Y) lattice by projection of all points within a given band onto a line, the tangent of whose angle with the X-axis is irrational. Both the sequence and its Fourier transform can thus be generated which provides a straightforward analytical method for calculating the scattered x-ray intensities. Elser<sup>12</sup> and Cahn et al<sup>13</sup> have independently applied this cut and projection method to 3-D quasicrystals and have indexed the observable peaks in the electron<sup>1</sup> and x-ray<sup>14</sup> diffraction patterns and provided an estimate of their intensities. Kuriyama and Long<sup>15</sup> have developed an alternative scheme for analyzing these patterns which gives an equivalent indexing of the lines and some insight into actual atomic positions. However, an unambiguous assignment of atoms to sites remains to be done. The influence of defects remains a problem as well in spite of the perfection of an infinite quasicrystal that may be obtained by projection from the  $Z^6$  space.

The available quasicrystalline material is obtained through quenching or vapor deposition as a metastable product intermediate between the glass, in which icosahedral order may prevail<sup>9</sup>, and the crystalline phase(s) which are usually quite complex and thus slow-growing; the microstructure is therefore fine-grained. Electron diffraction can explore the structure within a single grain as in Ref. 1 and subsequent work<sup>16-20</sup>. In particular Bursill and Lin<sup>16</sup>, Hiraga et al<sup>17</sup> and Portier et al<sup>18</sup> show very high resolution electron micrographs of the structure of an  $Al_6Mn$  alloy projected along high symmetry axes. The image of Hiraga et al<sup>17</sup> down a 5-fold axis extends over an area of

$\sim 350 \times 250 \text{ \AA}^2$  and reveals striking detail not only on the 5-fold orientational order and the Fibonacci-like sequence of projected potential but also on the nature of the defects alluded to earlier. This work and the recent work of Tanaka et al<sup>20</sup> provide important clues to our understanding of the structure and defect content of these materials.

Unfortunately, however, transmission electron diffraction and microscopy are of limited use in a quantitative structural study because the diffracted dynamical intensities must be treated within an n-beam multiple scattering formalism and are thereby not immediately useful for evaluating structure factors.<sup>21</sup> X-ray or neutron scattering on bulk samples must be employed, but these patterns are complicated by the powder averaging over the quasicrystalline reciprocal lattice. The study of Bancel et al<sup>14</sup> represents the first serious attempt to analyse such a powder pattern from quenched Al<sub>6</sub>Mn. Their (preliminary) indexing scheme has since been shown to be incorrect<sup>12,13</sup> and their pattern had quite intense Al reflections, indicating a large volume fraction of Al rejected during the growth of the quasicrystal phase. An interesting finding, however, was their measurement of very broad powder lines indicating a mean correlation range of  $\sim 300 \text{ \AA}$ . This is nominally at variance with dendrite arms of  $\sim 1 \mu\text{m}$  in the electron microscopic images, as Bancel et al<sup>14</sup> note, and should be attributable to defects because a perfect quasicrystal will have  $\delta$ -function peaks.

In the present paper we present observations on the quasicrystalline microstructure of a series of three spin-quenched alloy ribbons of composition Al<sub>0.74</sub> Mn<sub>0.20</sub> Si<sub>0.06</sub>, Al<sub>0.72</sub> Mn<sub>0.22</sub> Si<sub>0.06</sub> and Al<sub>0.70</sub> Mn<sub>0.24</sub> Si<sub>0.06</sub>. These three alloys fall within a domain previously found<sup>22</sup> to be considerably more stable on heating and to consist of nearly pure quasicrystalline material. We have used x-ray scattering, scanning electron microscopy (SEM) and transmission electron microscopy (TEM) to measure structure on scales from tens of angstroms (nanometers)

to tens of microns. It is our purpose to elucidate the various length scales (sizes) of macro- and microstructures that appear and to correlate results obtained by different methods thereby providing insight not only on the structure itself but also on the way it grows.

## 2. X-Ray Scattering

As noted above, our experiments are on the three alloys of  $Al_{.94-x} Mn_x Si_{.06}$  where  $x$  is .20, .22, and .24. All were prepared by R.F. Schaefer of the NBS by melt spinning which resulted in brittle ribbons which broke into flakes on the order of 2mm x 2-4mm x .035mm. For  $x = .20$  and .22, the as-quenched flakes were annealed at 450°C for one hour. For  $x = .24$  they were examined as-quenched. Both x-ray photography and diffractometry were done on intact flakes of the alloys. Our overall aims were the following:

- 1) to use photographic methods both to record a large number of diffraction peaks to compare with theoretical predictions and to examine single quasicrystal grains;
- 2) to measure texture in the quenched ribbons;
- 3) to determine grain size in these ribbons;
- 4) to measure carefully the profiles of the strong lines using moderately high resolution diffraction.

### a. Transmission Pinhole Photograph

The x-ray diffraction photography proved particularly useful. Fig. 1 shows a 39 hour transmission pinhole photograph taken with the incident beam normal to a flake of  $x = 0.24$ . The source was a RU-200 rotating anode supply with point focus geometry and a Mo target operated at 40kV and 150ma. The incident collimation produced a beam of ~ 0.75mm diameter on the sample with a divergence of  $1.0^\circ$  and a sample-film distance of 72.5mm. A total of 19 lines could be observed on the original film but only 16 survived reproduction and these are labeled in Fig. 1(a). Although a .003 inch Zr filter was used to remove  $MoK_\beta$ , radial white streaking associated with the strong spots around a Debye ring is

still visible. Photographs taken with a conventional sealed-tube GE XRDV unit and identical collimation produced quite comparable pictures from  $x = .20$  and  $.22$  but they showed fewer lines and required considerably longer exposure. Several aspects of this film are noteworthy:

1) Some of the Debye rings are distinctly spotty, while some are less so and still others appear continuous.

2) Because the flake is so thin and  $\text{MoK}\alpha$  is used ( $\mu t \approx .09$ ) both front and back diffract equally.

3) The intensity is uniformly distributed about the rings, i.e. there is no texture about a normal to the flake.

4) There is only one intense ring attributable to Al at the (111) position (see Table I), and its intensity is  $\sim 1/20 - 1/50$  of the strongest icosahedral phase lines. The Al (220) is barely visible.

5) The pattern is quite weak. If one were to take a similar photo of a fine-grained Al foil of comparable thickness, the exposure would be on the order of several hours, or an order of magnitude less than required here. This is because the diffraction pattern of a quasicrystal fills all reciprocal space with peaks of varying strength. A crystal directs the same kinematic intensity into a small number of strong lines when the unit cell is small.

We have indexed the pattern in Fig. 1 following the scheme of Cahn et al<sup>13</sup> who have chosen an orthogonal set of six 5-fold axes in  $Z^6$  which are composed of two groups related in a cyclical fashion about a 3-fold axis. Alternatively, an indexing in  $R^3$  may follow the  $\bar{m}35$  point group description of Miller indices<sup>23</sup> in which a six index notation is used in conjunction with an orthogonal set of three 2-fold axes. In this indexing  $hkl$  and  $h'k'l'$  refer to units of one and  $\tau$  (the golden ratio = 1.618034), respectively.

The indexing scheme of Elser<sup>12</sup>, in which the index numbers  $n_i$  ( $i=1,6$ ) are along the orthogonal axes in  $Z^6$ , uses the six 5-fold axes in  $R^3$  related cyclically about the one that is acute to all the others. Bak<sup>10</sup> has also suggested such a choice of wavevectors. The methods of Elser<sup>12</sup> and Cahn et al<sup>13</sup> are basically equivalent and give the same diffraction peaks; but the calculations must be carried out to enough hierarchies of intensity to account for the experimental observations. One cannot, however, be too arbitrary in picking a very weak member of the (infinite) set of peaks in order to fit a stray candidate. The calculations can only estimate intensity through the separation of a point in the higher dimensional reciprocal space from the cut plane used in the cut and projection method. The identity of the atoms is not included (the cell is primitive in  $Z^6$ ) and it is therefore remarkable that there can be rough agreement between calculation and experiment. In the neutron pattern<sup>24</sup>, for example, the array of weak and strong peaks is very different from the x-ray case. Because the neutron scattering length for Mn is negative, this difference between neutron and x-ray intensities is clear evidence both for ordering and for a more complex basis set than is considered by theory<sup>12,13</sup>.

The indexing of the peaks along with estimates of their intensities is presented in Table I. The estimation of  $Q$  ( $= 4\pi\sin\theta/\lambda$ ) from the film is done using the Al (111) line as a marker and then refining. Film shrinkage, even if uniform, produces a shift in  $Q$  which increases with increasing ring diameter and our estimate of  $Q$  is thus not very accurate. Still, the fit is quite acceptable and only the (111) and very weak (220) lines of Al are visible. All other lines can be indexed using the lowest hierarchy of predicted quasicrystal intensities. The material is therefore essentially single phase. The index  $N$  in Table I is a convenient notation from Cahn et al<sup>13</sup> referring to the integer part of  $Q^2$  (as opposed to its  $\tau$ -component), and it is numerically equal to twice the sum of the squares of the given indices in  $Z^6$ .  $N$  therefore takes on only even values as  $Q$

increases. Following Cahn et al<sup>13</sup>,  $Q_6^2$  (the square of the length of a 6-dimensional vector,  $Q_6$ , in  $Z^6$ ) may be given in dimensionless units as  $Q_6^2 = N(2 + \tau)$ .  $N$  therefore is a direct index of the length in  $Q_6$  space and thus in the real experimental  $Q$  space.

The intensity estimates in Table I are left in units of  $1/Q_C$ , where  $Q_C$  is the distance of a point from the cut plane<sup>13</sup>, because our intensity comparison, using Fig. 1, is not particularly reliable. As we shall see, the spotty rings imply a large grain size and we are thus somewhere between a single quasicrystal and an ideal poly-quasicrystal. We therefore leave accurate intensity estimates to more complete neutron and synchrotron powder data, although our own powdered sample results agree quite well with the intensities from the intact flake. The qualitative comparison in Table I is reasonable in that peaks expected to be strong are indeed strong especially if we include multiplicity factors.

The spotty Debye rings, shown more clearly in Fig. 1(b), are of particular interest because they are evidence of single quasicrystal grains and suggest the possibility of high resolution x-ray microtopography on a single one of these. In a polycrystalline sample of grain size  $> 1\text{-}2\mu\text{m}$ , photographic methods have traditionally been employed to estimate the grain size.<sup>25</sup> It is a useful quantity referring to the size of a singly oriented grain of the aggregate, whatever its defect content or external morphology may be. It is straightforward to show that the number of spots,  $M$ , on a Debye ring is given by<sup>25</sup>

$$M = \frac{1}{2}up\cos\theta d\theta \quad (1)$$

where  $u$  is the number of crystals or grains in the x-ray beam and  $p$  is the multiplicity of the reflection in question (which in our case is the number of members in all sets in  $Z^6$  with the same  $N$ );  $p=12$  for a 5-fold axis, 20 for a 3-fold axis, 30 for a 2-fold axis, and 60 for a mirror plane;  $p = 120$  is the general case.  $\theta$  is twice the Bragg angle, and  $d\theta$  is effectively the divergence angle of the

x-ray beam. The mean volume  $v$  of a single grain will be  $V/u$ , where  $V$  is the irradiated volume, so that:

$$v = \frac{V}{u} = \frac{Vp \cos \theta}{2M} d\theta \quad (2)$$

A careful counting of the spots in the  $N=18$  ring (no. 5 in Fig. 1(a)) at  $Q = 2.89 \text{ \AA}^{-1}$  yields a value of  $M = 250 \pm 10$  for all three compositions. Using  $p = 12$ ,  $d\theta = 1^\circ$  and  $V = \frac{\pi D^2 t}{4}$ , with  $D = .75 \text{ mm}$  and  $t = .035 \text{ mm}$ , we obtain  $v = 5970 \text{ \AA}^3$ . Thus, if the grain is a cube, it is about  $18 \text{ \AA}$  on edge. In as much as the flake is only  $35 \text{ \AA}$  thick this means an average of only a couple of grains per thickness. From the enlargement in Fig. 1(b) it is clear that many of the spots are elongated radially. This requires that the overall grain shape be elongated normal to the flake, or somewhat columnar. We may assume for these elongated grains that they extend completely from front to back but are randomly oriented with respect to the ribbon surface. In this case the grain length is  $\sim 35 \text{ \AA}$  with a concomitant cross-sectional area of  $171 \text{ \AA}^2$  or an average extent on the flat ribbon face of  $13 \text{ \AA}$ .

Note that the  $N = 18$  peak has a multiplicity of 12 and reveals the individual spots clearly.  $N = 20$  is a 2-fold axis with  $p = 30$  and shows a denser array of spots.  $N = 38$  with  $p = 60$  is a more nearly continuous ring, while  $N = 52$  has  $p = 30$  and again is spotty. In other words, the spottiness of the Debye rings provides a further corroboration of the indexing scheme through the dependence on  $p$ . This spottiness, however, prevents us from accurately assessing the intensity. On the one hand, we should compare individual spot intensities from ring to ring without a multiplicity factor, as in a single crystal. But for continuous rings a multiplicity factor is, of course, necessary.

We note also that the x-ray rings, particularly for the peak associated with the 5-fold axis at  $N = 18$ , demonstrate a weak continuous background ring under the isolated spots. This we associate with a small fraction of fine-grained material, of about  $3\text{--}4 \text{ \AA}$  in thickness, formed as a chill zone against the cold

wheel. If these grains, as we shall see from SEM and TEM, are  $\sim .4\mu\text{m}$  in size, the number of spots from Eq. (1) is  $\sim 10^5$  and the ring appears continuous.

#### b. Diffractometer Scans

In Figs. 2(a) and 2(b) we show diffractometer data from a sample of  $x = .22$  using a  $\text{CuK}\alpha_1$  beam off a bent and ground Ge (111) monochromator. The sample was an intact flake of dimensions similar to that used in Fig. 1 and it was mechanically oriented for both symmetrical reflection and transmission. A sealed x-ray tube was used at 40 kV and 40 ma and intensity was sacrificed for resolution where the instrumental width was on the order of  $\Delta Q \approx .007\text{\AA}^{-1}$  at Si (400) and no  $\text{CuK}\alpha_2$  was observed. The beam was focused approximately onto the sample and was confined by slits. While  $\text{CuK}\alpha$  is not ideal in these samples (it fluoresces Mn) it was used both for resolution and for the fact that it is absorbed more than  $\text{MoK}\alpha$  and the sample is thus more nearly of ideal thickness for transmission ( $\mu t = 2.08$  versus 1.0 for ideal).

The intensity was nonetheless extremely weak and the scans in Figs. 2(a) and 2(b) required long times, at 0.5 cps, to accumulate  $\sim 500$  counts at the peaks. These two peaks are the  $N = 18$  and  $N = 20$  of Table I which are the 5-fold and 2-fold axes respectively at  $Q = 2.89\text{\AA}^{-1}$  and  $Q = 3.04\text{\AA}^{-1}$ . They are the strongest peaks in the pattern and are the ones indexed by Bancel et al<sup>14</sup> as 100000 and 110000. It is clear here as in Fig. 1 that the Al content is quite low as there is no evidence for an Al (200) reflection at  $Q \sim 3.10\text{\AA}^{-1}$  whereas in Bancel et al<sup>14</sup> it is about as intense as the quasicrystal peak at  $Q \approx 3.04\text{\AA}^{-1}$ . Most apparent in Fig. 2 is the absence of texture because the ratio of intensities,  $I(N=20)/I(N=18)$  is essentially the same in reflection and transmission.

The spottiness of the rings enters here as well and we must be careful not to assign too much significance to the value of  $I(N=20)/I(N=18)$ . It may be due in part to the increased multiplicity at  $N=20$  which fills in the Debye ring more densely. The diffractometer trace cuts through the rings in Fig. 1 with a narrow detector slit so that we examine only those grains oriented to diffract

into this slit. Within the irradiated volume used here there are only a total of 250-300 grains and our statistics are not terribly good. For good powder statistics one should examine more grains by spinning the sample or using MoK $\alpha$  and a larger sample, but then one loses the opportunity to measure grain size as in Fig. 1 and to assess texture. Pulverizing the sample doesn't help if it is already random. We did, however, fill a 0.7mm Lindemann capillary with crushed flakes, and take a photo as in Fig. 1. The rings from this thicker sample were continuous and of the same relative intensity as in Fig. 1, indicating the absence of texture.

Table II summarizes the quantitative results on texture for  $x = 0.22$  and  $x = 0.24$ . While the peak ratios vary with composition, at neither composition, given the provisos about statistics, do they vary significantly between reflection and transmission. With no indication in Fig. 1 of texture about a normal to the flake, nor any in Table II as we rotate  $90^\circ$  about a line in the surface, we conclude, together with the capillary results, that there is very little texture. This is not surprising for a chill zone with fine grain size. But it is unusual for grains that, as we shall see, appear columnar and extend essentially from the front to the back of the flake.

Figs. 3(a) and 3(b) address the issue of the limited correlation range first reported by Bancel et al<sup>14</sup>. In that work, all peaks appeared broad and the peak ( $N = 20$ ) at  $Q \approx 3.04\text{\AA}^{-1}$  appeared still broader. We have fit our peaks with Gaussian profiles convoluted with the instrumental resolution function measured off a perfect Si crystal. Fig. 3(a) shows the result at  $Q = 2.894\text{\AA}^{-1}$  ( $N = 18$ ). The fit is good given our statistics and the Gaussian width translates to a correlation range,  $L$ , of  $\sim 330\text{\AA}$ , where  $\Delta Q = 2\pi/L$ . The correlation range for  $x = 0.20$  is  $\approx 380\text{\AA}$ , while for  $x = 0.24$   $L \approx 480\text{\AA}$ . This latter value is, to our knowledge, the largest correlation range observed in quasicrystalline material and we are currently doing high-resolution microscopy on this material.

At  $Q \approx 3.04\text{\AA}^{-1}$  ( $N = 20$ ) the profile cannot be fit by a single Gaussian as it shows an asymmetric shoulder to low  $Q$ . The next simplest fit uses two Gaussians and that fit is indicated in Fig. 3(b). It is again satisfactory but not perfect, especially on the high  $Q$  side of  $3.04\text{\AA}^{-1}$ . Table III lists the values of the  $Q$  positions for the two Gaussians and their separation for the three samples. Very roughly, the value of  $Q_2 - Q_1$  (peak minus shoulder) is of the same order as the inverse correlation range or peak width at either one, where  $\Delta Q_1$  and  $\Delta Q_2$  are the unfolded Gaussian widths at each. Both  $Q_1$  and  $Q_2$  appear to increase with increasing Mn content as shown by Schaefer et al<sup>26</sup> for the pure Al-Mn quasicrystals. The ratio of the height of the peak at  $Q_1$  to that at  $Q_2$  decreases as the perfection (correlation range) increases, where we treat  $x = 0.20$  and  $x = 0.22$  as nearly equal when both ( $N=18$ ) and ( $N=20$ ) peaks are used.

The asymmetric broadening of the peak at  $Q \approx 3.04\text{\AA}^{-1}$ , together with a symmetric profile at  $Q \approx 2.89\text{\AA}^{-1}$ , appears as well in the neutron diffraction pattern.<sup>24</sup> With neutrons, however, these two peaks are weak, not only with respect to the Al lines but also with respect to several other quasicrystalline peaks. Whether our fit to two Gaussians at  $Q \approx 3.04\text{\AA}^{-1}$  is correct (appropriate) or only an interesting fit cannot be completely answered and we will return to this point in the Discussion.

### 3. Scanning Electron Microscopy (SEM)

The x-ray photographic observation of a grain size on the order of  $18\mu\text{m}$  at all three compositions, together with the absence of texture, suggested a SEM study of the flakes used in the x-ray work. Fig. 4(a) shows a fractured flake of  $x = 0.20$  in cross section. The surface in contact with the copper wheel is at the top where we can see a chill zone on the order of a few microns thick before the decidedly columnar structure takes over. This structure is characterized by clusters of dendrite arms of approximately  $0.6\mu\text{m}$  in diameter that may be seen in the center of Fig. 4(b) which was taken at the bottom of 4(a). Our

ability to see the dendrite arms depends upon appreciable shrinkage of the liquid remaining after the arms have grown. This is a classic growth phenomenon in which the last liquid surrounding the dendrites shrinks back on solidification.<sup>27</sup> The extension of the elongated structure from the wheel side to the bottom surface of Fig. 4(a) suggests a grain size in this material comparable to the sample thickness.

Fig. 5 is taken on the chilled wheel surface and shows an interesting morphology. Rather than the dendritic structure typical of the region away from the wheel, we see a dense arrangement of geometrical shapes with a couple of well-defined pentagonal dodecahedra that happen to be isolated enough to be distinguished. This surface side of the chill zone in Fig. 4(a) is thus characterized by geometrical quasicrystallites with clear evidence of dodecahedral symmetry on a scale of  $\sim 0.4 - 0.5 \mu\text{m}$ . While such (nominally) non-crystallographic external shapes have hitherto been associated in fine particles with internal microtwinning<sup>28</sup>, which has also been suggested for quasicrystals<sup>29</sup>, the overwhelming evidence in quasicrystals would seem to rule out this interpretation.<sup>18,30</sup> The dodecahedra in Fig. 5 then may well be nice examples of external shape reflecting internal symmetry. The pentagonal faces can be associated with planes in which the rapid growth direction is normal to a 5-fold axis so that pentagonal facets grow out and touch. Alternately these facets may reflect more an equilibrium shape determined by anisotropic surface energy rather than kinetic factors.

The distinction between the morphology at this surface and the dendritic regime above the chill zone, where the dendrite arms represent instabilities leading to a growth along 3-fold axes<sup>26</sup>, is shown in Fig. 6. In interpreting these SEM photos it should be kept in mind that there are ten 3-fold axes along which dendrites may propagate assuming, of course, that these alloys follow the same growth mode as the pure Al-Mn alloys. Figs. 6(a) and 6(b) are of the sur-

face of a flake of  $x = 0.20$  away from the wheel (the bottom surface in Fig. 4(a)). There are clear indications of oriented clusters of dendrite arms from which the last liquid has shrunk away. Figs. 6(c) and 6(d) are of an identical surface from the same material etched for a few seconds to reveal overall morphology and distribution of quasicrystal dendrite clusters. From Figs. 6(c) and 6(d) in particular we may estimate the size of the contiguous clusters that cover the surface to range between about 12-21  $\mu\text{m}$ . This is quite close to our x-ray estimate and enables us to identify a coherently diffracting grain of a single orientation as a single quasicrystalline dendrite cluster. That these seem to be randomly oriented may be inferred both from the x-ray work and from the surface of Fig. 6(a) where pentagonal sections are occasionally but not always observed. The small quasicrystallites that remain at the surface in 6(a) would appear to be the fragmented ends of dendrite arms.

With this confirmation of the x-ray estimate of from one to, at most, a few grains per thickness, the absence of texture in this columnar structure becomes more remarkable. Assuming the dendrites to be instabilities nucleated at isolated "crystallites" in the chill zone, they can grow in a great variety of directions because of the high multiplicity and still retain an approximate columnar appearance. To illustrate this variety we found a region of the surface of Fig. 6(a) which had broken away to reveal the interior. Fig. 7(a) shows the boundary of such a region with the adjacent top surface while Fig. 7(b) shows an area completely exposed. The shrinkage is very clear here--no etching (or decanting) has been done--and the range of dendrite orientation, each cluster belonging to a separate quasicrystalline grain of unique orientation, is notable. The sizes of the packets or clusters varies in Fig. 7(b) from about 9  $\mu\text{m}$  to about 18  $\mu\text{m}$ . The width of the arms isolated by shrinkage is again quite regularly between 0.5  $\mu\text{m}$  and 1  $\mu\text{m}$ .

#### 4. Transmission Electron Microscopy (TEM)

We present here limited TEM observations on thinned flakes of the same material, at  $x = .20$ , examined in Figs. 6 and 7. Fig. 8 is a bright field micrograph taken from a region that must lie well below the level of the shrinkage seen in Fig. 7(b) because there is no evidence of porosity. In fact, although the sample was thinned from both sides, the section in Fig. 8 is most likely close to the wheel side or chill zone. Large macroscopic grains of about  $0.6 - 0.8 \mu\text{m}$ , comparable to the size of a dodecahedron in Fig. 5 or the width of a dendrite arm in Fig. 9, are seen in bright and dark contrast with edges that appear somewhat scalloped. Internal to these grains, and most visible when the grains are off the direct strong diffraction condition, is a rather regular array of cellular structure whose size is around  $40 - 120 \text{nm}$ . This structure resembles the cellular growth pattern associated with moderate growth rates during solidification in which the depleted liquid is rejected to the boundaries as the crystalline (or quasicrystalline) front advances. The scale is, in addition, close enough to suggest a relation to the  $300 - 400 \text{\AA}$  correlation range noted earlier in connection with the x-ray profiles.

To test the interpretation of cellular growth in Fig. 8 we carefully thinned another flake of the same batch at  $x = 0.20$  to permit the observation of dendrite arms near the surface opposite the wheel. Clearly substructure in a single dendrite arm cannot be due to cellular growth. Figs. 9(a) and 9(b) are from such an area viewed in the weak beam dark field (WBDF) mode. In this mode the deviation from the exact Bragg condition is substantial and strong dynamical contrast effects such as bend and strain extinction contours are absent. Instead, contrast arises from regions of the sample that vary slightly in orientation and thus in the degree to which they approach a stronger diffraction condition. In Fig. 9(a) the entire left portion of the sample is nearer strong

diffraction. At the right the WBDF condition is more nearly satisfied and we see an array of substructure boundaries or cells, albeit somewhat less well-defined than in Fig. 8. The size, however, is similar, namely 50-100nm. In this case, where the substructure boundaries diffract more strongly, we cannot attribute the boundary material to rejected Al because the image is taken from a single dendrite arm. In addition, as is clear in the enlarged image in Fig. 9(b), there is distinct mottling within a cell on a scale of  $\sim 2\text{-}5\text{nm}$ , similar to that noted by Field and Fraser<sup>29</sup> and attributed by them to possible microtwinning. As we noted above, microtwinning in these alloys has essentially been eliminated as an explanation for their remarkable microstructure<sup>18,30</sup>, but the 2-5nm mottling remains interesting and has also been seen recently by Urban et al<sup>19</sup>.

## 6. Summary and Discussion

We have presented here a series of x-ray and electron microscopic observations of quasicrystalline structure covering a considerable range of length scales or sizes. Our principle results include the following observations:

- a) The absence of texture is established in quenched flakes of  $\text{Al}_{.94-x}\text{Mn}_x\text{Si}_{.06}$  with  $x = 0.20, 0.22$  and  $0.24$ .
- b) Spotty Debye rings are seen on an x-ray photograph, giving clear x-ray evidence for single quasicrystal grains, from which a mean grain diameter (depending on sample shape) may be estimated to be between  $13$  and  $18\mu\text{m}$ . This means that a flake of  $\sim 0.035\mu\text{m}$  thickness has at most only a few grains across its thickness.
- c) The indexing of our powder photograph is accomplished using the scheme of Cahn et al<sup>13</sup> to show that, aside from weak residual Al lines, the material is single phase quasicrystalline. Both rough intensity comparisons and the systematic trend of spottiness in the Debye rings confirm the indexing.
- d) High resolution diffractometer determinations are made of correlation ranges of  $330\text{-}480\text{\AA}$ , the latter being the largest correlation range reported to date. The general range, however, agrees with Bancel et al<sup>14</sup> and Mozer.<sup>24</sup>

e) We measure an asymmetric low-Q shoulder on the 2-fold peak at  $Q = 3.04\text{\AA}^{-1}$  which is absent on the 5-fold peak at  $Q = 2.89\text{\AA}^{-1}$ . This is again similar to the report of Bancel et al<sup>14</sup> on an anomalously broad peak at  $Q = 3.04\text{\AA}^{-1}$ , but our pattern is cleaner and we can fit the peak using 2 Gaussians whose separation is comparable to the inverse correlation range. As the Mn content,  $x$ , increases from 0.20 to 0.24 the correlation range appears to increase somewhat and the relative heights of shoulder to peak at  $Q = 3.04\text{\AA}^{-1}$  decreases, i.e. as the material becomes more perfect, the asymmetry may perhaps diminish.

f) SEM photos on a typical flake from the batch at  $x = .20$  reveals a chill zone of  $\sim 3\mu\text{m}$  at the wheel surface followed by a dendritic growth mode. At the wheel surface, one can detect a dense array of geometrical shapes assumed by the solidified alloy, among which are isolated pentagonal dodecahedra. Ruling out microtwinning as a cause of this external shape, we may take it as a consequence of internal symmetry. At the opposite surface, pronounced shrinkage is observed which occasionally reveals a pentagonal external morphology of a dendrite cluster that terminates at the surface. Below the surface there is a dense array of dendritic clusters whose arms are  $\sim 0.5 - 1.0\mu\text{m}$  in diameter and whose lateral extent, both at the top surface and below, is comparable to the x-ray grain size determination of  $\sim 13-18\mu\text{m}$ .

g) TEM reveals, in both bright field and weak beam dark field (WBDF) images, an assortment of substructure. On a  $1-2\mu\text{m}$  scale there are grains near the wheel surface as well as dendrite arms near the opposite surface. Within the grains is a reasonably regular array of substructure boundaries on a scale of  $40-100\text{nm}$ , which appears as well--though perhaps less regular-- within a single dendrite arm thus ruling out segregation as a probable cause. Inside these cells, whose boundaries are brought into strong diffraction and appear bright in the WBDF image, is a mottled or speckled contrast on a scale of  $2-5\text{nm}$  which again suggests

a uniform distribution of very small regions oriented at slightly varied angles with respect to each other and the beam. While the substructure boundaries occur on a scale comparable, at the lower limit, with the correlation range of  $\sim 400\text{\AA}$  (40nm), the mottling is on a much finer scale. The asymmetric line shape or low- $q$  shoulder on the 2-fold peak ( $N=20$ ) suggests a few possibilities of interpretation. The first, most straightforward, explanation is that it is a quasicrystalline peak not listed in the lowest hierarchy of intensity given in Table I. It will generally be true that the intensity of a peak will fall off very rapidly with its distance from the cut plane<sup>12,13</sup> and this conclusion is modified only by the realization that the bounded volume in  $Z^6$  introduces ripples into the transform "fall-off" function so that a peak far away from the cut plane may by chance pick up intensity from a secondary ripple. In addition, because we do not know the actual structure factor, but only that for the primitive lattice, there may be some systematic surprises, even in the close vicinity of a strong peak.

The main candidates for the extra peaks in Table III at  $Q_1 = 3.025\text{\AA}^{-1}$  ( $x=.20$ ),  $Q_1 = 3.031\text{\AA}^{-1}$  ( $x=.22$ ) and  $Q_1 = 3.035\text{\AA}^{-1}$  ( $x=.24$ ) are those whose values can fit the measured ones, scaled to concentration, and which are closest to the cut-plane. Table IV gives the only two possibilities we could prefer. Only one of these is appropriate at all  $x$ , and the scale factor must be adjusted accordingly to have its  $Q$  value slide with composition.

While it is tempting to assign one of these (which one depends on our exact choice of scale factor or "lattice parameter"), we can see that the values of  $Q_c$  are quite large compared to the stronger peaks in Table I. They are therefore intrinsically extremely weak, even with their large multiplicity factors. Without evidence for a more complete set of observed peaks or shoulders whose predicted intensity is so low, we are reluctant simply to assign the indices in Table IV to the shoulder in Fig. 3(b).

Another interesting source of asymmetrical broadening of the 2-fold peak, which leaves the 5-fold peak symmetrical, is the possibility of a cubic approximant<sup>31</sup> to the exact quasicrystal, generated by a near-irrational cut in  $Z^6$ . Choosing a cubic cell size,  $a_0$ , of 53.545Å as suggested by Cahn et al<sup>30,31</sup> to give good agreement with positions of the other lines in the pattern, a splitting ( $\Delta Q = Q_1 - Q_2$ ) of  $-0.005\text{\AA}^{-1}$  would appear on the high-Q side of  $3.04\text{\AA}^{-1}$ . Lowering  $a_0$  increases  $\Delta Q$  but ruins the rest of the pattern as the quasicrystal is not, in fact, cubic. A lower symmetry approximant may produce a greater splitting but it splits the 5-fold peak as well.

It might also be possible to explain the shoulder as a contaminant peak from one of the other phases that the system exhibits.<sup>26</sup> This also seems incorrect, however, as the shoulder appears in all our patterns, and in the neutron pattern<sup>24</sup> as well, without any evidence for the strong peaks of other known phases.<sup>26</sup>

An interesting way of looking at defective quasicrystals has recently been suggested by Stephens and Goldman<sup>32</sup> who propose linear (or planar) spacing disorder as a model for quasicrystalline diffraction from imperfect pentagonal (or icosahedral) packing. The diffraction from this model, effectively identical to a defective Penrose tiling in 2 or 3 dimensions, is described by Stephens and Goldman<sup>32</sup> using a formalism developed by Hendricks and Teller<sup>33</sup> for planar or linear (1-D) disorder which may be applied to two or more incommensurate spacings. An interesting consequence of this model is the existence of asymmetric broadening of selected Bragg peaks together with a considerable variation in peak breadth with diffraction order. Although all experimental quasicrystal peaks appear broad, with some broader than others, this model provides an interesting approach to defective tilings.

Relevant to this idea are the observations of Hiraga et al<sup>17</sup> and Tanaka et al<sup>20</sup> using high resolution electron microscopy. Fig. 1 of the RITU paper of Hiraga et al<sup>17</sup> shows an image normal to the 5-fold axis of a Al<sub>6</sub>Mn quasicrystalline grain. If one lays a ruler along the observed row of spots (or glances down them) it is clear that these rows, which effectively show the projected potential, begin and end without losing overall orientation. In other words, we may assign to adjacent rows of spots in the high resolution image a separation of either the unit  $1$  or the unit  $\tau$ . Thus, in a sequence of three rows with the spacing  $1 + \tau$ , as one proceeds down the rows, one row ends and another takes up to maintain the three parallel but with  $1 + \tau \Rightarrow \tau + 1$ . This introduces an array of what may be called sequence faults or errors whose frequency determines the perfection of the quasicrystal. Measurements on Fig. 1 of Hiraga et al<sup>17</sup> indicate a length of an uninterrupted line varying from 15-25nm (150-250Å), with two of the five sets of lines being considerably shorter than the other three. This length, over which a line of projected potential remains uninterrupted, is effectively comparable to a correlation range for the material. Within the rows there is a spacing of spots which follows a Fibonacci sequence for some distance until a defect is encountered; normal to the rows we then have sequences interrupted by faults every 150-250Å. The effect of this 1-D faulting, that preserves overall orientational order but may give rise to local distortions, could be similar to the calculation of Stephens and Goldman<sup>32</sup> and we are currently modeling it.

It would be nice to establish a connection between the defective Penrose tiling, the broadening observed in our diffraction patterns (Fig.3) and the mottling and cellular-like structure observed in WBDF TEM (Figs. 8 and 9), should such a connection exist. In this regard, Tanaka et al<sup>20</sup> have done quite high resolution electron diffraction on Al<sub>6</sub>Mn in which they show that the Bragg reflections actually appear to be composed of a collection of spots as if there

were a micro-mosaic spread. Their estimated angular range of one of these spots corresponds to  $\sim 300\text{\AA}$ . This is associated by Tanaka et al<sup>20</sup> with the finite correlation range observed in x-ray scattering.<sup>14</sup> We are, however, tempted to assign such a micro-mosaic distribution to the WBDF mottling in which case the length scales remain to be reconciled.

Ultimately we would like a description of the quasicrystalline structure which includes both its idealization and the real structure permitted by the growth conditions. As Tanaka et al<sup>20</sup> demonstrate quite beautifully with small area convergent beam electron diffraction, when a quasicrystalline structure is examined on progressively finer scales the 5-fold symmetry progressively degrades. This is also apparent in the image of Hiraga et al<sup>17</sup> and its optical transform (the exact 5-fold symmetry is lost). Adding defects enhances the effect by providing a limit to long range order.

#### ACKNOWLEDGEMENTS

This work was supported at the University of Houston by the NSF on grant no. DMR-82-14314. We wish to thank Mr. Chris Kinalidis of the SEM Laboratory of the University of Houston for assistance with the microscopy. Thanks for numerous discussions and helpful comments are due our colleagues at the NBS: J.W. Cahn, W. Boettinger, M. Kuriyama, G.G. Long, B. Mozer and R.J. Schaefer. We particularly appreciate the permission of Dr. Mozer to quote from work in progress. We also thank Drs. M. Hirabayashi and M. Tanaka for helpful correspondence.

The contribution of Dr. L. Bendersky was supported by the Defense Research Projects Agency (DARPA) and the Office of Naval Research (ONR).

## REFERENCES

1. D. Shechtman, I. Blech, D. Gratias and J.W. Cahn, Phys. Rev. Lett. 53, 1951 (1984).
2. D. Levine and P.J. Steinhardt, Phys. Rev. Lett. 53, 2477 (1984).
3. R. Penrose, Bull. Inst. Maths. Its Appl. 10, 266 (1974).
4. M. Gardner, Sci. Am. 236, 110 (1977).
5. A.L. Mackay, Physics Bull., Nov. (1976) p.495; Sov. Phys. Cryst. 26, 517 (1981); Physica 114A, 609 (1982).
6. R. Penrose, Math. Intelligencer 2, 32 (1979).
7. R. Penrose, private communication (1984).
8. This issue is also discussed by Nelson and Halperin in Science 229, 233 (1985), in connection with the formation of "dislocations" in a 2-D Penrose tiling.
9. S. Sachdev and D.R. Nelson, Phys. Rev. B32, 4592 (1985).
10. P. Bak, Phys. Rev. Lett. 54, 1517 (1985); Phys. Rev. B32, 5764 (1985).
11. R.K.P. Zia and W.J. Dallas, J. Phys. A18, L341 (1985).
12. V. Elser, Phys. Rev. B32, 4892 (1985).
13. J.W. Cahn, D. Shechtman and D. Gratias, NBS preprint-submitted to J. Mater. Sci.
14. P.A. Bancel, P.A. Heiney, P.W. Stephens, A.I. Goldman and P.M. Horn, Phys. Rev. Lett. 54, 2422 (1985).
15. M. Kuriyama, G.G. Long and L. Bendersky, Phys. Rev. Lett. 55, 849 (1985); G.G. Long and M. Kuriyama; M. Kuriyama and G.G. Long, NBS preprints - Acta Cryst. (in press).
16. L. Bursill and J. Lin, Nature 316, 50 (1985).
17. K. Hiraga, M. Hirabayashi, A. Inoue and T. Masumoto, Sci. Rept. RITU, A-32, 309 (1985); J. Phys. Soc. Japan 54, 4077 (1985).
18. R. Portier, D. Shechtman, D. Gratias and J.W. Cahn, J. Mic. Spectro. Elec. 10, 107 (1985).
19. K. Urban, N. Moser and H. Kronmüller, Phys. Stat. Sol. (a) 91, 411 (1985).
20. M. Tanaka, M. Terauchi, K. Hiraga and M. Hirabayashi, Sci. Rept. RITU-Ultramicroscopy (in press).

21. There is, however, a good agreement between the predicted hierarchy of intensity (see Refs. 12,13) and the experimental electron diffraction patterns, without regard to details of the atom positions or form factors and without attention to multiple scattering. This may be due both to the weak scattering from a quasicrystal (more kinematic) and to the fact that secondary scattering in these structures does not coincide with a strong primary scattering direction.
22. L.A. Bendersky and M.J. Kaufman, NBS preprint-Phil. Mag. (in press); C.H. Chen and H.S. Chen, AT&T Bell Labs preprint.
23. Int'l. Tables for Crystallography, Vol. A, D. Reidel, Boston (1983), p. 779; see also Ref. 13.
24. B. Mozer, private communication; this NBS neutron powder data is on ~ Al<sub>6</sub>Mn.
25. A. Taylor, X-Ray Metallography, Wiley, New York (1961), p. 667ff.
26. R.J. Schaefer, L.A. Bendersky, D. Shechtman, W.J. Boettinger and F.S. Biancaniello, NBS preprint-Met. Trans. (in press).
27. M.C. Flemings, Solidification Processing. McGraw-Hill, New York (1974), p. 240.
28. See the series of papers of Heinemann, Yang and co-workers: Jnl. Cryst. Growth 47, 177; 187; 274; 283 (1979).
29. R.D. Field and H.L. Fraser, Mat. Sci. Eng. 68, L17 (1984-85).
30. J.W. Cahn, D. Gratias and D. Shechtman, NBS preprint--letter submitted to Nature.
31. D. Gratias and J.W. Cahn, NBS preprint-submitted to Scripta Met.
32. P.W. Stephens and A.I. Goldman, SUNY, Stony Brook, preprint.
33. S. Hendricks and E. Teller, J. Chem. Phys. 10, 147 (1942).

TABLE I. Comparison of experimental data of Fig. 1 with the theory developed in Ref. 13. Experimental (film) Q values are scaled using the Al (111) reflection. A theoretical scale factor for Q is obtained by setting Q (theory) = Q (expt.) at Ring #1. Theoretical intensities do not include form factors, Lorentz and polarization factors, or multiplicities.

Experiment (Fig. 1)						Theory (Ref. 13)			
Ring #	D	$2ng$ $Q(=4\pi\sin\theta/\lambda)$	I	$I^*$	p	Q	$\Delta Q^\dagger$	Index	N**
	(mm)	( $\text{\AA}^{-1}$ )	(visual)		(mult.)	$\text{\AA}^{-1}$	$\text{\AA}^{-1}$	( $Z^6$ )	
1	26.8	1.635	ms	0.42	20	1.635	0.000	(111000)	6
2	31.2	1.893	w	0.36	30	1.887	-0.006	(111010)	8
3	41.9	2.510	vvw	0.27	60	2.497	-0.013	(211010)	14
4	45.1	2.688	- Al	(111)	---	---	---	---	--
5	48.9	2.897	s	1.00	12	2.904	0.007	(211111)	18
6	51.8	3.059	vs	0.59	30	3.054	-0.005	(221010)	20
7	56.1	3.286	w	0.21	80	3.269	-0.017	(222000)	24
								(221111)	
8	62.3	3.606	w	0.31	72	3.590	-0.016	(311111)	28
								(222110)	
9	74.9	4.228	m	0.51	60	4.215	-0.013	(322110)	38
10	76.9	4.324	vw	0.42	60	4.319	-0.005	(322111)	40
11	79.0	4.421	- Al	(220)	---	---	---	---	--
12	91.1	4.959	ms	0.95	30	4.941	-0.018	(332020)	52
13	111.0	5.746	w	0.69	60	5.732	-0.014	(432121)	70
14	113.5	5.837	vw	0.50	72	5.809	-0.028	(433110)	72
								(422222)	
15	136.3	6.597	vvw	0.20	300	6.599	0.002	(532221)	94
								(443121)	
								(443121)	
16	150.0	6.991	vw	0.67	60	6.988	-0.003	(533221)	104

\*  $I = (1/Q_c)$ , normalized to 1.0 at ring # 5. This is a very rough estimate of intensity--see Refs. 12,13.

$\dagger$   $\Delta Q = Q_{\text{theory}} - Q_{\text{experiment}}$

\*\* as defined in Ref. 13 - see text

$$d = \frac{\lambda}{2\sin\theta} \quad \frac{1}{d} = \frac{2\sin\theta}{\lambda} = g \quad g = 2ng$$

TABLE II. Ratios of the peak intensity over background ( $I_p$ ) at  $Q \approx 3.04\text{\AA}^{-1}$  to that at  $Q \approx 2.89\text{\AA}^{-1}$  for  $x = 0.22$  and  $0.24$ . Reflection data are compared with transmission data on the same flake.

$I' = I_p(3.04)/I_p(2.89)$	$x = 0.22$	$x = 0.24$
$I'$ (reflection)	1.30	1.46
$I'$ (transmission)	1.32	1.49

TABLE III. Peak positions for the two Gaussian peaks fit to the data at  $Q \approx 3.04 \text{ \AA}^{-1}$ .  $Q_1$  is the low  $Q$  shoulder on the main peak at  $Q_2$ ;  $\Delta Q$  is the FWHM of each. Ratios of peak intensity are also given.

$x$ (at. fract. Mn)	$Q_1$ ( $\text{\AA}^{-1}$ )	$\Delta Q_1$ ( $\text{\AA}^{-1}$ )	$Q_2$ ( $\text{\AA}^{-1}$ )	$\Delta Q_2$ ( $\text{\AA}^{-1}$ )	$I_1/I_2$
.20	3.025	.016	3.040	.016	.37
.22	3.031	.015	3.046	.015	.37
.24	3.035	.013	3.050	.013	.15

TABLE IV. Candidates for the (assumed) secondary peaks at  $Q_1 = 3.025 - 3.035 \text{ \AA}^{-1}$ , listed in Table III, that were used to fit the profile at  $Q = 3.04 \text{ \AA}^{-1}$  in Fig. 3(b).  $Q_c$  is the distance from the cut plane in the cut-projection method (see text and Ref. 13 for notation). Only one of these candidates, scaled for composition changes, is needed to account for the data.

$Q_1$ ( $\text{\AA}^{-1}$ )	$p$ (mult.)	$Q_c$ ( $\text{\AA}^{-1}$ )	Index ( $Z^6$ )	Index ( $R^3$ ) ( $h/h'$ , $k/k'$ , $l/l'$ )
3.027	120	6.704	312 $\overline{11}$ 0	4/0 2/2 2/2
	120		130112	0/4 $\overline{2}$ /2 2/2
3.031	120	10.482	321 $\overline{31}$ $\overline{1}$	6/1 2/0 3/0
	120		3 $\overline{1}$ 3 $\overline{1}$ 21	4/1 2/2 $\overline{3}$ /4

\* Both of these  $Q_1$  values are scaled to a peak for  $N=18$  at  $Q = 2.898 \text{ \AA}^{-1}$ .

## FIGURE CAPTIONS

Fig. 1. (a) Filtered  $\text{MoK}_\alpha$  transmission pinhole photograph of an intact flake of spin-quenched  $\text{Al}_{.70}\text{Mn}_{.24}\text{Si}_{.06}$  taken with the incident beam normal to the flake. The numbers are indices to the Debye rings for guidance in Table I. The spottiness of these rings is an indication of the large grain size which may be determined from a count of these spots (see text);

(b) 2x enlargement of Fig. 1(a). The radial elongation of many of the spots demonstrates the elongation, normal to the flake, of the individual quasicrystal grains that are coherently diffracting.

Fig. 2. X-ray diffractometer scans from the  $x = 0.22$  sample using  $\text{CuK}\alpha_1$  radiation. Measured intensity in counts per second, versus scattering vector,  $Q = 4\pi\sin\theta/\lambda$ .

(a) reflection geometry; (b) transmission geometry

Fig. 3. Fit to the reflection data of Fig. 2(a) using Gaussian profiles convoluted with the measured instrumental profile.

(a)  $Q \approx 2.894\text{\AA}^{-1}$ ,  $N=18$ . The inner curve is the instrumental profile.

(b)  $Q \approx 3.04\text{\AA}^{-1}$ ,  $N=20$ . The measured profile cannot be fit using a single Gaussian. The fit shown corresponds to two overlapping Gaussians (see Table III).

Fig. 4. SEM photographs of the edge of a flake with  $x = 0.20$ . The surface in contact with the Cu wheel is at the top in (a). A chill zone of  $\sim 3\mu\text{m}$  in thickness is present. The remainder of the sample in (a) exhibits a columnar structure. (b) shows, in magnification near the bottom surface, the extension of clusters of dendrites growing up from the chill zone that are revealed by shrinkage of the surrounding liquid upon solidification.

Fig. 5. SEM photograph of the chill zone surface of Fig. 4(a). An outline has been made of a few of the isolated pentagonal dodecahedra. The clear geometrical shape of all of the particles is notable.

Fig. 6. SEM photographs of the bottom surface of the flake in Fig. 4(a) which is away from the copper wheel surface.

(a) and (b) are unetched surfaces showing the termination of dendrite clusters revealed by shrinkage. Occasional pentagonal symmetry is present. (c) and (d) are etched surfaces revealing the inner dendrite morphology and, in (c), a rather uniform grain size of  $\sim 12\text{-}21\mu\text{m}$ .

Fig. 7. SEM photographs of the same surface as in Fig. 6 at a place where the uppermost surface layer chipped off to reveal the underlying dendritic structures and the obvious shrinkage. (a) at the boundary of the chipped region; (b) into this region.

Fig. 8. Bright field TEM micrograph of a region near the chill zone showing a macro grain size of  $\sim 0.6\text{-}0.8\mu\text{m}$  with an internal substructure on a scale of  $\sim 40\text{-}120\text{nm}$ .

Fig. 9. Weak beam dark field (WBDF) TEM micrographs of a dendrite arm near the bottom of Fig. 4(a), i.e. away from the chill zone. In (a) much of the left side of the dendrite is too strongly diffracting. (b) is a magnification of the right side of (a) in which substructure boundaries similar in size to those of Fig. 8 are visible (bright) along with fine scale mottling of about  $2\text{-}5\text{nm}$  in extent.

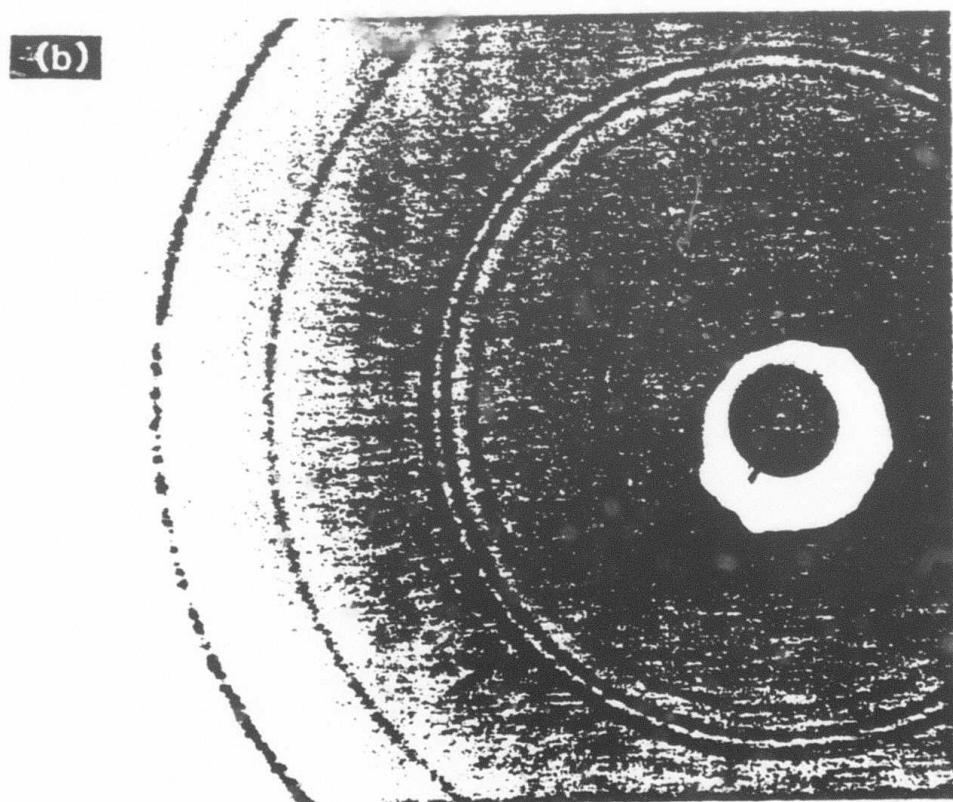
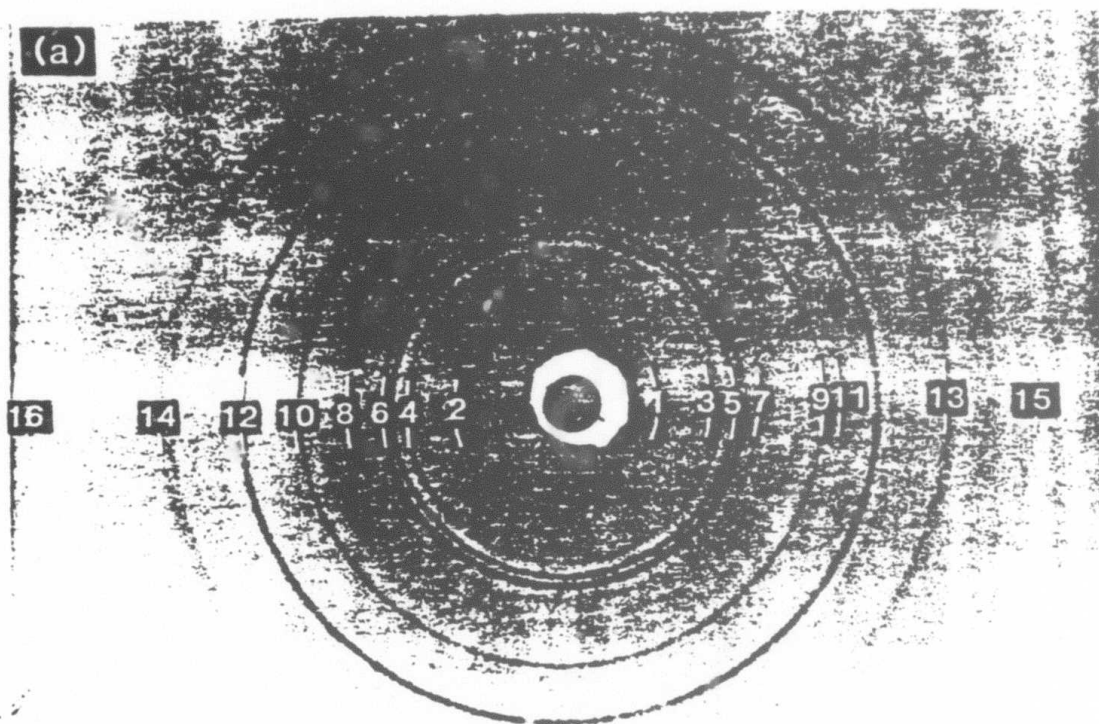


Fig. 1

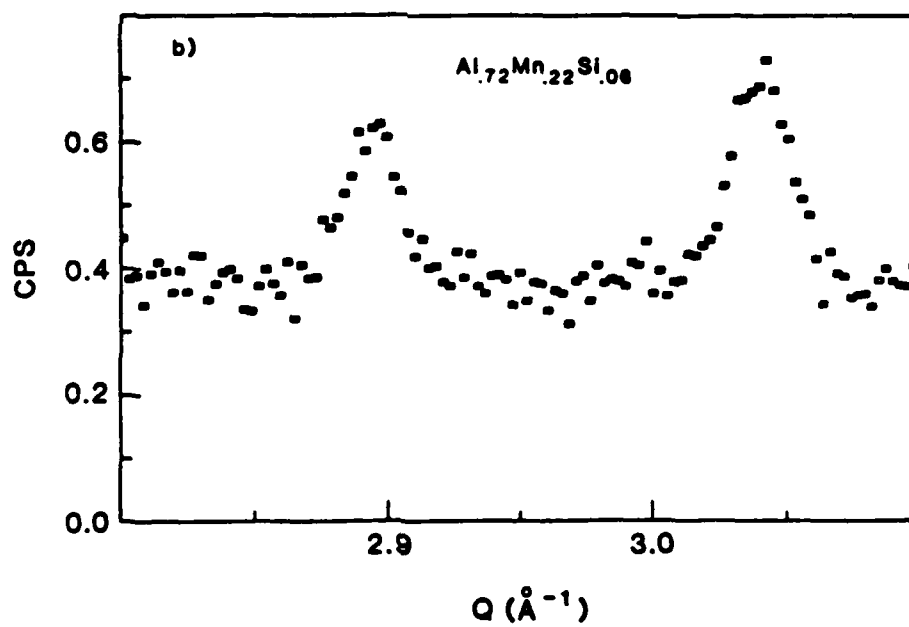
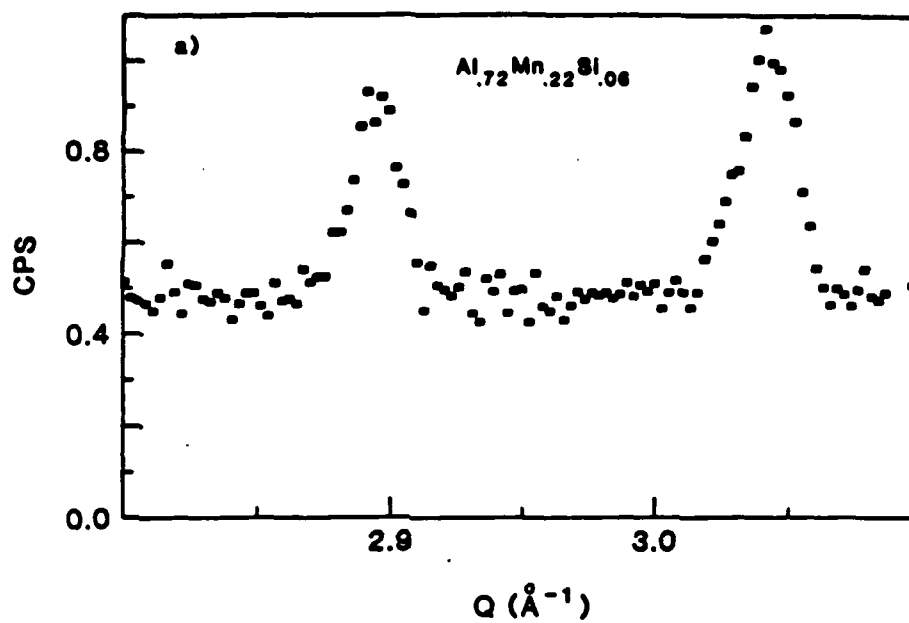


Fig. 2

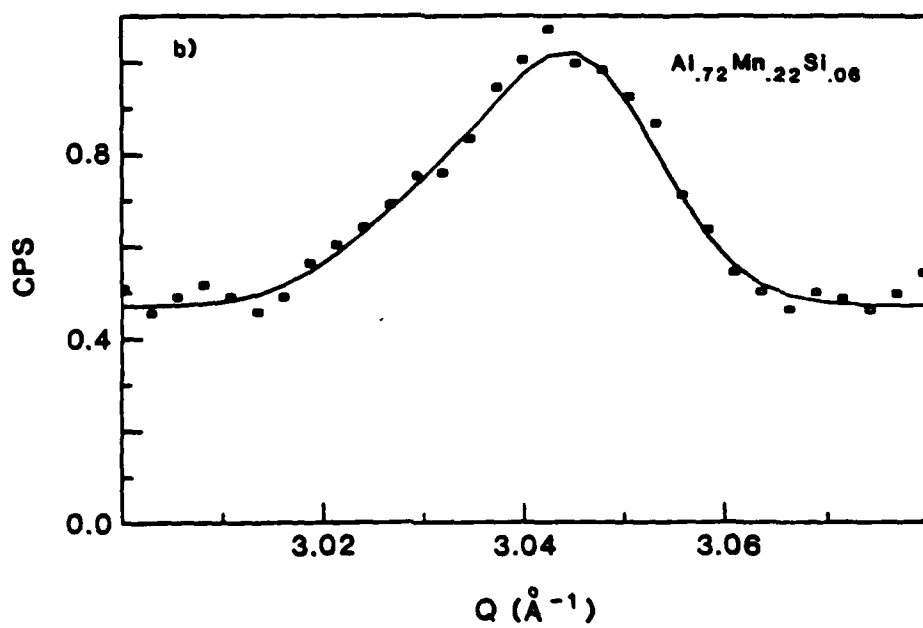
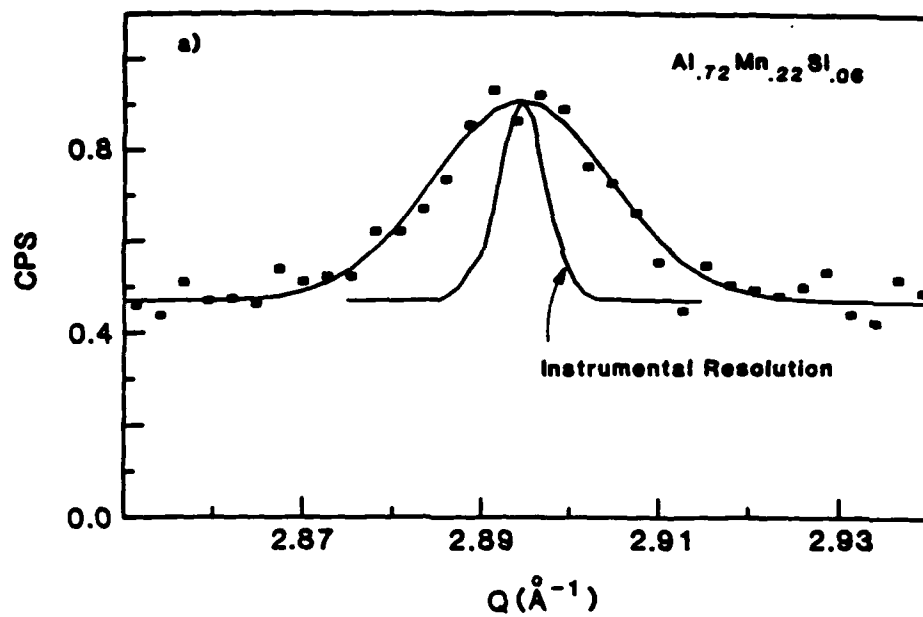


Fig. 3

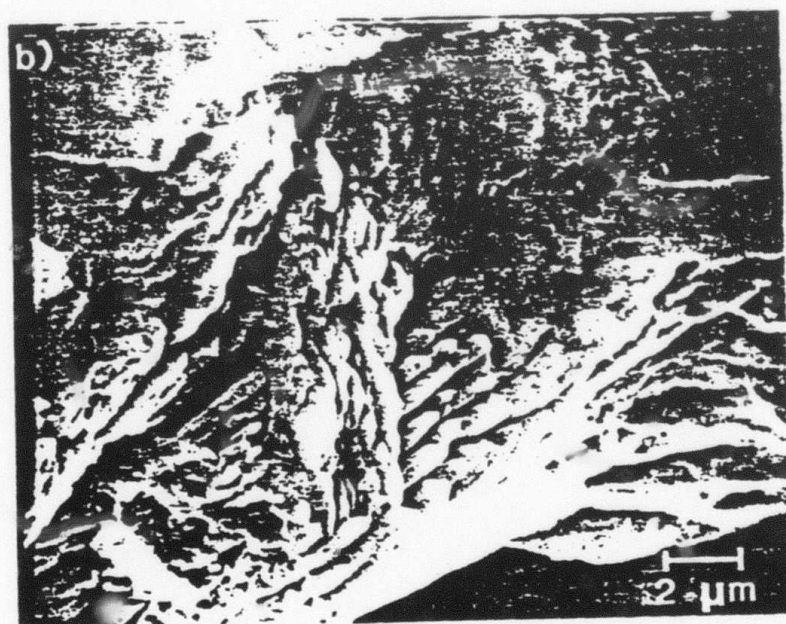
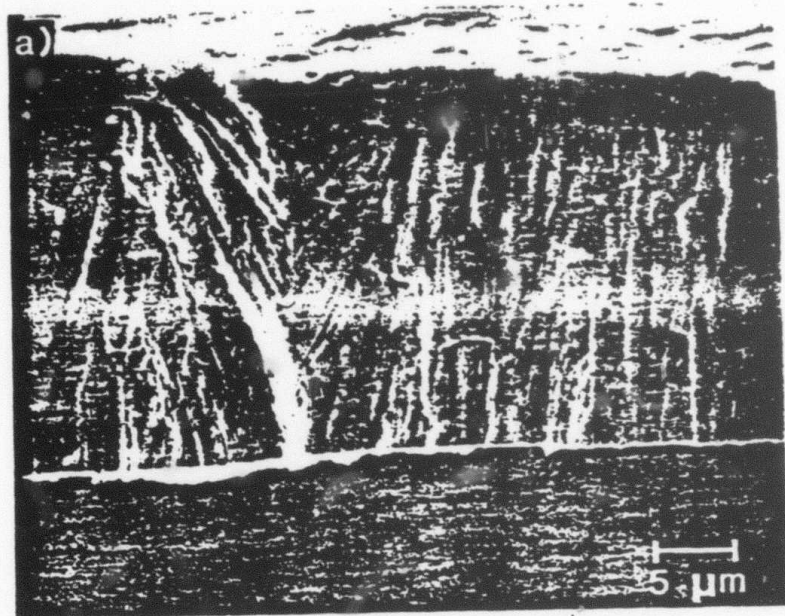
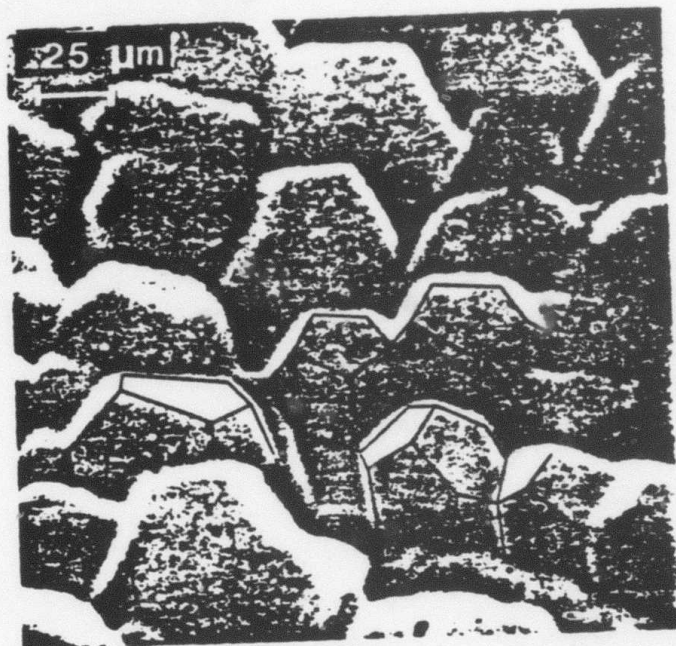
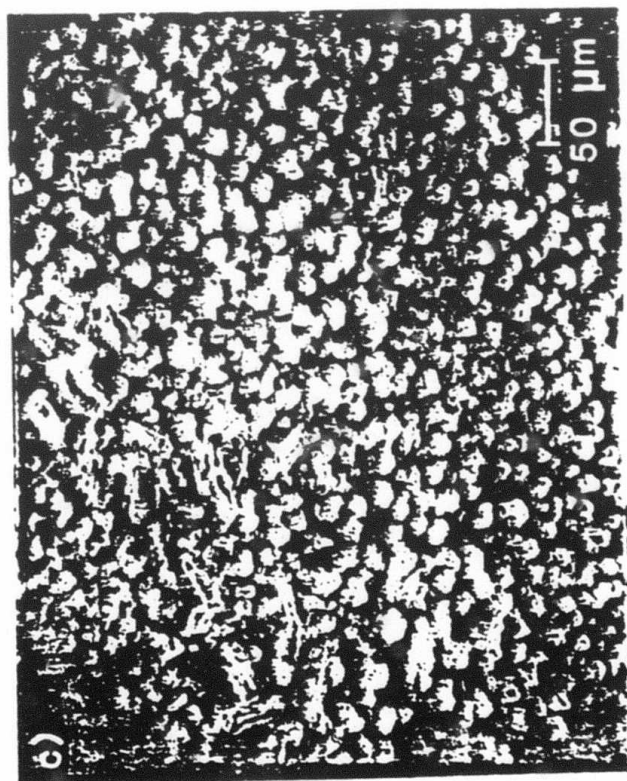
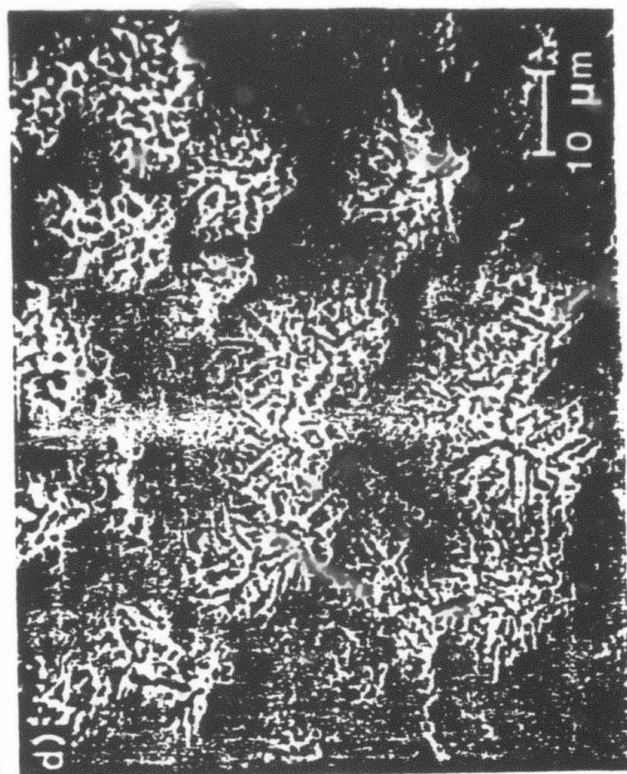
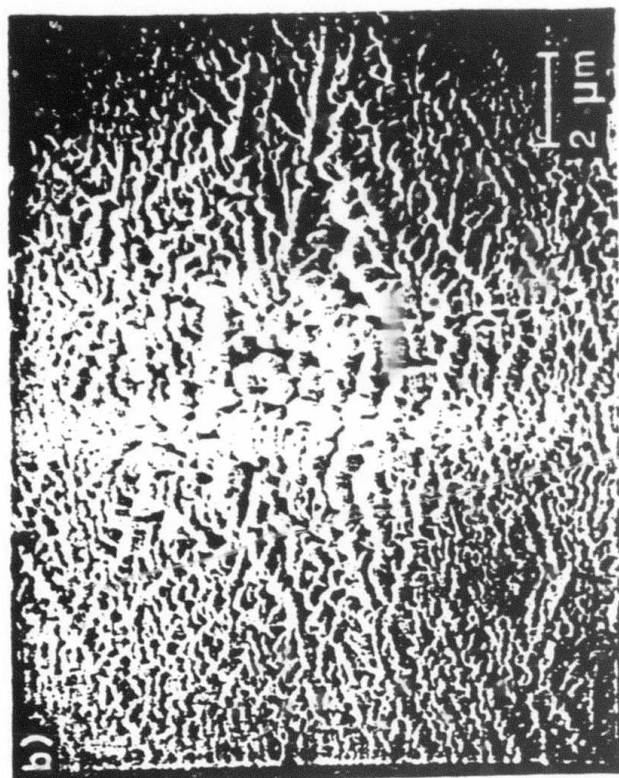


Fig. 4



*Fig. 5*



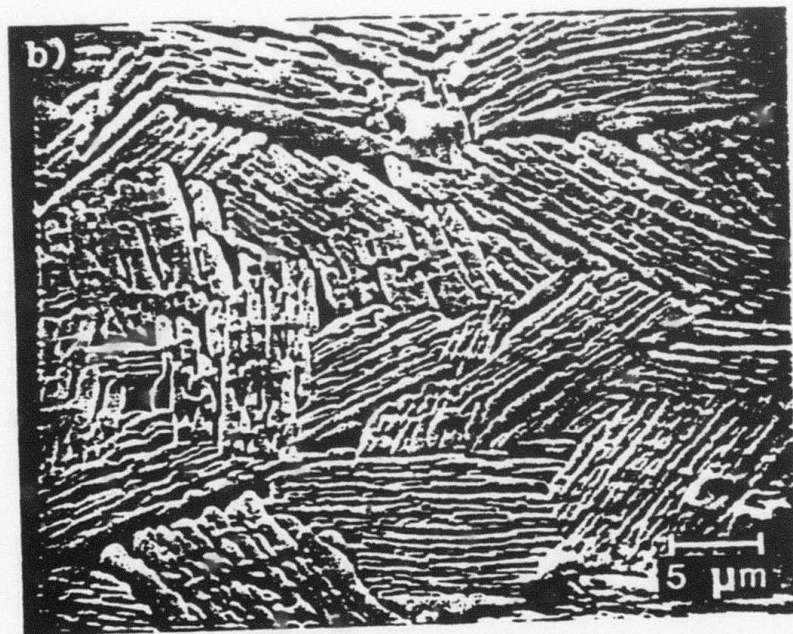
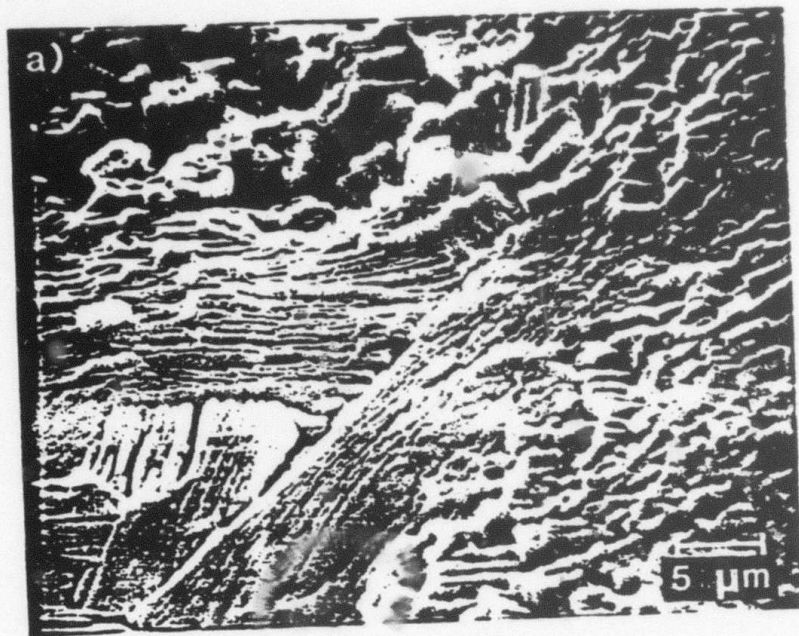
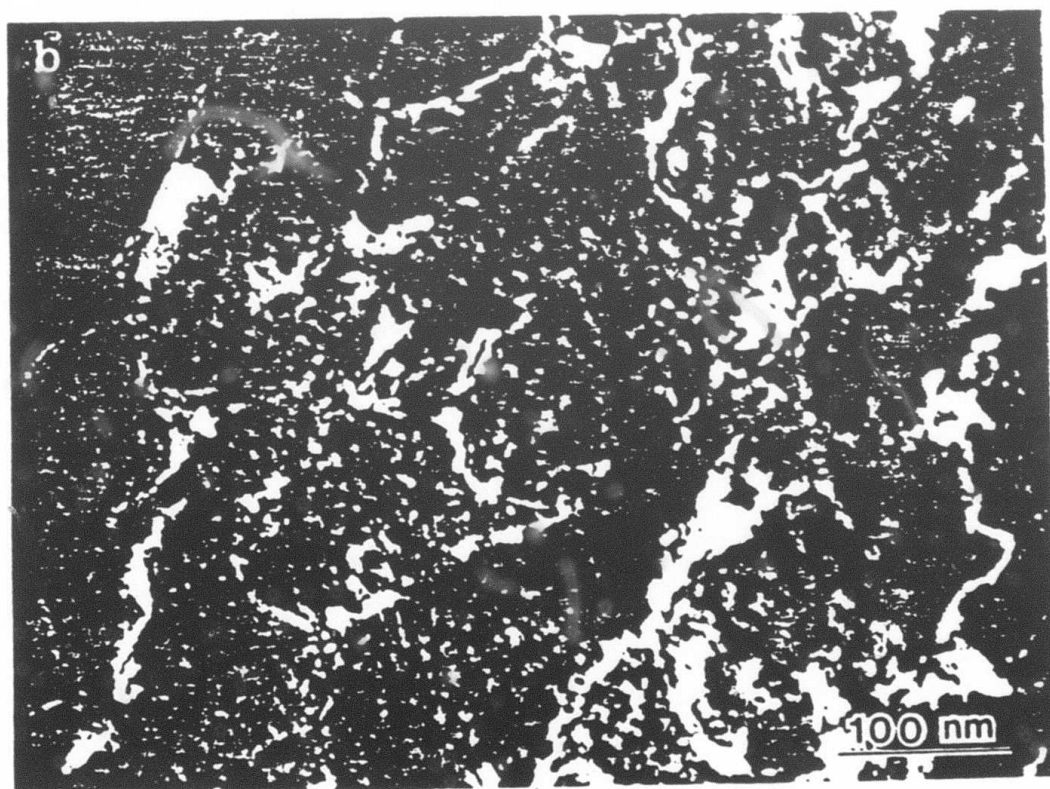
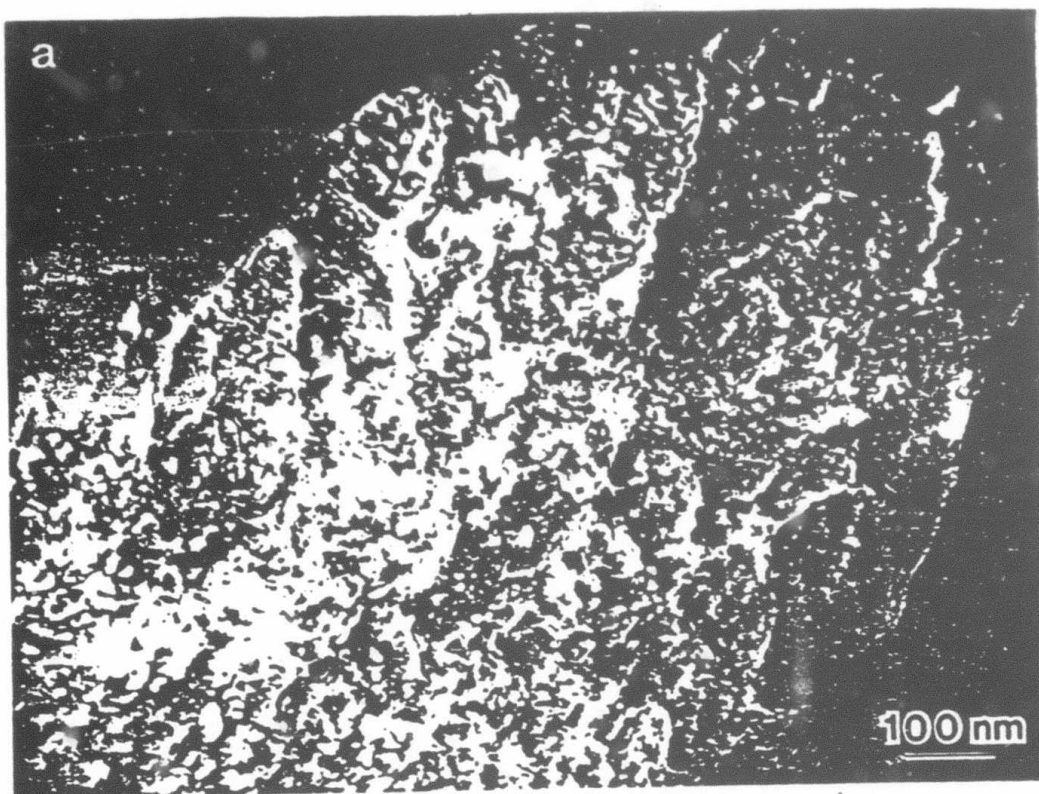


Fig. 7



*Fig. 8*



Fin. 9

# Stable and Metastable Phase Equilibria in the Al-Mn System

J.L. MURRAY, A.J. MCALISTER, R.J. SCHAEFER, L.A. BENDERSKY,  
F. BIANCANIELLO, and D.L. MOFFAT

The aim of the present investigation was resolution of certain obscure features of the Al-Mn phase diagram. The experimental approach was guided by assessment of the previous literature and modeling of the thermodynamics of the system. It has been shown that two phases of approximate stoichiometry "Al<sub>4</sub>Mn" ( $\lambda$  and  $\mu$ ) are present in stable equilibrium,  $\lambda$  forming by a peritectoid reaction at  $693 \pm 2$  °C. The liquidus and invariant reactions as proposed by Goedecke and Koester have been verified. A map has been made of the successive non-equilibrium phase transformations of as-splat-quenched alloys. Finally, the thermodynamic calculation of the phase diagram allows interpretation of complex reaction sequences during cooling in terms of a catalogue of all the metastable invariant reactions involving (Al), Al<sub>6</sub>Mn,  $\lambda$ ,  $\mu$ ,  $\phi$ , and Al<sub>11</sub>Mn<sub>4</sub> phases.

## I. INTRODUCTION

Despite both technological and scientific interest in Al-Mn alloys, one can reasonably assert that prior to 1970 the only definitively established feature of the Al-Mn phase diagram was the melting point of Al. Although the Al-rich side of the diagram has since been clarified, not all the observed phases of the system have yet been accounted for as stable or metastable phases, nor have all experimentally observed reactions been interpreted in terms of a self-consistent picture of the stable and metastable phase equilibria. Some of the reasons are evident. Mn has been available in high purity only for the last decade or so; it has a high vapor pressure even at relatively high Al-content, and it is readily oxidized.

But there lurk more subtle traps that have caught many investigators of unquestionable ability. Long-lived metastable phases occur in surprising numbers and reactions leading to the stable equilibria are sluggish. No experiment in this system can be unambiguously interpreted unless the phases are characterized structurally and the approach to equilibrium is demonstrated. Most of the reactions seen during cooling from the liquid state do not pertain to the stable equilibrium diagram at all. Therefore an analysis of the thermodynamics of the system is needed to construct a self-consistent model of the nature, number, and sequence of the possible reactions.

In this paper we present experimental work by differential thermal analysis, transmission electron microscopy, and x-ray diffraction, on alloys containing between 12 and 55 at.% Mn. Samples were prepared in the form of ribbon by splat-quenching of the liquid. By use of these homogeneous or at worst very finely segregated samples, equilibrium could be approached far more rapidly than by using conventional bulk samples. Our results and other

observations critically selected from the literature are interpreted in terms of a calculation of stable and metastable equilibria from thermodynamic functions. We have revised some features of the generally accepted stable diagram, notably in the region near 20 at.% Mn. We have also reinterpreted thermal analysis cooling data in terms of a sequence of six thermodynamically predicted metastable peritectic reactions.

Considerable experimental work remains to be done to verify the details of this composition and temperature region of the diagram. By the present study we have established the feasibility of our experimental approach. The present calculation of the diagram is shown to provide a suitable basis for interpreting non-equilibrium experiments. While the calculation of the diagram will be susceptible to improvement as more accurate thermochemical data are obtained, it places limits, for the first time, on the range of possibilities for the binary Al-Mn phase equilibria.

## II. SUMMARY AND REINTERPRETATION OF THE LITERATURE

Previous experimental studies relevant to the present investigation were made by Taylor [1], Goedecke and Koester [2], Dix et al. [3], Phillips [4], Kono [5], Koester and Wachtel [6] and Koch et al [7]. The latter two studies were confined to more Mn-rich compositions and will be discussed below. The most striking conflicts occur in the range out to 25 at.% Mn.

The two most recently proposed versions of the Al-rich side of the diagram, due to Taylor [1] and Goedecke and Koester [2], are compared in Fig. 1. According to Goedecke and Koester, the phases labelled  $\mu$  and  $\phi$  by Taylor do not belong to the equilibrium diagram, and therefore neither do peritectic reactions shown at 880 and 822 °C by Taylor. Goedecke and Koester identified  $\phi$  as a metastable phase that participates in two metastable peritectic reactions  $L + Al_{11}Mn_4(HT) \rightarrow \phi$  and  $L + \phi \rightarrow Al_4Mn$ ; they did not,

however, address question of the stability of the  $\mu$  phase. Most of the differences between these two diagrams can be understood in terms of the different experimental techniques that were used.

Taylor's was an XRD study of as-cast samples and bulk samples annealed for two weeks at 750, 810, 850 and 950 °C. The diagram was constructed by assuming that all the observed phases were stable equilibrium phases and assigning melting temperatures to each from the previous thermal analysis work by Dix et al. [3] and Phillips [4]. Evidence was obtained that  $\text{Al}_4\text{Mn}$  can persist up to a temperature between 810 and 850 °C, (supporting Phillips' thermal analysis and metallographic results), but no direct evidence was obtained to associate the melting of  $\phi$  with the thermal arrests observed by Dix at -920 °C. However, the structures of the phases observed by Taylor have all been verified by independent studies (that of  $\mu$  in this work). The phases and their structures are summarized in Table 1, using the nomenclature adopted in the present work.

The investigation by Goedecke and Koester was carried out using thermal analysis on heating and cooling, supported by metallographic examination but not by XRD. Equilibration times of 80 days, rather than 2 weeks, were used. Between 12 and 22 at.% Mn, Goedecke and Koester observed on cooling reactions at about 880, 860, and 840 °C; but on heating above 800 °C they found only one melting reaction at 923 °C.

It can tentatively be concluded that the work of Goedecke and Koester established the melting reactions of the stable equilibrium diagram, but is not definitive with regard to the identities of the phases in equilibrium. The work of Taylor established the structures of phases to be accounted for, but did not establish their stability ranges.

Comparison of the two diagrams suggests three ways in which the diagram proposed by Goedecke and Koester requires modification:

(1) All the phases found by Taylor must be included either stably or metastably. That Taylor observed no " $\text{Al}_4\text{Mn}$ " at 850 °C and that Goedecke found " $\text{Al}_4\text{Mn}$ " to be stable up to 923 °C, strongly suggests that the phase that Goedecke identified as " $\text{Al}_4\text{Mn}$ " should rather be identified with  $\mu$  phase. This is consistent with compositions at which  $\mu$  and " $\text{Al}_4\text{Mn}$ " (here called  $\lambda$ ) were observed by all investigators [1,2,4].

(2) The interpretation of the two reactions at 880 and -860 °C as the metastable peritectic reactions in which  $\phi$  and  $\mu$  are successively formed from the melt must be revised, because it is not thermodynamically self-consistent. As drawn by Goedecke and Koester, the extension of the  $\phi$  liquidus below 860 °C lies above the stable  $\mu$  liquidus in temperature. Because a metastable two-phase field cannot extend into a stable single-phase field, this construction implies that  $\phi$  is a stable phase. This, however, was not intended by Goedecke and Koester, nor is there any experimental evidence that  $\phi$  is a stable phase.

(3) There are conflicts about the peritectic temperature at which  $\text{Al}_6\text{Mn}$  is formed. Reactions have been reported at 670 to 690 °C (on cooling) and at about 710 °C (on heating only). It is usually assumed that the lower reaction is the effect of undercooling and involves the same phases as the higher reaction. Thus most investigators [1,2,3] placed the equilibrium peritectic isotherm between 700 and 710 °C. However, Phillips [4] had disputed this interpretation: he found arrests at 690 °C on both heating and cooling but none at 710 °C. When the  $\lambda$  phase is incorporated into the diagram, it is plausible to suppose that  $\text{Al}_6\text{Mn}$  may be formed from either Liquid +  $\mu$  or Liquid +  $\lambda$  and that the two reactions may be near 700 °C.

### III. EXPERIMENTAL DETAILS

The experimental techniques used in this study were constant heating/cooling rate differential thermal analysis (DTA), x-ray diffraction analysis (XRD), and transmission electron microscopy (TEM).

The samples studied were splat-quenched ribbons containing from 12 to 55 at% Mn, prepared from 99.999% Al and 99.98% Mn. Stated compositions are starting compositions for arc melted buttons. Some weight loss occurred during arc melting. No analysis of the ribbon was performed, but true compositions are believed to be within 0.5 at% or better of the starting composition. Ribbons were prepared by melting chunks of the arc melted buttons and squirting the liquid under He pressure onto a single, rapidly rotating Cu wheel. Full details of sample preparation and of the TEM and XRD methods have been given by Schaefer et al. [9], the DTA instrument and technique of DTA data analysis by McAlister et al. [10].

### III. EXPERIMENTAL RESULTS AND DISCUSSION

In the as-quenched condition, almost all of the samples contained metastable phases. The only exceptions were those with compositions falling within the equilibrium single phase  $\gamma_2$  region.

The approach to equilibrium of the metastable samples under constant heating rate conditions was studied to assure the relevance of higher temperature DTA results to the equilibrium diagram and to supplement the available thermodynamic data.

For many compositions, the approach to equilibrium is quite complex. For illustration, Fig. 2 shows a DTA trace obtained at a heating rate of 15 °C/min from a sample containing 20 at% Mn. Four distinct exothermic peaks are observed below 800 °C. The phases successively present were identified by carrying out additional heats, in which heating was stopped between

exothermic peaks and the sample quickly cooled, then examined by XRD and TEM. The as-splat-quenched 20 at% Mn sample contained the quasicrystalline icosahedral [11] and decagonal [12] phases, the latter predominating. In the first exothermic reaction, the icosahedral phase transformed to metastable  $\text{Al}_6\text{Mn}$ . In the second,  $\text{Al}_6\text{Mn}$  transformed to the decagonal phase. In the third, the decagonal phase transformed to  $\lambda$ , and in the fourth,  $\lambda$  transformed to  $\mu$ . The subsequent endothermic transformations occurred at temperatures in excellent agreement with those reported by Goedecke and Koester [2] in heating of a 20 at% sample heat treated for 80 days at 700 °C.

Fig. 3 summarizes the DTA (heating) and XRD results for samples containing from 12.2 to 22.4 at% Mn. With the exception of the high temperature form of  $\text{Al}_{11}\text{Mn}_4$ , which could not be retained on cooling in the DTA instrument, all of the phases reported by Taylor [1] in this composition range were observed. The endothermic events above 800 °C are in excellent agreement with the results of Goedecke and Koester [2]. The discrepancies are in the neighborhood of 700 °C.

All of the samples in the 12.2 to 22.4 at% Mn range were also cooled from the liquid. Our cooling results are compared in Fig. 4 with the cooling data from previous investigations [1,2,3,4].

Overall our results on the equilibrium diagram are in very close agreement with those of Goedecke and Koester. Of particular interest is the confirmation of the  $\gamma_1 \rightleftharpoons \text{Al}_{11}\text{Mn}_4(\text{HT}) + \gamma_2$  eutectoid at 957 °C and the  $\gamma_1 + \gamma \rightleftharpoons \gamma_2$  peritectoid at 900 °C which they were the first to report.

However, our results differ from theirs in two important respects. They identified the room temperature equilibrium phase at 20 at% Mn as " $\text{Al}_4\text{Mn}$ " (the  $\lambda$  phase), evidently without performing XRD structural analysis. It can be deduced from the results presented in Fig. 3 that the low temperature

equilibrium phase at 20 at.% is the  $\mu$  phase. This leaves the question of how to incorporate  $\lambda$  in the stable or metastable phase diagrams, between  $\text{Al}_6\text{Mn}$  and  $\mu$ . Our data strongly suggest that  $\lambda$  is a stable equilibrium phase, formed in the peritectoid reaction  $\text{Al}_6\text{Mn} + \mu \rightleftharpoons \lambda$  at  $693 \pm 2$  °C, and that  $\lambda$  is single phase at 18 at.% Mn and 680 °C. Fig. 5 presents melting studies upon which this opinion is based. These melts were carried out on samples previously heated to a temperature just below the  $L \rightleftharpoons (\text{Al}) + \text{Al}_6\text{Mn}$  eutectic to transform the metastable icosahedral and/or decagonal phases present in the as-quenched samples. Very near and below the composition  $\text{Al}_6\text{Mn}$ , a melting event started at about 720 °C. (Chilled liquid has been observed by TEM in these samples after cooling from 750 °C). For compositions above  $\text{Al}_6\text{Mn}$  to 18 at.% Mn, two overlapping transformations occur, the lower starting at about 693 °C. The starting temperature of the upper reaction cannot be determined directly from the DTA traces, but has been estimated via model analysis of slow DTA runs at 15.4 at.% Mn to be  $706 \pm 3$  °C. The upper reaction becomes progressively weaker as the Mn content increases. Interpretation of these results is readily obtained from the calculated diagram shown in Fig. 4, if it be assumed that  $\mu$  nucleates easily upon  $\lambda$ , but only reluctantly upon  $\text{Al}_6\text{Mn}$ . For compositions at or below  $\text{Al}_6\text{Mn}$ , no  $\lambda$  is initially present, the stable reaction  $L + \mu \rightleftharpoons \text{Al}_6\text{Mn}$  is suppressed, and the metastable  $L + \gamma \rightleftharpoons \text{Al}_6\text{Mn}$  reaction shown in Fig. 4 occurs, with  $\lambda + \mu$  conversion proceeding immediately thereafter. Above the composition  $\text{Al}_6\text{Mn}$ , the reaction sequence is different because one starts with a two phase assemblage of  $\lambda + \text{Al}_6\text{Mn}$ . The reaction  $\text{Al}_6\text{Mn} + \mu \rightleftharpoons \lambda$  occurs readily, since  $\lambda$  is already present; then the reaction  $L + \mu \rightleftharpoons \text{Al}_6\text{Mn}$  can also occur readily because now  $\mu$  is already present. The measured heats of these reactions are in very good agreement with the heats calculated from the present model, as shown in Fig. 6.

Samples transformed at constant heating rate in the DTA instrument from the initial metastable condition often do not have equilibrium phase abundances. For example, the 18 at% Mn sample initially contained principally decagonal phase, with a trace of icosahedral, and no detectable (Al). When heated in the DTA instrument to 670 °C, the sample was found to contain both  $\lambda$  and some  $\text{Al}_6\text{Mn}$ . However, after heat treatment for two and seven days at 680 °C, the sample consisted of single phase  $\lambda$ . Given the very small grain size observed in the as quenched and DTA heated samples, we believe this length of heat treatment adequate to produce equilibrium and consider this further evidence that  $\lambda$  is a stable equilibrium phase. Why then was  $\lambda$  not observed by Goedecke and Koester [2] in samples containing 15, 17, and 19 at% Mn? They heat treated these samples for 80 days at 700 °C and quenched them. In our view, the heat treatment was carried out in the  $\text{Al}_6\text{Mn} + \mu$  two phase region, and formation of  $\lambda$  was suppressed in quenching.

#### IV. THERMODYNAMIC CALCULATIONS

The aim of the calculations is to construct Gibbs energy functions for the liquid, fcc,  $\text{Al}_6\text{Mn}$ ,  $\lambda$ ,  $\mu$ ,  $\delta$ , and  $\text{Al}_{11}\text{Mn}_4$  phases which reproduce the stable liquidus, invariant reactions, and thermochemical data and predict the metastable phase equilibria.

Gibbs energies of the pure elements are represented in the form

$$G^\circ = H^\circ - TS^\circ$$

where T is absolute temperature, i.e. heat capacities are not taken into account. For the phase diagram calculation, this means that differences in heat capacities of different phases are not taken into account. This approximation proves satisfactory for most phase diagram calculations.

Gibbs energies of the compounds are also represented in this form; that is, the homogeneity ranges are not taken into account. Moreover,  $\text{Al}_{11}\text{Mn}_4$

which has low- and high-temperature forms (one with a fairly wide composition range, the other very narrow) is represented as a single line compound. Our interest in the present calculations is the liquidus, three-phase equilibria and heats of formation of the compounds. The variation of Gibbs energies of intermetallic compounds with composition are not central to the present study, and the homogeneity ranges are in any case not well enough known.

Excess Gibbs energies of the liquid, fcc, and bcc solution phases are, represented as polynomial expansions in composition and temperature

$$G^{XS} = x_{Al} x_{Mn} [A(T) + B(T)(x_{Al} - x_{Mn}) + \sum C_i(T) P_i(x_{Al} - x_{Mn})]$$

where  $x_{Al}$  and  $x_{Mn}$  are atomic fractions of Al and Mn;  $P_i$  are Legendre polynomials; and A, B, and C are temperature dependent coefficients of the polynomial expansion. The number of coefficients used to describe each solution phase was chosen as the fewest required to fit the selected experimental data within the estimated experimental uncertainty.

Thermodynamic data for the liquid come from different experimental techniques and have different accuracy over the composition range. Heats of mixing were measured calorimetrically over the whole range by Esin et al. [13]; the heats have not yet been verified by an independent investigation. They reach a minimum of -17000 J/mol and are reproduced by a subregular solution model ( $A=0$ ,  $B=0$ ,  $C=0$ ) with maximum discrepancy of 600 J/mol. The excess entropy is derived from partial Gibbs energies measured by the emf technique by Batalin et al. [14]. The data have been assessed by Desai [15]: the assessed integral excess entropies  $S^{XS}$  are negative at the Al-rich end but positive at the Mn-rich end; they reach a minimum of -5.403 J/mol K at  $x_{Mn} = 0.4$ , with an assessed uncertainty of  $\pm 2.5$  J/mol K. It is therefore not clear that even the variation from positive to negative  $S^{XS}$  is real, and  $S^{XS}$  is represented by one symmetrical term in the polynomial expansion.

The liquid phase Gibbs energy was checked for consistency with the phase diagram over the whole range. At intermediate compositions, accurate calculation of the diagram is ruled out by lack of information about the structures of several phases whose homogeneity ranges are substantial and whose Gibbs energies would be required in some detail. However it has been verified that the phase equilibria among the liquid and the terminal solid solutions ( $\delta$ Mn), ( $\gamma$ Mn), and ( $\beta$ Mn) can be calculated from the subregular solution model for the liquid and estimated regular and subregular contributions to the solid phase Gibbs energies. In particular, the Gibbs energy of the fcc (Al) solution is continuous with that of fcc ( $\gamma$ Mn) solution and reproduces the solubility of Mn in fcc Al.

Kubaschewski and Heymer [15] measured heats of formation of alloys containing 14.2, 20, and 26.7 at.% Mn calorimetrically at 300 to 350 °C. They estimated that the results were accurate to  $\pm 1000$  J/mol and reported that completeness of alloy formation was verified by XRD and metallographic analysis. It can be assumed that the 14.2 and 26.7 at.% Mn alloys had formed stable  $\text{Al}_6\text{Mn}$  and  $\text{Al}_{11}\text{Mn}_4$ (LT) respectively; however in view of the even recent failure to distinguish  $\lambda$  and  $\mu$ , it is not known what phase or phases were present in the 20 at.% Mn alloy. Therefore, the enthalpies of  $\text{Al}_6\text{Mn}$  and  $\text{Al}_{11}\text{Mn}_4$  are based on Kubaschewski's values; the enthalpies of  $\lambda$ ,  $\mu$ ,  $\phi$  and were estimated as approximately equal to those of  $\text{Al}_6\text{Mn}$  and  $\text{Al}_{11}\text{Mn}_4$  and adjusted to fulfill the requirement that above about 400 °C,  $\phi$  is a metastable phase. The range 0 to 30 at.% Mn was calculated. The following assumptions were made for the calculation of the range 0 to 30 at.% Mn:

- (1) The liquidus between 923 and 990 °C is that of  $\text{Al}_{11}\text{Mn}_4$ .
- (2) At 923 °C there occurs the peritectic reaction  $\text{L} + \text{Al}_{11}\text{Mn}_4 \rightarrow \mu$ .

(3) At about 700 °C two peritectic reactions compete for stability,  $L + \mu \rightarrow Al_6Mn$  and  $L + \lambda \rightarrow Al_6Mn$ .

(4) The peritectic reaction at 880 °C is  $L + Al_{11}Mn_4 \rightarrow \phi$  and it is metastable.

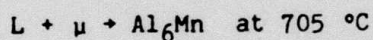
(5) The  $\phi$  liquidus lies everywhere to the Mn-side of the stable liquids (i.e.  $\phi$  is a metastable phase).

(6) If  $\mu$  is not considered, then  $\lambda$  is the next most stable phase in equilibrium with the liquid up to about 800 to 830 °C.

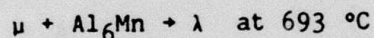
These assumptions were sufficient to estimate the entropies of fusion of  $Al_6Mn$  and  $Al_{11}Mn_4$  and the Gibbs energies of  $\mu$ ,  $\lambda$ , and  $\phi$ . The Gibbs energy parameters are listed in Table 2.

#### V. DISCUSSION OF THE CALCULATIONS

In Fig 4, six independent liquidus curves are shown: those representing equilibrium with fcc Al,  $Al_6Mn$ ,  $\lambda$ ,  $\mu$ ,  $\phi$  and  $Al_{11}Mn_4$ . For any given composition, the uppermost curve is the stable equilibrium liquidus; in this calculation the stable liquidus consists of branches for  $Al_{11}Mn_4$ ,  $\mu$  and  $Al_6Mn$ . At those points where the stable equilibrium crosses from one liquidus branch to another, there occur the peritectic reactions:

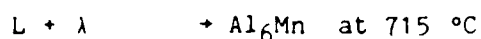


These are the only peritectic reactions in this portion of the stable equilibrium diagram, in addition there is a peritectoid solid state reaction

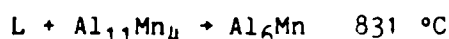
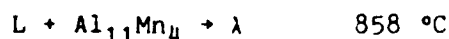


The other points where one liquidus branch crosses another give rise to metastable peritectic reactions that can be observed experimentally under suitable conditions: namely, that the more stable phases cannot nucleate and grow. A metastable equilibrium diagram can be obtained by imposing the

constraint that a particular phase does not appear and finding the next most stable equilibrium diagram when that phase is not taken into account. In Al-Mn the appropriate phase to omit is  $\mu$ , and the metastable sequence of peritectic reactions is:



Experimentally the reaction  $L + Al_{11}Mn_{14} + \phi$  is the most reproducible of the peritectic reactions seen on cooling. The lower peritectic reactions are predicted to be the only ones to occur during cooling if each succeeding reaction proceeds to completion. However, in this system, reactions are not completed during slow cooling. If it be assumed that all solid phases formed at high temperature are present (for example  $Al_{11}Mn_{14}$  below 884 or  $\phi$  below 847  $^\circ\text{C}$ ), then there are additional peritectic reactions by which they can decompose to more stable assemblages:



In some cooling curves, it is observed that as many as five distinct reactions can occur between 800 and 900  $^\circ\text{C}$ , and the present calculation should be understood as a predictive guide to identifying the phases in equilibrium in the sequence of reactions. Gibbs energies are not accurately enough known that the reaction temperatures or the metastable liquidus can be predicted with any confidence, but the order in which various liquidus branches cross in the interval 800 to 900  $^\circ\text{C}$  is determined only by the assumption that  $\phi$  and then  $\lambda$  appear from the liquid metastably on cooling.

## VI. SUMMARY

The aim of the present investigation was resolution of certain obscure features of the Al-Mn phase diagram. The experimental approach was guided by assessment of the previous literature and modeling of the thermodynamics of the system. It has been shown that two phases of approximate stoichiometry "Al<sub>4</sub>Mn" ( $\lambda$  and  $\mu$ ) are present in stable equilibrium,  $\lambda$  forming by a peritectoid reaction at  $693 \pm 2$  °C. The liquidus and invariant reactions as proposed by Goedecke and Koester have been verified. A map has been made of the successive non-equilibrium phase transformations of as-splat-quenched alloys. Finally, the thermodynamic calculation of the phase diagram allows interpretation of complex reaction sequence during cooling in terms of a catalogue of all the metastable invariant reactions involving (Al), Al<sub>6</sub>Mn,  $\lambda$ ,  $\mu$ ,  $\phi$ , and Al<sub>11</sub>Mn<sub>4</sub> phases.

## ACKNOWLEDGMENTS

Thermodynamic calculations were performed using software graciously provided by H.L. Lukas, G. Petzow, and E.-Th Henig of the Max-Planck Institute, Stuttgart, Federal Republic of Germany.

Table I. Structures and Lattice Parameters of Al-rich Intermetallic Compounds (Compiled from the literature by Pearson (8))

Phase	Structure	Space group	Lattice Parameters (nm)
$\text{Al}_6\text{Mn}$	$\text{D}_{2h}$	$\text{Cmcm}$	$a=0.75518$ $b=0.64978$ $c=0.88703$
$\lambda(\text{Al}_4\text{Mn})$	hexagonal	-	$a=2.841$ $c=1.238$
$\mu$	hexagonal	-	$a=1.995$ $c=2.452$
$\phi(\text{Al}_{10}\text{Mn}_3)$	$\text{D}_{8_{11}}(\text{Co}_2\text{Al}_5)$	$\text{P}6_3/\text{mmc}$	$a=0.7543$ $c=0.7898$
$\text{Al}_{11}\text{Mn}_4(\text{HT})$	orthorhombic	$\text{Pnma}$	$a=1.479$ $b=1.242$ $c=1.259$
$\text{Al}_{11}\text{Mn}_4(\text{HT})$	triclinic	$\text{P}\bar{1}$	$a=0.5092$ $\alpha=85^\circ 19'$ $b=0.8862$ $\beta=100^\circ 24'$ $c=0.5047$ $\gamma=105^\circ 20'$
$\gamma_2$	$\text{D}_{8_{10}}(\text{Cr}_5\text{Al}_8)$	$\text{R}3\text{m}$	$a=1.2739$ $c=1.5861$

Table II. Al-Mn Gibbs Energies Obtained in the Present Calculations

Gibbs Energies of the Pure Components (in J/mol, J/mol K)

$G(L, Mn) = 0$	$G(Al_6Mn) = -27215 + 14.95 \quad T$
$G(L, Al) = 0$	$G(\lambda) = -31518 + 17.0988 \quad T$
$G(bcc, Mn) = -14644 + 9.6395 \quad T$	
$G(bcc, Al) = -627.6 + 6.6944 \quad T$	$G(\mu) = -34951 + 17.8 \quad T$
$G(fcc, Mn) = -16401 + 10.8803 \quad T$	$G(\phi) = -35400 + 17.025 \quad T$
$G(fcc, Al) = -10711 + 11.473 \quad T$	
	$G(Al_{11}Mn_4) = -35250 + 15.1 \quad T$

Parameters for Excess Gibbs Energies of Solution Phases (in J/mol, J/mol K):

$$A(L) = -68000 + 17 \quad T$$

$$B(L) = -3500$$

$$A(bcc) = -84000 + 16 \quad T$$

$$B(bcc) = -11000$$

$$A(fcc) = -67950 + 16 \quad T$$

$$B(bcc) = 3500$$

## FIGURES

Figure 1. The Al-Mn phase diagram according to Taylor [1] and Goedecke and Koester [2].

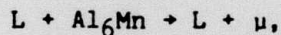
Figure 2. DTA trace for 20 at.% Mn obtained at a heating rate of 15 °C/min.

Figure 3. DTA and XRD results superimposed on the present assessment of the stable equilibrium phase diagram. T denotes the decagonal phase. Phase labels along the bottom of the diagram indicate structures of the as-splat-quenched ribbon; other phase labels indicate structures of alloys transformed on heating and rapidly cooled in the DTA instrument.

Figure 4. Cooling data from present and previous work, superimposed on the calculated phase diagram.

Figure 5. A series of melting curves showing evidence of two reactions  
 $L + \mu \rightleftharpoons Al_6Mn$  and  $L + \lambda \rightleftharpoons Al_6Mn$ .

Figure 6. Comparison of measured and calculated heats of the reaction sequences:



## REFERENCES

1. M.A. Taylor: *Acta Met.*, 1960, vol. 8, pp. 256-62.
2. T. Goedecke and W. Koester: *Z. Metallkd.*, 1971, vol. 62, pp. 727-32.
3. E.H. Dix, W.L. Fink and L.A. Willey: *Trans. AIME*, 1933, vol. 104, pp. 335-52.
4. H.W.L. Phillips: *J. Inst. Metals*, 1943, vol. 69, pp. 275-91.
5. H. Kono: *J. Phys. Soc. Japan*, 1958, vol. 13, pp. 1444-51.
6. A.J.J. Koch, P. Hokkeling, M.G.v.d. Steeg and K.J. de Vos: *J. Appl. Phys.*, 1960, vol. 31, pp. 755-75.
7. W. Koster and E. Wachtel: *Z. Metallkd.*, 1960, vol. 51, pp. 271-80.
8. W.B. Pearson: *Handbook of Lattice Spacings and Structures of Metals and Alloys*, vol. 2, Pergamon, New York, 1967.
9. R.J. Schaefer, D. Shechtman, W.J. Boettinger, and F.S. Biancaniello: National Bureau of Standards, Gaithersburg, MD, unpublished research, 1986.
10. A.J. McAlister, R.J. Schaefer, and F.S. Biancaniello: National Bureau of Standards, Gaithersburg, MD, unpublished research, 1986.
11. D. Shechtman, I. Blech, D. Gratias, and J.W. Cahn: *Phys. Rev. Lett.*, 1984, vol. 53, pp. 1951.
12. L. Bendersky, R.J. Schaefer, F.S. Biancaniello, W.J. Boettinger, M.J. Kaufman, and D. Shechtman: *Scripta Met.*, 1985, vol. 19, pp. 909-914.
14. Yu.O. Esin, N.T. Bobrov, M.S. Petrushevskii, and P.V. Gel'd: *Russ. J. Phys. Chem.*, 1973, vol. 47(8), pp. 1103-05.
14. P.D. Desai: *Thermodynamic Properties of Binary Al-Mn Alloy System*, CINDAS Report, 1985.
15. O. Kubaschewski and G. Heymer: *Trans. Farad. Soc.*, 1960, vol. 56, pp. 473-78

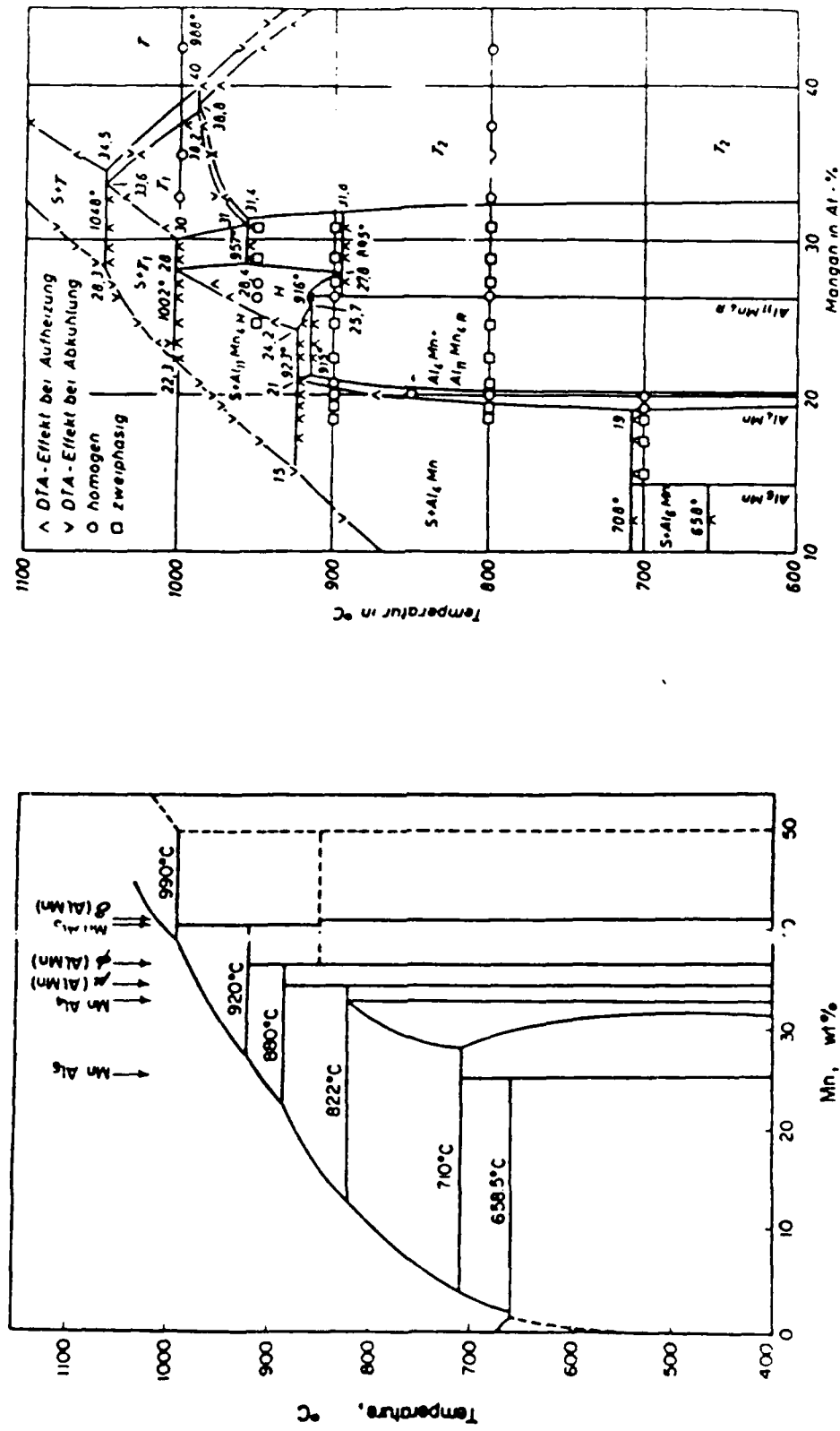


Figure 1. The Al-Mn phase diagram according to Taylor [1] and Goedecke and Koester [2].

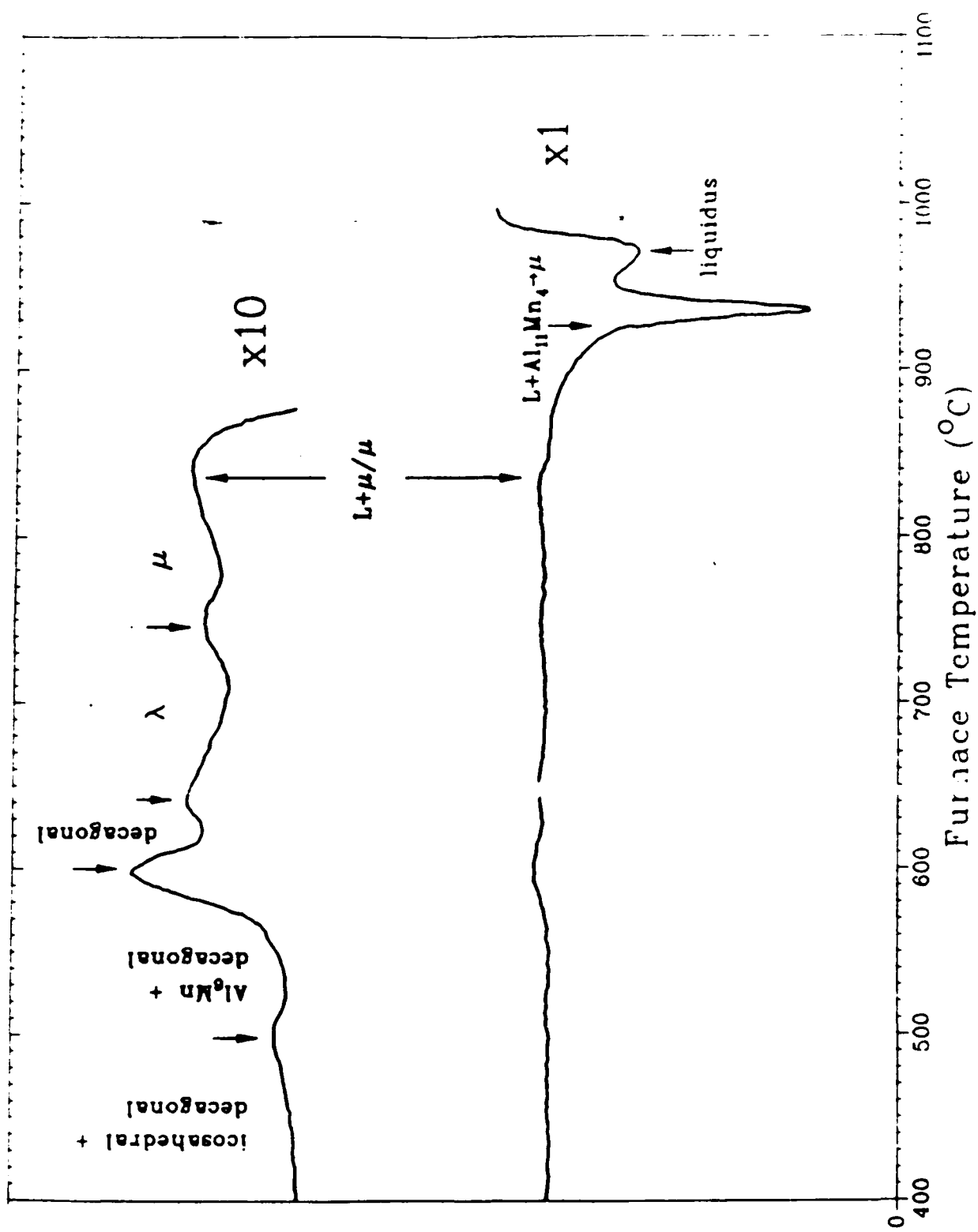


Figure 2. DTA trace for 20 at.% Mn obtained at a heating rate of 15 °C/min.

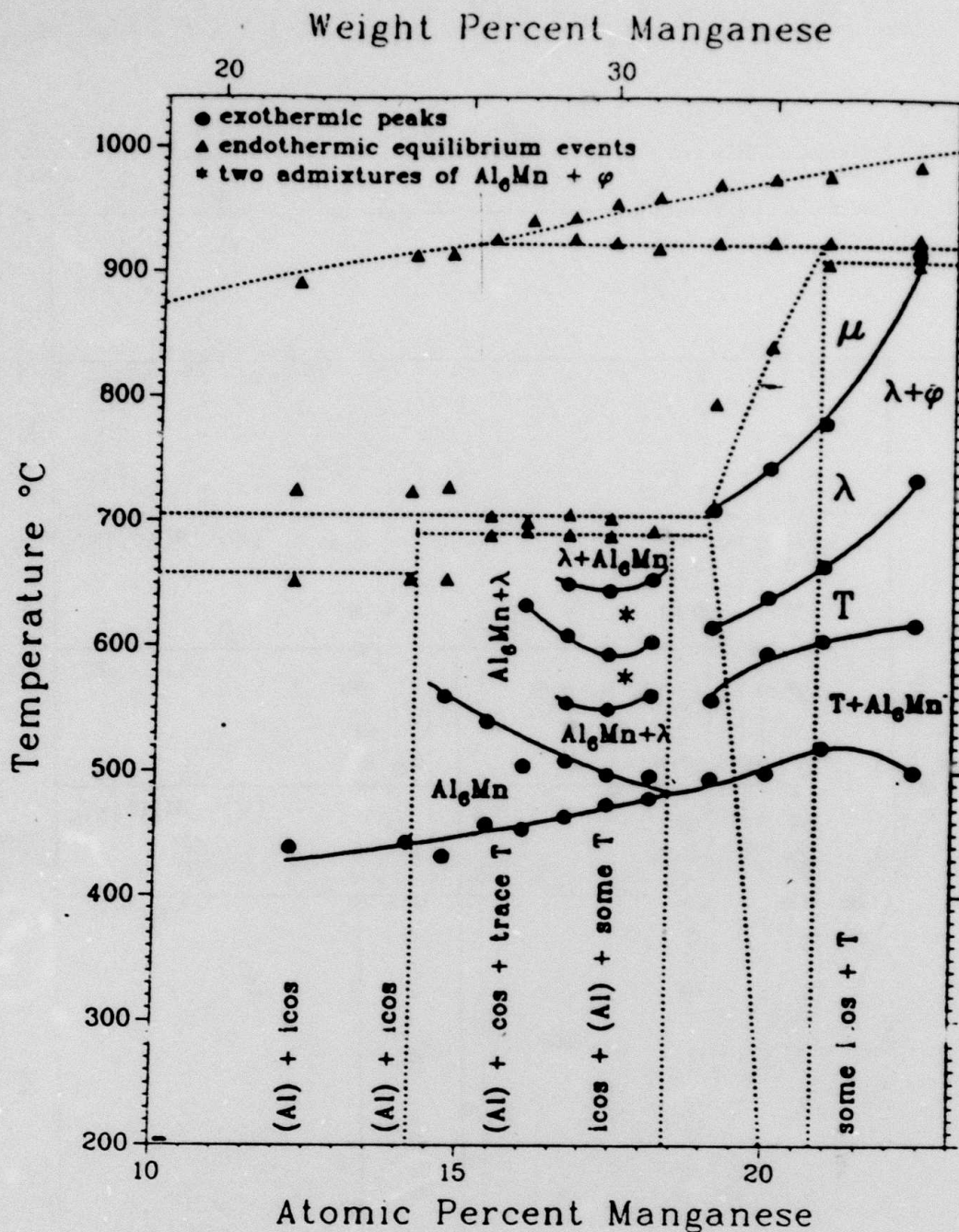


Figure 3. DTA and XRD results superimposed on the present assessment of the stable equilibrium phase diagram. T denotes the decagonal phase. Phase labels along the bottom of the diagram indicate structures of the as-splat-quenched ribbon; other phase labels indicate structures of alloys transformed on heating and rapidly cooled in the DTA instrument.

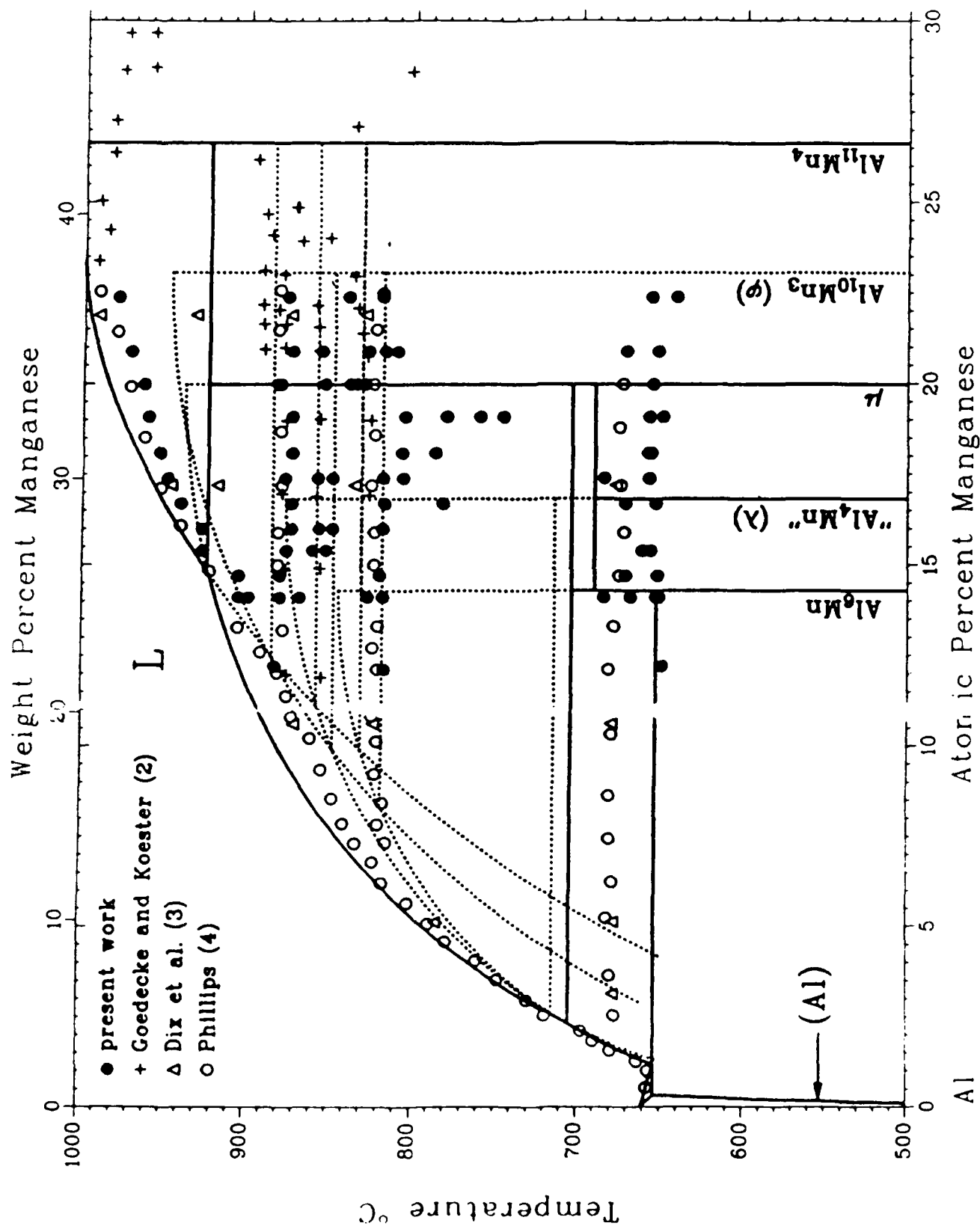


Figure 4. Cooling data from present and previous work, superimposed on the calculated phase diagram.

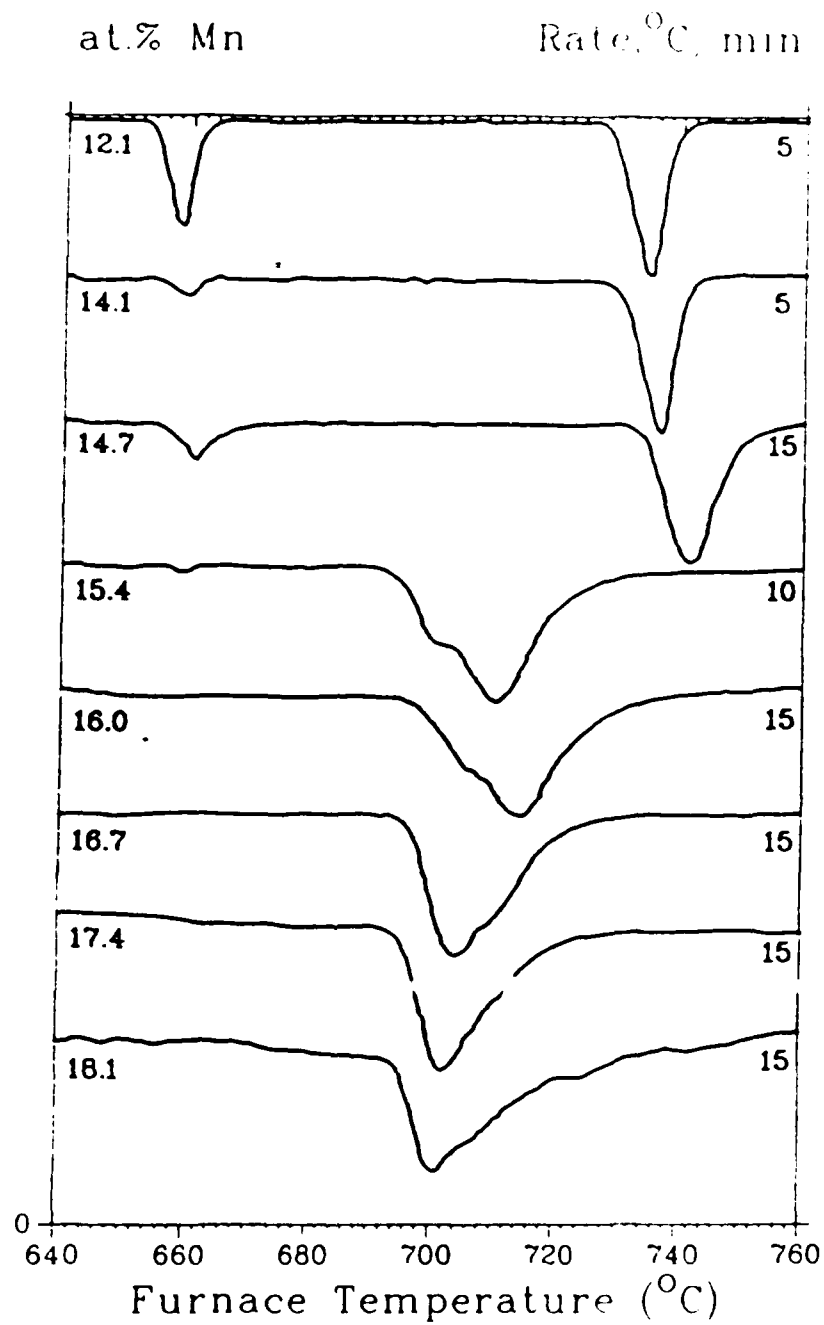
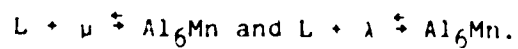


Figure 5. A series of melting curves showing evidence of two reactions



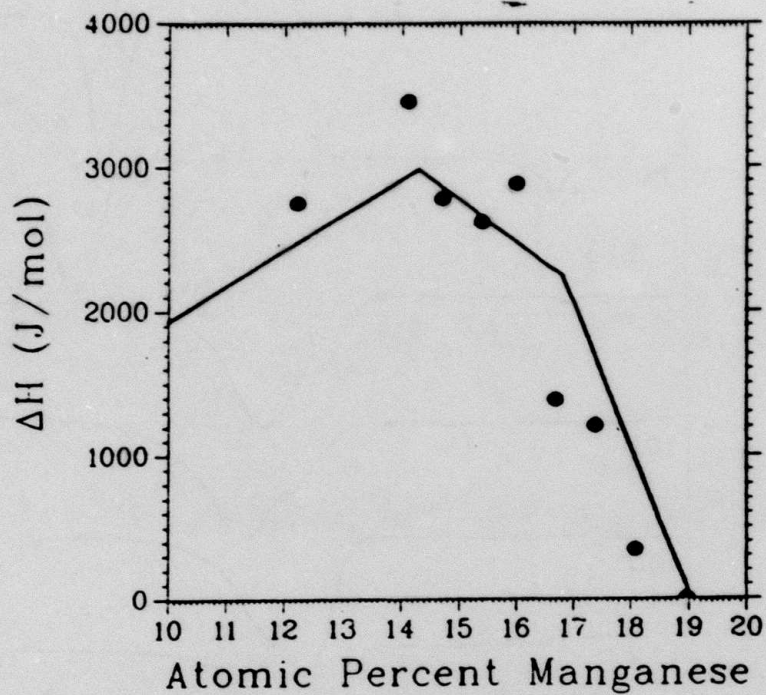


Figure 6. Comparison of measured and calculated heats of the reaction sequences:

